THE TRIBOLOGICAL BEHAVIOUR OF ALUMINIUM MATRIX COMPOSITES

by

Scott Wilson

A thesis submitted to the Faculty of Engineering, University of Cape Town in fulfilment of the degree of Doctor of Philosophy

Department of Materials Engineering
University of Cape Town
February 1993

ABSTRACT

Metal matrix composites consisting of 6061 and 2014 aluminium alloys, reinforced with 10%, 15% and 20% alumina particulates and a 6061 alloy reinforced with 20% SiC particulates, have been characterised in terms of their behaviour under various tribological conditions.

In abrasive environments, the wear behaviour of each composite is dominated by their ability to resist indentation by hard particles. Abrasion against fine grit particles leads to a reduced load per abrasive particle and a correspondingly significant reduction in wear loss.

Reciprocating sliding wear tests, conducted in an aqueous environment and against hardened steel counterfaces, displayed composite wear rates that were up to three orders of magnitude below those of their monolithic alloys. This is attributed to the increased resistance to surface shear provided by the reinforcing particulates themselves and their constraining effects on the matrix. The particulates become load bearing and protect the matrix by reducing the metal to counterface adhesive wear. However, the counterface wear increases due to the interaction with the hard reinforcements. Transmission electron microscopy of the worn composites reveal the formation of a transfer layer and subsurface dislocation structures which are similar to those found in metals subjected to low amplitude fatigue.

In contrast to the results for abrasive and sliding wear, the composites show increasingly inferior cavitation and solid particle erosion resistances with increasing volume fractions of particulates. This depreciating effect was especially evident for particle erosion and can be related to the inability of metal matrix composites to accommodate the increments of strain which accompany erosive processes.

The mechanisms responsible for the various performances have been studied by scanning electron microscopy, optical microscopy and transmission electron microscopy. An attempt is made to reconcile the steady state wear rates of the reinforced and unreinforced alloys with their observed wear modes, microstructures and bulk mechanical behaviour.

ACKNOWLEDGEMENTS

I would like to express my appreciation to all those who have assisted me in the course of this work:

In particular I am very grateful to Professor A Ball, my supervisor, for his help and encouragement during the research project.

I am thankful to Dr T Hurd and Mr BI Dennis of Hulett Aluminium Pty. Ltd., Pietermaritzburg, for their helpful suggestions, financial support and supply of materials for this project.

The help, encouragement and technical support of Mr D van Heerden and the late Professor MP Shaw with transmission microscopy are gratefully acknowledged.

Thanks are also due to the staff of the Electron Microscope Unit, for their technical assistance.

The technical assistance of Mr G Newins and Mr N Dreze (workshop), Mr B Greeves and Mr J Petersen (photographic), Professor JFW Bell (elastic modulus measurements) and Mrs M Hoosen (laboratory), are gratefully acknowledged.

I am very grateful for the administrative support and help of Mrs JD Sharland and Mrs AC Ball.

Thanks are also due to the staff and students of the Department of Materials Engineering for their support and encouragement.

The financial support of Huletts Aluminium Pty. Ltd. and the FRD (Foundation for Research and Development) are gratefully acknowledged.

Dedicated to Bill and Carol, my parents.

Table of Contents

	Page no.
1.0 Introduction	1
1.1 Research Approach	2
2.0 Literature Review	5
2.1 Mechanical behaviour of aluminium matrix composites	5
2.2 Abrasion	9
2.2.1 *Abrasive wear of aluminium and aluminium alloys*	9
2.2.2 *Abrasive wear of multi-phase microstructures*	9
2.2.3 *Abrasion of aluminium matrix composites*	11
2.3 Sliding Wear	14
2.3.1 *Sliding wear of aluminium and aluminium alloys*	14
2.3.2 *Sliding wear behaviour of aluminium matrix composites*	14
2.3.3 *Transfer phenomena and subsurface deformation in aluminium matrix composites*	18
2.4 Solid Particle Erosion	21
2.5 Cavitation Erosion	24
3.0 Materials and Experimental Methods	25
3.1 Materials	25
3.1.1 *Preliminary heat treatment*	26
3.1.2 *Heat treatment*	26
3.1.3 *Composite microstructures*	26
3.1.4 *Matrix microhardness tests*	27
3.1.5 *Young's Modulus determination*	28
3.1.6 *Wear and tensile specimen preparation*	28
3.2 Tensile testing	29
3.3 Abrasion testing	29
3.4 Reciprocating sliding wear tests	30
3.5 Solid particle erosion tests	32
3.6 Cavitation erosion testing	33

3.7 Transmission electron microscopy 37

4.0 Results 36
4.1 Materials Characterisation 36
4.1.1 *Preliminary heat treatment results* 36
4.1.2 *Heat treatment and matrix microhardness tests* 38
4.1.3 *Monolithic alloy and composite microstructures*
39
4.1.4 *Young's Modulus results* 43
4.2 Tensile Test Results 43
4.3 Abrasive Wear Results 49
4.3.1 *Abrasion resistance against a silicon carbide abrasive* 56
4.4 Reciprocating Sliding Wear Results 57
4.4.1 *Dislocation substructures and transfer layer characterisation* 71
4.5 Solid Particle Erosion 78
4.6 Cavitation Erosion Results 87

5.0 Discussion 96
5.1 Tensile Properties 96
5.2 Abrasion 102
5.3 Reciprocating Sliding Wear 107
5.3.1 *Dislocation substructures* 118
5.4 Solid Particle Erosion 120
5.5 Cavitation Erosion 127

6.0 Conclusions 134

7.0 References 137

Appendix 1 144

List of symbols and abbreviations

E = Young's Modulus

$E_{fracture}$ = Tensile work to fracture

UTS = Ultimate tensile strength

YS = Yield stress (0.1% proof)

γp = Plastic strain amplitude

α = Thermal expansion coefficient

C = Specific heat capacity

σ = Thermal conductivity

ε_f = Strain to wear and microfracture

1.0 Introduction

Aluminium alloys are used extensively for the manufacture of low density, high strength items for high speed reciprocating mass components and structural members in the aerospace and general transport sectors. Recently, the dominance of aluminium alloys has been challenged by the development of advanced polymeric composite materials having stiffness, strength and density characteristics ideally suited for high performance energy efficient applications. In response to this competition there have been a number of developments in the aluminium industry; the major ones being the high modulus aluminium lithium alloys, the aluminium-polymeric (aramid fibre) composite laminates and aluminium alloys reinforced with continuous and discontinuous ceramic reinforcement (metal matrix composites) [1].

Heat treatable aluminium alloys reinforced with discontinuous ceramic fibres or particulates are presently the most commonly available and easily produced metal matrix composites. These materials were developed originally for their greater stiffness and strength compared to ordinary monolithic alloys and have been used in a limited but growing number of applications. In the early 1980's, a motor company initiated the use of alumina fibres to reinforce the piston ring area of their diesel engine pistons with successful results [2]. Other engine components being considered for manufacture from aluminium composites are drive shafts, connecting rods and rocker arms [3]. The thermal expansion properties of silicon carbide reinforced aluminium alloys can be tailored to levels well below those of conventional aluminium alloys [4]. The use of reinforcing ceramics with high thermal conductivity and specific heat, such as silicon carbide, makes these materials excellent heat sinks and ideal for housing electronic instruments.

Recent research has focused on the friction and wear behaviour of aluminium matrix composites (eg.[5-14]). As metal matrix composites are considered as candidate materials in applications such as engines and aerospace structures, the need to characterise their behaviour in a range of different wear environments has become critically important. The increased research efforts into the tribological behaviour of metal matrix composites has resulted in their becoming more

competitive as wear resistant materials. Examples include the seizure resistant aluminium graphite [5] composites and, more recently, the pilot testing of silicon carbide reinforced aluminium alloys as brake discs for high speed railway vehicles [6]. Aluminium matrix composites are also finding increased usage in the automotive industry in applications such as cylinder liners, where the traditionally used cast iron liner has been done away with and replaced by the aluminium engine block which has been selectively reinforced with alumina, as well as carbon fibres for lubricity [15]. Pistons, gear selector forks, propshafts and brake rotors are also being manufactured from aluminium matrix composites [15].

1.1 Research approach

This thesis focuses on the wear behaviour of two age hardening commercial aluminium alloys, each reinforced with different volume fractions of ceramic particulates. While most other research reported to date generally tends to concentrate on the behaviour of aluminium matrix composites in one type of wear situation, the approach taken here is based on an attempt to characterise the responses of each reinforced and unreinforced alloy in a variety of tribological environments. This should provide an insight into the various modes of wear and the controlling mechanisms. The need to characterise the wear behaviour of these materials in as many different tribological conditions as possible, becomes ever important as they find applications in critical components in engines and other machinery. This approach is essential due to the fact that up to three or four different wear modes can exist at one time in an item of machinery a good example being the piston chamber in an internal combustion engine. Here, wear loss generally occurs as a result of the reciprocating nature of the piston rings against the liner during normal operation. This wear can be both adhesive and abrasive depending on the factors such as the level of oil starvation at the sliding interface, sliding speed, temperature and the presence of abrasive contaminants in the fuel or oil. The reciprocating motion of the piston and pressure changes arising from fuel combustion are also conducive to the setting up of high frequency vibrations in the piston chamber. These vibrations can initiate cavitation in the lubricant that coats

the pistons, liners and valves, and may result in cavitation erosion damage of these components.

When an engine runs under adverse conditions such as oil starvation or overheating, the aforementioned wear modes can become very severe, often leading to rapid seizure and damage to the rest of the engine components. In this regard, both the engine design and its materials of construction can be critical in limiting the onset of adverse conditions. In particular, the thermal properties of the materials in contact are important, especially their thermal conductivities and thermal expansion coefficients. Materials having a high thermal conductivity will be better able to conduct heat away from a sliding interface at a high rate, thus preventing effects such as thermal softening, seizure and melting. The difference in thermal expansion coefficient between for example, a piston and liner, are important as under high temperature conditions the expansion mismatch between the sliding materials may result in increased loads and seizure. What is possibly extremely attractive about using aluminium matrix composites as candidate materials for automotive components, is that their thermal expansion coefficients can be tailored to very low levels through the addition of ceramic reinforcement whose expansion coefficients are below those of aluminium. The thermal conductivity of some ceramics and intermetallics are very high, approaching those of metals such as aluminium eg. silicon carbide, boron nitride and aluminium nitride. These enhanced thermal properties make such ceramics ideal for use as heat conducting materials in high temperature wear situations.

The thesis initially deals with the tensile behaviour of each material. Uniaxial tensile tests were conducted on the reinforced and unreinforced alloys in order to determine how the addition of ceramic particulates influences the stress-strain response of the matrix aluminium alloys. Failure modes and strengthening mechanisms of each material are characterised and discussed in terms of their microstructural details and properties of the ceramic reinforcements and matrix alloys used. The tensile characteristics of each composite are then used to facilitate interpretation of the often complex deformation processes that occur in the tribological situations.

The wear behaviour of each material is determined for four different tribological environments, namely, two body abrasion, reciprocating sliding wear in an aqueous environment, solid particle erosion, and cavitation erosion. The two body abrasion resistances of each material are determined and compared, against fine mesh (low contact stress) and coarse mesh (high contact stress) abrasive papers. A reciprocating sliding wear testing arrangement is used to determine the behaviour of each reinforced and unreinforced alloy in sliding contact against a hardened stainless steel counterface. Erosion rates and wear modes are then determined for each material in cavitation erosion conditions in an aqueous environment and airborne solid particle impact conditions by silicon carbide particles.

The various surface topographies and subsurface microstructures associated with each type of wear are examined primarily through the use of optical and scanning electron microscopy techniques. An attempt is made to characterise subsurface dislocation arrangements using transmission electron microscopy, particularly in the case of reciprocating sliding wear. These results are then discussed in terms of the bulk and surface properties of each material, taking into account the different deformation modes, strain rates and contact stresses associated with each type of wear. Suggestions are then made for the optimal utilisation of metal matrix composites for specific tribological situations.

2.0 Literature Review

2.1 Mechanical behaviour of aluminium matrix composites

In the past decade there has been a surge of interest in discontinuously reinforced metal matrix composites and their mechanical properties. The addition of high modulus ceramic particles, fibres or whiskers to metallic materials offer marked increases in stiffness and in most cases, tensile strength, over monolithic alloys. Despite these improvements, metal matrix composites also display inferior fracture toughnesses and ductilities in contrast to their unreinforced matrix alloys. Considerable research effort has been devoted to studying the influence of ceramic reinforcement on the mechanical and microstructural properties of aluminium and its alloys. Several mechanisms have been suggested in interpreting the elastic and plastic constitutive response of these materials. A brief outline of some of the major works in this area is given below.

McDanels [16] evaluated the stress-strain behaviour and mechanical properties of 6061, 2124, 5083 and 7075 aluminium alloys, reinforced with discontinuous silicon carbide in whisker, nodule and particulate form. Improvements in ultimate tensile strength were obtained for alloys in the T6 heat treated condition, containing up to 20 vol.% silicon carbide, over that of their respective matrix alloys. Composites with the higher matrix strength alloys (2124 and 7075) had higher strengths but low ductilities, whereas the 6061 matrix composites exhibited both the greatest improvement in strength over its unreinforced condition, while maintaining high ductilities. The 5083 matrix composites, which had been optimised by solid solution strengthening and cold working (H-temper), failed in a brittle manner - with ultimate tensile strengths related to failure strain. This behaviour was attributed to the probable over-straining of the matrix alloy by the addition of the reinforcement, thus lowering the remaining strain energy available to gain potential strength and ductility.

McDanels noted that strength increased with increasing reinforcement content only as long as the composites were able to exhibit enough ductility to attain full strength. With additions of 30 vol.% or 40 vol.% silicon carbide, the strength increase was found to taper off due to the composites failing while still in the steeply ascending portion of the stress-strain curve. He postulated that the matrix probably did not have sufficient internal ductility to redistribute the very high localised internal stresses, thus leading to composite failure before their being able to reach stable plastic flow and normal ultimate strength. The fall off in strength with added reinforcement was most dramatic in the highest strength 7075 aluminium matrix composites, followed by the 2024

composites. The 6061 matrix composites however, showed negligible depreciation in strength even with reinforcement contents as high as 40 vol.%. A bar chart summarising McDanel's [16] results on the effect of matrix alloy, silicon carbide reinforcement type (whisker, nodule or particulate) and content on the ultimate tensile strengths of the discontinuously reinforced composites, is displayed in fig.1.

Arsenault and co-workers [17-24] have attributed the observed strengthening effect in discontinuous aluminium matrix composites to an increase in the dislocation density in the matrix alloy, caused by the difference in coefficients of thermal expansion between matrix and reinforcement. Dislocations are punched into the aluminium matrix as a consequence of the relaxation of the compressive thermal residual stress at particle - matrix interfaces, when the composite is cooled down from solution heat treatment temperatures [17]. Associated with increasing the volume fraction of reinforcement in aluminium is a resultant increase in dislocation density and a decrease in the dislocation subgrain size. The dislocation density and subgrain size are also affected by the aspect ratio and size of reinforcing particles or whiskers, with smaller inclusions generating higher dislocation densities and smaller subgrain sizes, culminating in improved strengths but reduced ductilities [23-25].

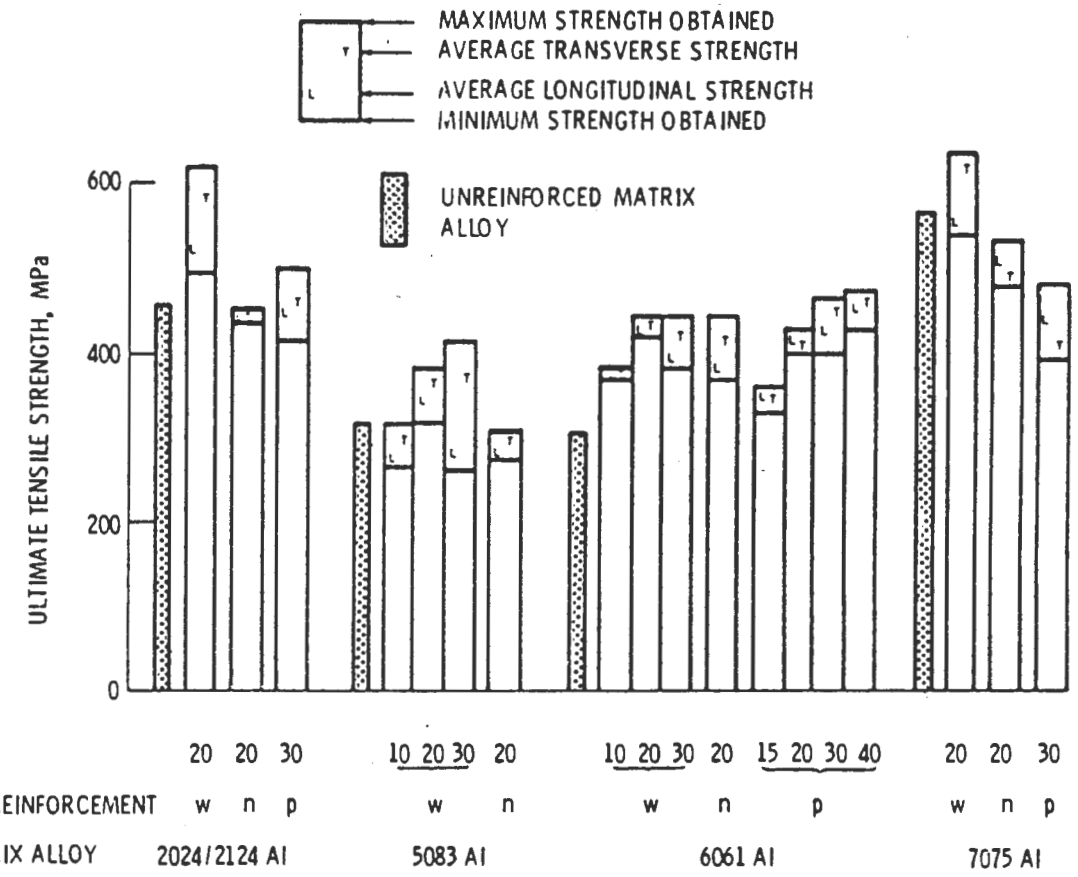

Fig.1: Effect of SiC reinforcement type and content on the ultimate tensile strengths of various discontinuous SiC/Al composites. After McDanels [16].

Other researchers have invoked continuum plasticity models to explain composite strengthening effects, in circumstances where dislocation structures are small compared to the size of the reinforcing particles [26,27]. While obtaining good agreement between experimental and theoretical power-law hardening behaviour, the continuum models predict strength increased based only on volume fraction considerations, and do not show any particle size dependencies, despite experimental evidence to the contrary [28-30].

Withers, Stobbs and Pedersen [31] used Eshelby's equivalent inclusion approach as a basis for the prediction of mechanical properties of short fibre reinforced metal matrix composites. The model was found to be successful in predicting Young's modulus, coefficient of thermal expansion, residual thermal stress and the transfer of load between aluminium matrix and silicon carbide inclusions, during elastic and plastic deformation. In their analysis of plastic deformation of composite materials, it was noted that the plastic strain of a matrix alloy and composite would be equal, were it not for the constraining effects of the high modulus inclusions which do not undergo plastic deformation. The total macroscopic plastic strain of the composite was given by:

$$e^{p}_{comp} = e^{p} + f e^{T(plastic)} \qquad (1)$$

where e^{p} is the uniform, stress-free deformation of the matrix, f is the volume fraction of the reinforcing phase and $e^{T(plastic)}$ the plastic misfit or stress-free transformation strain of an equivalent (Eshelby ellipsoid) homogenous inclusion.

For low volume fractions of inclusions, as is found in dispersion hardened materials, the macroscopic plastic strain of the composite is approximately equal to e^{p}. However, in metal matrix composites, the difference can be quite large, for example $e^{p}_{comp} = 0.5e^{p}$, for f=20 vol.% of whisker reinforcement. Since the equivalent transformation strain is of opposite sense to the plastic strain, the permanent macroscopic deformation of the composite is less than that of the matrix. Thus, as the volume fraction of inclusions is increased, disproportionately large mean stresses are generated in the matrix for a given composite plastic strain. Using this analysis, Withers and co-workers emphasize that the inclusions become more elastically distorted as the plastic flow of the matrix progresses, reducing the matrix stress at the expense of a corresponding increase in the inclusion stress.

The rate of transfer of stress from the more compliant matrix to the stiffer phase during plastic deformation, is directly influenced by the yield and strain hardening characteristics of the matrix alloy. While the matrix alloy flow stress is primarily dependant on its solute content and microstructure, the constraining effect of the

reinforcing inclusions changes the metals' yield criteria by raising the flow stress above the levels found in an unreinforced alloy. Apart from these considerations, phenomena such as thermal mismatch residual stresses [21], thermal mismatch dislocations [17] and changes in precipitation kinetics arising from these effects [32,33], further influence the flow stress and hardening behaviour in reinforced matrices, making comparisons with unreinforced alloys difficult to quantify.

A series of experimental and finite element investigations on age-hardening and unalloyed aluminium matrices, reinforced with ceramic inclusions was conducted by Christman, Needleman and Suresh [34]. They established that the dominant contribution to strengthening in these composites was due to the build-up of significant triaxial stresses in the matrix, due to the constraint imposed by the reinforcing particles. Of significant importance was their assertion that comparisons between age hardening reinforced aluminium alloys and their unreinforced counterparts were meaningless, unless they both had comparable microstructures ie. the accelerated ageing effects associated with reinforced alloys were taken into account during processing, such that the composite matrix and its monolithic alloy counterpart were of comparable strength and hardness [32].

Llorca, Needleman and Suresh [35] investigated the influence of hydrostatic stresses that develop as a result of constrained plastic flow, on void formation and growth phenomena in aluminium matrix composites. Using finite element methods together with experimental results of deformation of Al-Cu alloys reinforced with silicon carbide particulates, they established that factors that tend to increase matrix constraint during plastic flow (eg. large particle size and volume fraction) tend to decrease the overall strain to failure in the matrix and vice versa.

Lloyd [36] estimated that the triaxial stresses generated in T4 and T6 heat treated 6061 aluminium alloys, reinforced with silicon carbide particles, were sufficient to initiate fracture in the ceramic inclusions at the onset of strain localisation. Brechet, Embury, Tao and Luo [37] investigated the particulate damage events that arise during plastic deformation of an A356 aluminium alloy reinforced with 20 vol.% silicon carbide. They found that the probability of reinforcement failure was dependant on both size and aspect ratio, highlighting the importance of the inclusion Weibull modulus in damage initiation, when critical stresses are reached in the adjacent matrix.

Other researchers who have emphasised the dominant contribution of matrix constraint to strengthening in aluminium matrix composite include, Davidson [38,39], Pickard and Derby [40], Tvergaard [41], You, Thompson and Bernstein [42], Kobayashi, Iwanari, Kim and Yoon [43], Wang and Zhang [44] and Mummery and Derby [45].

2.2 Abrasion

2.2.1 *Abrasive wear of aluminium and aluminium alloys*

Aluminium and aluminium alloys generally exhibit poor wear resistances in abrasive environments when compared to other structural materials. Dry abrasion tests by Meyer-Rodenbeck, Ball and Hurd [46], showed that aluminium alloys have a quarter to half the abrasion resistance of mild steel, depending on their alloy content. For example, pure aluminium showed an abrasion resistance that was 0.22 times that of mild steel. The harder heat treatable alloys showed better abrasion resistances eg. 0.49 for the 7075 alloy, 0.4 for 2014 and 0.34 for 6061 aluminium alloys. Casting alloys tended to show poor microfracture properties as a result of coarse and brittle silicate phases and as a consequence, showed abrasion resistances close to 0.2 times that of mild steel.

2.2.2 *Abrasive wear of multi-phase microstructures*

The abrasion resistance of metals containing hard second phases or inclusions is in general, dependant on the test conditions used, the nature and properties of the abrasive, as well as the microstructure and mechanical properties of the heterogeneous material being abraded [47]. The early work on abrasive wear by Khruschov [48], examined the abrasive wear behaviour of several structurally heterogeneous materials. Using an abrasive that was harder than that of the structural constituents, he established that the wear resistance of heterogeneous materials such as brass-lead compositions, hypereutectic aluminium silicon alloys and annealed carbon steels of various compositions, were equal to the sum of products of the volumetric share of separate constituents, multiplied by their relative wear resistances. This "additive" correlation or rule-of-mixtures behaviour, was found to be limited in assessing the abrasive wear of brittle and porous materials such as metals containing metal carbides and hard alloys of tungsten carbide bonded with cobalt.

Khruschov's results provide the general impression that the abrasive wear behaviour of a metal matrix can be improved through incorporation of harder phases, despite some deviations from rule-of mixtures behaviour. This is indeed the case in the work of Zum Gahr and Eldis [49] who studied the effect of massive carbide size and volume fraction on the abrasive wear of white cast irons. The wear resistance of the cast irons was found to improve upon increasing carbide volume fractions when worn against 150 mesh garnet abrasives. However, the reverse was true when the same materials were worn against 180 mesh silicon carbide. This depreciation in wear resistance with

increase in carbide volume fraction, was attributed to the spalling of the massive carbides when penetrated by the harder silicon carbide abrasives.

A similar abrasive hardness effect was also reported by Zum Gahr [50] in abrasion tests conducted on tungsten carbide - cobalt matrix composites. Abrasion against very hard particles such as diamond or silicon carbide resulted in grooving and microcracking of the cemented carbides and substantially higher wear rates. Abrasive particles which were of equivalent or lower hardness than tungsten carbide (eg. alumina) were only partially able to penetrate the carbides, resulting in lower wear rates. Thus the hardness of the abrasive can become a crucial factor in determining the wear behaviour of metals reinforced with hard and brittle inclusions. In this regard, when abrasive hardnesses are increased to levels close to, or above that of the hard inclusions in a metal matrix, the microfracture of these inclusions can become rate determining. If wear resistance is to be maximised then the properties of secondary hard phases or inclusions also need to be optimised if possible, in order to resist fracture.

The two major parameters which affect the resistance to fracture in hard, brittle materials are their bulk hardness and fracture toughness values. Lawn and Evans [51] have shown that there is an absolute minimum load P, for fracture initiation which is primarily dependant on the ratio of the fracture toughness K, and hardness H, such that:

$$P = \theta(K^4/H^3) \qquad (2)$$

where θ is a constant. This relationship was developed for static indentation of bulk ceramics by hard indenters. When ceramic particulates are incorporated into a tough metal matrix, their susceptibility to fracture is reduced. This assertion was made by Almond, Lay and Gee [52] who compared the abrasion resistances of cemented tungsten carbide - cobalt materials and bulk ceramic materials of equivalent hardness. The bulk ceramics had higher wear rates compared to the composite structures, due to their tendency to form subsurface cracks of cone and median geometry accompanied by significant lateral cracking. These modes of fracture were rarely observed in the cemented carbides.

The complexities associated with compression failure of block specimens of brittle glassy materials were investigated by Kendall [53], who demonstrated that cracking of these materials is best described by fracture surface energy criteria as opposed to "compressive strength" parameters. Using both theoretical fracture surface energy considerations and experimental observations of axial crack propagation in glassy

materials, he demonstrated that the predicted force required to split a body depended on the size of the compressive platen, the size of the specimen and its elastic properties. Of interest was the observation that axial compressive splitting became impossible as the specimens were reduced in size compared to that of the compressive platen; a transition from splitting to plastic "squashing" of the specimen being observed. Compression cracking was also found to be inhibited through the application of lateral pressure on the sides of specimens; the lateral forces preventing crack propagation by inhibiting bending of the specimen as the crack grows. These observations have possible implications for abrasive wear of metals containing hard ceramic particles where the fracture criteria of reinforcing inclusions, may be affected by both the constraining effects of the surrounding matrix during abrasion, as well as the size and sharpness of the abrading particles.

The importance of the particle-matrix interfacial bond strength in wear of multiphase systems has been highlighted by Sim and Freti [54] and Zum Gahr [55]. Important micromechanisms such as cracking, wear debris formation and pulling out of reinforcing phases can take place at interfaces. In Simm and Freti's work, a two phase material comprising of spherical aluminium bronze (Cu-Al) particles embedded in an epoxy matrix, and a NiCrBSi alloy containing tungsten carbide particles, were worn against various grain sizes of silicon carbide bonded abrasive papers. The epoxy matrix composite, having weak particle-matrix bonding, exhibited particle pull-out as an additional contribution to the wear of both phases, once the depth of penetration of the abrasive particles reached that of the microstructural size of the Cu-Al inclusions. No pulling out of tungsten carbide grains was observed in abrasion conditions using both fine and coarse abrasives, although groove sizes remained smaller than the microstructural size of the hard carbides. From these observations, the researchers emphasised that the excellent interfacial bonding between matrix and inclusion in WC-Co cermets, was a dominant factor in improving wear resistance. Optimisation of wear resistance was also attained by increasing the volume fraction and microstructural size of the hard phase.

2.2.3 *Abrasion of aluminium matrix composites*

Aluminium matrix composites have been found to outperform their matrix alloy counterparts in a wide variety of abrasive wear conditions. Banerji, Prasad, Surappa and Rohatgi [56] assigned a simple rule of mixtures behaviour to an aluminium alloy (Al- 11.8 Si - 4 Mg) containing zircon particulates with a mean diameter of 100μm in abrasion tests against 80 mesh alumina grit impregnated paper. Rule of mixtures wear

behaviour was found in alloys containing volume fractions of reinforcement above 0.09. Below this critical volume fraction, the wear resistance of composites were similar to that of the matrix alloy. The greatest wear resistance was attributed to the reinforced alloy with the highest hardness and reinforcement volume fraction of 0.35. Using the data published by Banerji et al, this composite displayed an average wear resistance, calculated relative to that of the unreinforced matrix alloy, of 1.4 when abraded against fresh abrasive and at various loads up to 10N. Interestingly, the relative wear resistance of this composite improved to around 2.4 after some ten passes over the same abrasive wear track. Similar trends were observed in alloys containing lower concentrations of reinforcement down to fractions of approximately 0.09. This improvement in wear resistance of the composites relative to that of the unreinforced alloy, was attributed to the degradation and blunting of the abrasive particles brought about by the mutual abrasion between the zircon reinforcement and alumina abrasive.

Banerji et al [56] highlight the fact that during abrasion with fresh abrasive, the indentation by sharp alumina particles first produces plastic deformation followed by fracture of the ceramic reinforcement when the indentation reaches a critical size; the size of the indent required to initiate fragmentation being greater for blunt indenters than for sharp ones. Worn surfaces of these composites displayed reinforcing particulate fracture but there was no evidence of particulate pullout or debonding at particle-matrix interfaces.

Surappa, Prasad and Rohatgi [57] compared the abrasive wear resistance of pure aluminium reinforced with 100μm alumina particulates (3wt.% and 5wt%), with those of unreinforced pure aluminium, a reinforced (5wt.% Al_2O_3) and unreinforced Al-Si eutectic alloy, and an unreinforced Al-Si hypereutectic alloy. The materials investigated were worn against 80 mesh alumina abrasive belts at various loads. The reinforced pure aluminium alloys greater wear resistances compared to the Al-Si reinforced and unreinforced alloys despite having lower hardness values. Likewise, the reinforced and unreinforced Al-Si alloys had wear rates of up to approximately 1.25 times that of pure unreinforced aluminium. The high wear rates of the Al-Si alloys were attributed to extensive chipping of the silicon phase during abrasion, which is in common with the findings of other researchers [46,58].

Wang and Hutchings [7] conducted two body abrasive wear tests on a 6061 aluminium alloy reinforced with up to 30 vol.% discontinuous alumina fibres. The wear resistance of the composites was found to increase with added reinforcement, up to a volume fraction of approximately 20% fibres, when abraded against large silicon carbide abrasive particles (240 mesh - 60μm mean diameter). An alloy containing additional reinforcement (30 vol.%) displayed a subsequent decrease in abrasion resistance.

When the composites were abraded against fine silicon carbide abrasive particles (600 mesh - 20μm mean diameter) a linear increase in wear resistance with increasing fibre volume fractions was obtained. Under these low contact stress conditions, wear rates of up to six times below that of the matrix alloy were displayed. The transition from high contact stress (large abrasive grit sizes) to low contact stress conditions (small abrasive grit sizes) was accompanied by a change in wear mode from extensive fibre fracture and debonding to plastic deformation and minimal fibre damage respectively. Using parameters such as fibre tensile strength, fibre dimensions and calculated contact pressures present at abrasive grit contact points, a model was developed to determine the critical abrasive particle size required to initiate fibre fracture in the aluminium matrix. A critical abrasive grit diameter of 30-35μm was obtained from the model, which correlated reasonably well with the experimentally observed value of 20-28μm.

Prasad, Rohatgi and Kosel [8] conducted low stress abrasion tests using a rubber wheel abrasion apparatus (ASTM G65) with quartz (50-70 mesh) as abrasive on Al-11.8Si-4.0Mg zircon particulate composites. Wear rates five times below that of the unreinforced matrix alloy were obtained with an alloy containing 35 vol.% particulates, showing a marked deviation from rule of mixtures behaviour observed under high stress two-body abrasive conditions by Banerji et al [56]. The surfaces of the composites abraded under low stress conditions displayed minimal damage (microfracture) of the zircon particulates, which tended to stand proud of the surrounding matrix alloy.

The abrasive wear behaviour of SiC whisker, SiC particulate and SiC short fibre reinforced 6061 aluminium was investigated by Zongyi, Jing, Yuxiong, Hangwei and Yinxuan [9]. Fine grit sizes (600 and 400 mesh) of emery (alumina) paper were used as the abrasive medium. Wear rates which were an order of magnitude below that of unreinforced 6061 alloy were reported for an alloy containing a mixture of both fibres (4.4 vol%) and particulates (15.5 vol.%) worn against 600 mesh paper. This composite also displayed a constant wear rate at different loads, unlike that of the alloys containing lower volume fractions of reinforcement.

Investigations into the abrasive wear behaviour of silicon carbide particulate and whisker reinforced 7091 aluminium alloys by Wang and Rack [10], found similar improvements in wear resistance over that of the unreinforced matrix alloy, with the greatest improvements found for abrasion against finer abrasive particles. They proposed that the ratio of the average abrasive penetration depth to the size of the reinforcing particulates, was the critical parameter controlling the relative abrasive wear resistance of the silicon carbide reinforced composites. Thus it becomes apparent that by reducing asperity sizes and contact stresses, the probability of catastrophic failure of reinforcing particulates in an aluminium matrix is diminished. The reinforcement

becomes load bearing and material loss occurs through plastic deformation and ductile removal of the matrix alloy accompanied by microfracture of the reinforcing particulates.

2.3 Sliding Wear

2.3.1 *Sliding wear of aluminium and aluminium alloys*

The use of commercial aluminium alloys in the engineering industry is widespread, where low density, toughness and corrosion resistance are their most attractive qualities. However the tribological behaviour of aluminium and aluminium alloys is notoriously poor, particularly in unlubricated sliding wear situations where the transition from mild oxidational wear to catastrophic seizure and wear loss, is found to occur at low loads. In view of these effects, aluminium alloys are most likely to be used under low load lubricated sliding conditions, often requiring advanced component designs so as to minimise high contact loads or 'hot spots' and ensure sufficient lubrication at the sliding interface. Improved seizure resistance of aluminium alloys is obtained through alloying (eg. Al-Si alloys, which are widely used in the auto industry), as well as surface treatments such as anodising and improving the choice of counterface used [59].

2.3.2 Sliding wear behaviour of aluminium matrix composites

Tribological environments in which contacting asperities are no longer able to indent the surface to an extent that substantial material removal occurs, can be referred to as sliding or "adhesive" wear conditions [47]. The expected behaviour of aluminium composites in sliding wear situations can be partially inferred from their performance under low stress abrasion; the markedly reduced contact stresses and resulting minimal damage to the load bearing reinforcement should result in very low material removal rates. Nevertheless, variables such as sliding speed, contact temperature, tribo-chemical environment and the magnitude of frictional stresses developed at the sliding wear interface can become rate controlling factors [60].

A common feature of investigations which involve sliding contact between aluminium matrix composites and steel surfaces, is a lowering of the amount of transfer of aluminium to the steel, resulting in reduced wear rates. Hosking, Portillo, Wunderlin and Mehrabian [61] conducted pin-on-disk sliding wear experiments on silicon carbide and alumina reinforced 2024 and 2014 aluminium alloys. A steel ball bearing was loaded against rotating discs of each of the unreinforced matrix alloys and reinforced alloys containing different fractions of up to 20 wt.% particulates. The composites

displayed an overall trend of decreasing wear rates with increasing reinforcement contents. Wear rates of up to two orders of magnitude below the unreinforced alloys were obtained for the composites with 20 wt.% of silicon carbide and 20 wt.% alumina. While the wear mechanism for the unreinforced alloy was described as purely adhesive, showing metal transfer to the steel bearing pin, that for the composites was of a mixed abrasive-oxidative nature, with the steel ball against which the composites were loaded undergoing significant abrasive wear. Alloys which were reinforced with silicon carbide showed superior wear resistances compared to the alumina reinforced materials; this was attributed to the greater hardness of silicon carbide compared to the softer alumina.

Other investigations involving aluminium matrix composites sliding against hardened steels have reported similar features to those of Hosking et al [61]. Rana and Stefanescu [62] recorded reductions in sliding friction coefficients from 0.63 for a monolithic Al-1.5% Mg alloy, to values of 0.24 (15wt% SiC) through additions of silicon carbide particulates to this alloy, during sliding tests against a tool steel rotating disc in air. Composites with smaller average particulate sizes displayed lower frictional forces in comparison to alloys containing the same volume fraction. The reduction in friction coefficient was attributed to the greater surface area of silicon carbide in contact with the steel and less cutting action afforded by the resultant lower contact stresses.

Yang and Chung [63] recorded decreased wear rates during sliding wear of an Al-Si eutectic alloy which had been reinforced with bauxite particulates. The wear tests were conducted on a pin-on-disc apparatus under dry sliding conditions against a hardened (50HRC) steel counterface. Alloys containing 20 wt.% bauxite displayed wear rates which were comparable to those of annealed mild steel under similar sliding conditions. The addition of 3 wt.% graphite particles into an 8 wt.% bauxite reinforced alloy displayed a wear rate some seventeen times below that of the unreinforced matrix alloy, producing a layer of graphite solid lubricant on the steel surface.

Surappa et al [57] determined the sliding wear behaviour of pure aluminium, eutectic, and hypereutectic Al-Si alloys, each reinforced with up to 5wt.% alumina particulates. The composites and unreinforced alloys were worn against a hardened steel disc (57HRC) under dry sliding conditions on a pin-on-disc apparatus. Each of the alloys displayed a linear decrease in adhesive wear rate with added reinforcement, with the 5 wt.% reinforced alloys each showing wear resistances some seven times that of their matrix alloys in the case of the Al-Si composites, and two and a half times in the case of the reinforced pure aluminium. The composites displayed higher wear resistances in comparison to those of Al-Si alloys of similar hardness.

Anand and Kishore [64] characterised the wear behaviour of an Al-10% Zn alloy reinforced with different volume fractions of corundum particulates up to 40 wt% content. Wear tests were conducted on a pin-on-disc machine with the composites and unreinforced alloy specimens being loaded against a high chromium hardened steel disc (63HRC) in dry sliding. The wear rates of the composites were found to decrease with higher corundum contents with as little as 5 wt% particulates providing a seventeen-fold decrease in wear rate over that of the unreinforced matrix alloy. Subsurface metallographic sections of the worn composites revealed cracking and delamination of heavily sheared material below the worn surface. A delamination wear mechanism, similar to that observed by Suh [65], was considered to be operative under the experimental conditions. Edax analysis of worn composite surfaces and subsurface regions showed the presence of steel debris which had been sheared from the counterface during sliding wear.

In contrast to the general observed trend of improved sliding wear resistance with added ceramic reinforcement, Saka and Karalekas [66] noted a significant reversal of this trend in copper reinforced with different volume fractions of alumina particulates (45-53μm in diameter). The composites displayed increased wear losses with higher reinforcement contents of up to 40 vol.% alumina, during dry sliding wear against a tungsten carbide - cobalt coated steel ring. The wear resistance of the 40 vol.% alumina composite was some five times below that of unreinforced copper. Delamination of surface material was considered to be the dominant wear mechanism for the composites although no evidence of subsurface cracking could be found. The researchers postulated that subsurface cracks were propagating in the near surface regions of each composite, making their detection difficult. Other considerations which were attributed to the lowered wear resistance in the composites, were their loss of ductility with added reinforcement and poor matrix-particulate interfacial bonding.

It is interesting to note that while most sliding wear experiments conducted with metal matrix composites tend to involve their being worn against hardened steel counterfaces, the tests by Saka and Karalekas [66] involved loading the copper composites against a very hard tungsten carbide - cobalt counterface (hardness 13730 MPa). An increase in counterface hardness would diminish the probability of any counterface material from being abraded and transferred to the composite surface. In addition, the probability of microfracture of alumina reinforcement is increased when loaded against the very hard cermet counterface. Large rises in temperature at the wear interface would also be expected in the experiment detailed by Saka and Karalekas [66]. This is due to the high flash temperatures generated during sliding contact between ceramics, which in this instance is between the alumina reinforcing particulates and the tungsten carbide ceramic phase of the counterface. Further additions of ceramic reinforcement to the

copper matrix would only exacerbate the heating effects from high flash temperatures at the wear interface resulting in increased wear losses. In this regard it would be of interest to see whether alumina or silicon carbide reinforced aluminium alloys show similar losses in wear resistance to those exhibited in Saka and Karalekas' results, when they are worn against hard ceramic counterfaces.

The addition of ceramic particulates to aluminium matrices not only improves their sliding wear performance but also has a marked effect on their bulk mechanical properties. In particular, alloys reinforced with increasing volume fractions of ceramic reinforcement show significant reductions in ductility and fracture toughness. Some recent investigations have shown that the sliding wear resistance of composites having low strains to failure are reduced to levels close to those of their unreinforced states. Pan, Fine and Cheng [11] compared the performances of an A356 Al-Si casting alloy reinforced with 15 vol.% SiC particulates and a 2014 aluminium alloy containing 15 vol.% alumina particulates in both lubricated rolling and sliding wear tests. Both of the composites displayed exceptionally low wear rates of around 10^{-9} mm^3m^{-1} in sliding contact (block on ring) against 52100 steel. This behaviour was attributed to the constant abrasion stresses associated with the sliding contact and the development of a stable surface transfer layer of high iron concentration especially in the alumina reinforced composite. In contrast, the two composites had rolling wear resistances (MMC roller loaded against nodular cast iron cylinder) which were some 10 to 20 times lower than their sliding wear resistances. The diminished performance of the two composites was related to the cyclic loading associated with rolling contact which induced the formation of fatigue-like cracks in the subsurface wear region, leading to severe microcracking and loss of material by pitting. The researchers reported rolling wear rates for the A356 composite which were double that of the 2014 matrix composite, attributing this to the lower matrix strength and ductility (317 MPa and 0.3% elong.) compared to the 2014 matrix composite (476 MPa and 2.3% elong.) which is able to resist crack propagation and particle pull-out more effectively.

Alpas and Embury [12] reported similar wear resistances for a 2014 aluminium alloy reinforced with 20 wt.% SiC particulates and a monolithic 2024 alloy in dry sliding (block on ring) contact against a bearing steel ring. They inferred that the low ductility and fracture toughness of the reinforced alloy, irrespective of its higher hardness, were responsible for controlling its wear resistance. While the monolithic alloy exhibited extensive strain accommodation beneath its sliding surface, the reinforced alloy had a very large subsurface strain gradient accompanied by cracking along particle matrix interfaces. Material loss in the composite was thus attributed to the delamination of subsurface layers along which cracks had propagated, and not adhesive transfer to the slider, as was found for the monolithic alloy. The continued exposure of reinforcing

particulates by delamination of the surface layers of the composite was suggested as being the major reason for increased abrasion of the steel counter material. The addition of a lubricating oil to the sliding wear interface of both the composite and unreinforced matrix alloy, was found to decrease the subsurface strains and damage accumulation to such an extent that wear rates of the composite were an order of magnitude below those of the monolithic alloy.

A subsurface delamination wear mechanism was also reported by Alpas and Zhang [13] in investigations involving the dry sliding of silicon carbide reinforced A356 aluminium alloys against hardened bearing steel (block on ring apparatus). This mode of material loss was observed in alloys containing 10 - 20 vol.% SiC under conditions where the applied load was raised above a critical value and fracture of reinforcing particulates at the wear surface began. Under these conditions, the composites displayed wear rates which were similar to the unreinforced A356 matrix alloy. The researchers attribute the deterioration in wear resistance of the composites to the inability of fractured SiC particulates to remain as load bearing components, resulting in large shear strains being transmitted to the matrix alloy accompanied by subsurface cracking and delamination. The transition to poor wear resistance of the reinforced alloys is dependant on the volume fraction of particulates, with the alloys having low reinforcement contents undergoing the deterioration at lower loads than those observed for composites having higher volume fractions.

Subsurface cracking assisted wear modes have also been reported by Wang and Rack [14] at high sliding speeds in dry sliding wear tests on 7091 aluminium reinforced with SiC particles and whiskers. They suggested that the growth of subsurface cracks was attributable to shear instabilities arising from friction induced thermal softening at sliding velocities greater than 1.2 ms^{-1}. Modi, Prasad, Yegneswaran and Vaidya [67] also reported subsurface cracking at SiC fibre/matrix interfaces in silicon carbide reinforced Al-4.5% Cu alloys under sliding wear conditions against steel.

2.3.3 Transfer phenomena and subsurface deformation in aluminium matrix composites

One of the more commonly observed phenomena associated with materials in sliding contact with each other, is the transfer of material between surfaces to form what is generally referred to as the transfer layer or tribo-layer. Transfer of slider and counterface material generally occurs in both directions and is usually found in most metal-metal sliding couples. When aluminium and its alloys are brought into sliding contact with steel surfaces, under loading conditions which break up the protective oxide layer in the severe metallic wear regime, a transfer layer of aluminium forms on

the counter surface. [68-70]. The build-up of this transfer layer on the steel counter material leads to a situation where the aluminium slider eventually ends up sliding against a surface that is also mostly aluminium. The generation of wear debris from such a sliding couple is primarily dependant on factors such as the alloy content of the aluminium and its ability to accumulate strain energy at the wear interface, together with sliding condition variables such as load, speed, contact geometry, presence of a lubricant and counterface hardness and roughness. The composition of the transfer layer is predominantly aluminium but small concentrations of iron from the steel counterface can become incorporated into its microstructure [68]. Studies on other metal-metal sliding couples have shown that their friction and wear behaviour can be significantly affected by the formation of wear transfer layers [71]. The composition of transfer layers can be correlated with the cohesive strengths of each metal where the direction of transfer is usually from the cohesively weaker to the cohesively stronger material. The transfer layer is thus composed of very finely mixed fragments of both sliding materials whose composition correlates closely with that of the wear debris generated by the system [71-73].

The presence of ceramic particulate or fibre reinforcement in aluminium alloys incorporates an additional abrasive wear component into their sliding wear behaviour. This is evident in the commonly observed loss of steel counterface material due to the abrasive action of the ceramic reinforcing particulates, during sliding contact. Thus the composition of any transfer layer formed on composite surfaces, would be reflected by higher levels of counter material in their microstructures compared to that observed for monolithic alloys sliding on steel. In addition, the abrasive action of the reinforcing phase prevents the formation of a transfer layer developing on the opposing counter surface, particularly in composites which have high levels of reinforcement. The formation of transfer layers, their composition and their influence on composite wear rates have yet to be systematically investigated.

Several researchers have reported the development of a transfer layer on the surfaces of aluminium composites which have been in sliding contact with steel counter materials [11-14,64,74-76]. Common to each of these investigations is the observation that the transfer layers are formed under "mild" sliding conditions which is concurrent with composites displaying improved wear behaviour over that of their respective unreinforced matrix alloys.

You, Donlon and Boileau [74] characterised the nature and formation of the transfer layer in an Al2124 aluminium alloy reinforced with 20 vol.% silicon carbide particulates in dry sliding conditions against a hardened 1045 steel disc (pin on disc arrangement). In the early stages of wear, the load bearing silicon carbide particulates remove

counterface steel material in an abrasive 'micromachining' operation. The steel debris generated by this process is compacted between the reinforcing particulates followed by mechanical mixing and plastic deformation, giving rise to a 'steady state' transfer layer. TEM examination of the transfer region revealed large variations in both microstructure and composition. Some areas had an extremely fine grained structure (5-20nm) with selected area diffraction patterns consisting of several broad rings which corresponded closely with the d-spacings of aluminium, iron and silicon carbide. Other areas of the transfer layer had larger grain sizes of aluminium and iron (30-100nm) together with silicon carbide particles of around 100-500nm in size.

A substantial degree of subsurface deformation was also found in the composite material, immediately below the wear transfer layer [74]. Subsurface examination of the worn composite revealed large strain gradients below the worn surface indicating that large shear stresses are generated in this region; estimations of plastic shear strain in the near surface regions were estimated to be around values of ten. TEM examination of foils prepared in transverse section to the worn surface, revealed high dislocation densities to depths of approximately 150μm in the aluminium matrix. Evidence for dislocation arrangement into cells elongated in a direction parallel to that of the sliding direction were observed at depths of around 25μm below the worn surface. The aluminium matrix grains below the cell structure did not show this substructure, but were characterised by high uniform densities of dislocation tangles.

In Alpas and Zhang's [13] tests involving silicon carbide reinforced A356 alloys in dry sliding contact with a steel counterface, the formation of an iron rich transfer layer on composite wear surfaces at low loads (below 0.2 MPa nominal contact pressure) was reported. X-ray analysis of transfer material found that it consisted primarily of iron oxide (α-Fe_2O_3) and silicon carbide debris. Upon increasing the contact pressure to above 1.6 MPa, wear rates of composites increased to those of their respective matrix alloys and very little transfer material was found on the composite surfaces.

The dry sliding pin on disc wear tests conducted by Wang and Rack [14] involving silicon carbide reinforced 7091 aluminium alloys loaded against a stainless steel counter material, also reported the formation of a wear transfer layer. They describe the sliding conditions used as being "mild", with sliding speeds below 1.2ms^{-1} and a nominal contact pressure of 0.43 MPa, despite obtaining wear rates for the composites which were of the same magnitude as the unreinforced matrix alloy. X-ray analysis of wear debris from composite surfaces was found to be metallic in nature, consisting of mechanically mixed iron and aluminium. The researchers proposed that the non-oxide nature of the debris was an indication that "fatigue-related surface cracking" was the predominant wear mechanism. However, there is little evidence given to support a surface fatigue-

cracking mechanism, or to suggest that debris formation could not have occured by mechanical mixing and shear failure of the surface material.

Caracostas, Chiou, Fine and Cheng [75] examined the surface and subsurface microstructural phenomena associated with an aluminium 2124 alloy, reinforced with 15 vol.% TiB_2 particles (1.3 μm diameter), in lubricated sliding against a 52100 steel ring (block on ring). TEM examination of foils prepared in cross section to the worn surface and parallel to the sliding direction revealed microfracture of the TiB_2 particles, accompanied by a high dislocation density in the matrix alloy beneath the wear track. The dislocations were arranged in dense tangles with no evidence of subgrain or cell substructures being present. The researchers did not report whether any transfer layers were formed, although such phenomena were absent from their micrographs.

The sliding wear tests conducted by Pan, Fine and Cheng [11] on alumina reinforced 2014 aluminium and silicon carbide reinforced A356 alloys, in sliding contact against 52100 steel, also reported the formation of iron rich transfer layers on the worn composite surfaces. The worn surface of the alumina reinforced composite had a much higher iron concentration (17 wt.%) in comparison to that of the silicon carbide reinforced composite (5 wt.%), after being worn to steady state under dry sliding conditions. The researchers attributed the high iron content on the alumina reinforced composite transfer layer, to the chemical reaction between the oxide surface of particulates and the steel counter surface. In this reaction, the freshly exposed iron surface reacts with the high oxygen content alumina surface to produce an alumina-iron oxide interface.

Other researchers, who have reported the transfer of steel counter material to the worn surfaces of reinforced aluminium composites in sliding wear tests, include Alpas and Embury [12], Anand and Kishore [64] and Wilson and Ball [76].

2.4 Solid Particle Erosion

The erosion of materials by solid particle impact is of particular importance in many technological applications, where components are exposed to gas or liquid borne erosive particles. The severity of erosion is dependant on several factors which include the size, velocity and frequency of impact of erosive particles as well as the mechanical properties of both the target and erodent materials. Most industrial environments involve impacts in the 5 to 500ms^{-1} range, where damage to metals and ceramics can be severe.

The erosive wear mechanisms found in ductile metals generally include damage accumulation processes, where the target material absorbs and accumulates strain energy by work hardening and ductile rupture, accompanied by erosive cutting or ploughing type modes of material removal [77,78]. Brittle ceramic materials on the other hand, respond to impact by hard particles at high speeds by localised plastic accommodation around the impact centre accompanied by arrays of radial, lateral and median cracks associated with the plastic impression [79-80]. The intensity of material removal depends on the frequency of impacts as well as target variables such as hardness (including hardness relative to that of the erodent [81]), fracture toughness and intrinsic flaw populations [79].

The erosion behaviour of alloys containing a second harder phase was studied by Hovis, Talia and Scattergood [82]. Using the Al-Si alloy system as a model, they demonstrated that the erosion resistance of these materials can be analysed in terms of mechanism-independant averaging laws, if the size of the erosion impact events are small relative to that of the microstructural constituents. Deviations from this behaviour occurred with increases in erodent particle size. These deviations were attributed to a change in the erosion mechanisms, where microstructural criteria such as interface bond strength, and ductility constraints imposed by hard second phase inclusions, played a major part in influencing material losses. However, this theory disregards the fact that erodent particles, no matter how small, will always hit both the constituents and interfaces; changes in erosion mechanisms would therefore arise from changes in target response as opposed to erodent size when the impact stresses are increased or decreased. Very small particles can initiate extensive damage and high material losses if their impact velocities are high eg. meteorite particle in space travelling at 30000kmh^{-1}.

Ninham [83] tested the solid particle erosion resistance of abrasion resistant cobalt based (*Stellite*) and iron based (*Tristelle*) alloys, whose microstructures contained discrete carbide phases. The erodents used were silicon carbide (60 grit) and quartz (75-200μm) using a particle velocity of approximately 60ms^{-1} in an air-blast type rig. Results from these tests indicated that an increasing carbide volume fraction caused an increase in erosion rate. The depreciation in erosion resistance was attributed to the disruption of plastic flow of the matrix alloy caused by the carbides. The inhomogeneous nature of the plastic flow resulted in very high strain gradients and void formation near carbides accompanied by carbide cracking and high rates of material removal.

When the magnitude of strain energies imparted to metal matrix composite surfaces is dramatically increased, as is the case with high velocity solid particle impact, their

ability to accommodate strain becomes rate determining. Goretta, Wu, Routbourt and Rohatgi [84], studied the erosion by alumina particles of cast 2014 aluminium alloys reinforced with 20 vol.% silicon carbide and 20 vol.% alumina inclusions respectively. The steady state erosion rates of the alumina and silicon carbide reinforced alloys were similar for a range of erodent sizes and impact velocities, but markedly greater than those of the unreinforced matrix alloy. Lack of ductility was ascribed as being the major reason for reduced erosion resistance in the composites, with properties such as hardness and elastic modulus being of little influence. Similar findings have been made by Hutchings and Wang [85], who studied the solid particle erosion resistance of 6061 aluminium reinforced with up to 30 vol.% discontinuous alumina fibres. The extent to which fibres had fractured during particle impact was described as the dominant erosion rate controlling factor.

Srinivasan, Scattergood and Warren [86] conducted erosion tests on a series of Al-4% Cu matrix composites containing up to 30 vol.% alumina fibres, using alumina particles as the erodent. These composites also exhibited higher erosion rates with increasing fibre contents. A characteristic feature of the observed wear modes were the increased ductility constraints associated with composites having greater fibre contents. The erosion rates of these materials showed an inverse correlation with work to fracture parameters (ultimate tensile strength multiplied by strain to failure) calculated from their respective tensile test data. However, Wu and co-workers [87] in an extension of their work in ref.[84] stipulated that the product of strength and ductility is not very useful in predicting erosion rate, and that local properties of composite microstructure (eg. inclusion size, shape, angularity) were more important than basing models of composite erosion on macroscopic properties. Their reasoning was based on the similarity in erosion rates between their particulate reinforced composites and those of Srinivasan et al [86], which are fibre reinforced; the particulate composites apparently having comparable strengths, but higher ductilities, than the fibre reinforced materials (although tensile data was not published by Wu et al [87]). It was postulated that the relatively high erosion rates in the particulate reinforced composites arose due to the deleterious effect of local stress concentrations, attributable to sharp edged particulate morphologies, a feature which was less evident in the rounded and continuous nature of the fibres. Another factor which could influence the erosion response of these materials is the strength of the interfacial bond between matrix alloy and ceramic reinforcement, the nature of which would change according to type of ceramic used, the aluminium alloy chemistry and possibly inclusion morphology.

2.5 Cavitation Erosion

Another common form of erosive wear is cavitation erosion, which often affects engineering components used in liquid environments eg. pump impellers, pistons, bearings, valves and ships propellors. Cavitation is the repeated formation and collapse of bubble cavities arising from high frequency pressure disturbances in a liquid medium. Early work on cavitiation by Lord Rayleigh [88] estimated that pressures close to 10300 atmospheres (1.04 GPa) could be generated by the collapse of a cavity in water. Vyas and Preece [89] established that the stresses generated during erosion are due primarily, to the collapse of whole clouds of bubbles created by pressure changes in the liquid. The stress pulse thus generated has the characteristics of a shock wave, the magnitude of which determines the level of elastic and plastic deformation in the surface regions of the material being eroded. Vyas and Preece also stipulated that cavitation damage models invoking microjet impingement by individual bubbles [90], were negligible in vibratory cavitation systems, but could become responsible for a greater portion of the damage in flowing liquids undergoing cavitation eg. venturi systems. More recently, Chen, Kuhl and Israelachvilli [91] monitored the formation and collapse of cavities in thin liquid films using a surface forces apparatus technique and time-lapse video. They established that the sudden nucleation and growth of cavities is associated with the relaxation of high local stresses on nearby rigid surfaces and that it is this nucleation and growth phase which is responsible for most damage, rather than cavity collapse.

Heathcock, Protheroe and Ball [92], studied the behaviour of a wide range of materials in cavitation erosion conditions. They established that improved performances were attained by materials with one or more of the following properties: a high elastic resilience, a high resistance to the accumulation of fatigue damage under repeated shock loading conditions, a tough microstructure which is resistant to the propagation of microcracks. Aluminium alloys generally have low resistances to cavitation erosion [93], due to their inability to absorb impact energy in an elastic manner. An aluminium 6061 alloy reinforced with 20 vol.% silicon carbide particulates displayed an erosion resistance which was slightly above that of its unreinforced state [76]; the presence of high modulus silicon carbide reinforcement possibly improving the elastic resilience of the alloy to a certain degree. Filler materials may also provide regions of elastic modulus mismatch and plastic strain mismatch in a matrix and can act as nuclei for rupture [85], giving higher wear rates. However, the excellent bond between ceramics such as silicon carbide or alumina, and aluminium [14,38], lowers the possibility of interfacial rupture; although rupture arising arising from plastic strain mismatch effects, next to the strong interfaces, may result in increased material losses. The influence of reinforcing particulate fracture toughness and composite failure strain on cavitation erosion resistance, still need to be determined however.

3.0 Materials and Experimental Methods

3.1 Materials

The materials investigated consisted of the aluminium alloys 6061 (1.0 Mg, 0.6 Si, 0.2 Cu, 0.2 Cr in wt. %) a commercial structural extruding alloy, and 2014 (4.4 Cu, 0.8 Si, 0.4 Mg, 0.8 Mn in wt. %) an extruding alloy used widely in aerospace structures, each reinforced with 10, 15 and 20 vol.% alumina particulates. The 6061 alloy was also reinforced with 20 vol.% SiC particulates. Both of the unreinforced alloys were fabricated by Hulett Aluminium Ltd., Pietermaritzburg, South Africa and supplied in extruded bar form. The reinforced alloys were manufactured by Duralcan Composites Co. (Alcan) in San Diego, USA and extruded into bar stock by Hulett Aluminium Ltd. in South Africa. The cross-sectional dimensions of the composites and monolithic alloys extruded bar stock are shown in Table I. The unreinforced alloys and composites were extruded into rectangular or round bar form, with the exception of the 10% Al_2O_3 reinforced 6061 alloy, which was supplied as extruded "H" bar.

Alloy	Width (mm)	Thickness (mm)	Diameter (mm)	Cross Section
6061 0 vol.%	51	16	-	rectangular
6061 10 vol.% Al_2O_3	-	3	-	H section (63x45x45)
6061 15 vol.% Al_2O_3	40	20	-	rectangular
6061 20 vol.% Al_2O_3	40	20	-	"
6061 20 vol.% SiC	51	16	-	"
2014 0 vol.%	51	16	-	"
2014 10 vol.% Al_2O_3	51	16	-	"
2014 15 vol.% Al_2O_3	-	-	27	round bar
2014 20 vol.% Al_2O_3	-	-	27	"

Table I: Extruded bar stock cross-section dimensions for each of the reinforced and unreinforced aluminium alloys.

Before specimens for wear and tensile testing could be prepared, preliminary heat treatment tests were conducted on each of the reinforced and unreinforced alloys in order to determine their respective ageing characteristics. There is sufficient evidence in the literature [32,33] which demonstrates that the incorporation of ceramic particulate or whisker reinforcement into age hardening aluminium alloy matrices, leads to accelerated ageing of the matrix compared to the unreinforced matrix alloy. Thus, if comparative studies are to be made on the mechanical and wear behaviour of the reinforced and unreinforced alloys, then it is imperative that their respective matrix

microstructures are in a similar heat treated condition.

3.1.1 *Preliminary heat treatment*

Coupon specimens, 14mm in diameter and 4mm thick, were machined from bar stock of the composites and monolithic alloys. One side of each specimen was wet-ground on SiC abrasive pads to a 1000 grit followed by diamond polishing to a 3μm finish. The 6061 matrix alloy and composites were solution treated at 520°C for one hour followed by a water quench to room temperature. Each specimen was then placed into an ageing furnace at 175°C and artificially aged within 15 minutes of quenching. In a similar routine, the 2014 composites and matrix alloy were solution treated at 495°C for one hour, followed by a water quench to room temperature and artificial age at 175°C (see Results section).

Bulk hardness tests were conducted on each material at specific intervals during the ageing treatment using a Vickers diamond indenter and 20kg load. The time required for each specimen to attain its maximum hardness (T6 condition) during artificial ageing was then determined from their respective hardness vs. ageing time curves.

3.1.2 *Heat treatment*

The composite and monolithic specimens for wear and tensile testing were solution heat treated for one hour at 520°C and 495°C for the 6061 and 2014 matrix materials respectively. Following a water quench, each material was then artificially aged at 175°C to peak hardness (T6) according to their respective ageing time vs. hardness curves, determined during preliminary heat treatment tests.

3.1.3 *Composite microstructures*

Specimens of each composite were wet-ground and diamond polished to a 0.25μm finish in order to obtain representative microstructures. Average particulate sizes were measured using the mean linear intercept method [94] on optical micrographs of each composite.

3.1.4 *Matrix microhardness tests*

In order to ascertain whether the matrix alloy of each composite had been artificially aged to the same strength as that of its parent monolithic alloy, microhardness tests were conducted on the interparticulate matrix alloy of each composite and their respective monolithic alloys, after having been heat treated to peak aged conditions.

Specimens of each alloy composition and reinforcement content were chosen at random from the items which had been aged to their respective peak hardnesses. Each sample was then cold mounted in epoxy resin, wet-ground down to 1000 grit on SiC pads, followed by diamond polishing to a 0.25μm finish. Care was taken to reduce the excessive fragmentation of reinforcing particulates during wet grinding by applying low specimen contact pressures to the grinding surface. Ceramic fragments were removed from inter-particulate matrix regions by successive polishing with 3μm, 1μm and 0.25μm diamond grits accompanied by rubbing the specimen surfaces with an alumina suspension (1μm). A weak hydrofluoric acid solution (approx. 2%) was also used to remove reinforcement fragments from the interparticulate regions followed by diamond polishing. Each specimen was thoroughly cleaned by ultrasounding in absolute ethanol for several minutes.

In interparticulate matrix microhardness tests conducted by Christman and Suresh [32,33] on SiC reinforced 2124 alloys, the composites were mechanically polished followed by electropolishing to remove surface residual stresses and reinforcement debris. An attempt was made to use this procedure on the 6061 and 2014 composites and matrix alloys by electropolishing them in an 80:20 methanol/nitric acid mixture at -30°C and 15V applied potential, after mechanical polishing. However, despite obtaining an excellent matrix alloy polish for all the materials, microhardness readings of interparticulate metal could not be obtained for the 15 and 20 vol.% reinforced alloys. This was due to the microhardness indenter being prevented from reaching the specimen surface, by particulates standing proud from the specimen surface as a result of the electropolishing procedure.

Matrix microhardness measurements were thus made on the mechanically polished, reinforced and unreinforced alloys on a *Shimadzu* microhardness tester using a Vickers diamond pyramid indenter and a 15g load. A minimum of twenty indents per sample were made in particulate free regions of each composite and on the monolithic alloys. Anomalously high readings were attributed to particulates being in the indented region and were thus discarded.

3.1.5 *Young's modulus determination*

The Young's elastic modulus of each composite and monolithic alloy was determined using the in-plane resonance spectra of disc specimens of each material. The in-plane resonance spectra of thin discs are well known and numerical solutions are readily available [95,96]. Disc resonances fall into two categories. In the first, the distortion modes are nodal diameters which divide the disc into slices, where adjacent slices vibrate in and out in reverse phase. The area of the specimen remains unchanged. In the second category, the whole disc periphery expands and contracts, resulting in an area change (radial mode). Comparisons of resonance frequencies from distortion mode and radial mode measurements gives Poisson's ratio with good sensitivity. Young's modulus values can then be calculated using standard formulae which incorporate the density, Poisson's ratio and radial diameters of each disc specimen.

The transmission line technique used to determine resonant frequencies of disc specimens, was that developed for material characterisation up to high temperatures [96]. One end of a long annealed nickel wire of diameter 0.7mm was connected into a hole of similar diameter on the edge of 14mm diameter disc specimens of each reinforced and unreinforced aluminium alloy. The disc specimens were machined such that their radii were in a plane parallel to that of the bar stock extrusion direction. Anisotropy effects arising from particulate alignment would most likely affect results in this regard, as discs were not machined in any other orientations relative to the bar stock extrusion direction. A burst of oscillations from a magneto-restrictive transducer at the remote end of the line drives the resonator and the return signals are detected by the same transducer. Measurements of resonance frequencies are carried out by displaying the signal returned from the resonator on an oscilloscope.

3.1.6 *Wear and tensile specimen preparation*

Specimen preparation for each of the tribological and tensile tests was carried out by cutting samples from extruded bar stock using a water fed abrasive cut-off wheel, followed by machining to the required dimensions. The specimens for abrasion and sliding wear tests were machined such that the wear face of each was made perpendicular to the direction of extrusion of the bar stock. Machining operations were carried out using standard carbide tip tooling.

3.2 Tensile Testing

The stress-strain behaviour of each composite and unreinforced alloy was determined by conducting uniaxial tensile tests to failure, on tensile specimens machined from each material. Each specimen was made according to ASTM B557 standards [97], using a flat section specimen geometry and a 30mm long gauge length (6mm x 4mm gauge length cross section). The tensile specimens were machined such that the gauge length was parallel to the extrusion direction of the bar stock. Gauge lengths of each specimen were mechanically polished to remove machining marks followed by an electropolishing procedure in an 80:20 methanol/nitric acid mixture at -17° C and 20V for 5-10 seconds. The electropolishing procedure was used to remove all traces of particulates which had fractured during mechanical polishing, as well as to obtain a finish in the matrix alloy suitable for microstructural observation. Testing was carried out at a strain rate of $2.5x10^{-4}$ s^{-1} on a *Zwick 1484 Universal Testing Machine* and scanning electron microscopy was employed to establish the post-fracture deformation characteristics and fracture mode for each specimen.

3.3 Abrasion Testing.

Dry abrasion testing was performed using a modified Rockwell belt sanding machine shown in fig.2 [98]. A continuous bonded abrasive belt is run horizontally at a constant velocity, against which a specimen is loaded perpendicularly on its cross-section face (10mm x 10mm). The specimen is made to traverse normal to the direction of the belt movement so that it always abrades against unworn particles. The total abrasion distance traversed by each of the composites and unreinforced alloys was about 20 metres, with mass losses being determined at specific intervals. Wear rates were calculated from the mass losses averaged over the total distance abraded by each specimen.

The conditions employed for testing are shown in Table II. The wear rate of each material was determined using four different grit sizes of alumina bonded abrasive belt. The average abrasive particle diameters and distribution densities were measured from scanning electron micrographs of each of the different grades of abrasive belt. The diameters were measured from a minimum of fifty particles on each micrograph and averaged. Worn surfaces of the composites and matrix alloys were also examined in the scanning electron microscope in order to establish their respective wear modes.

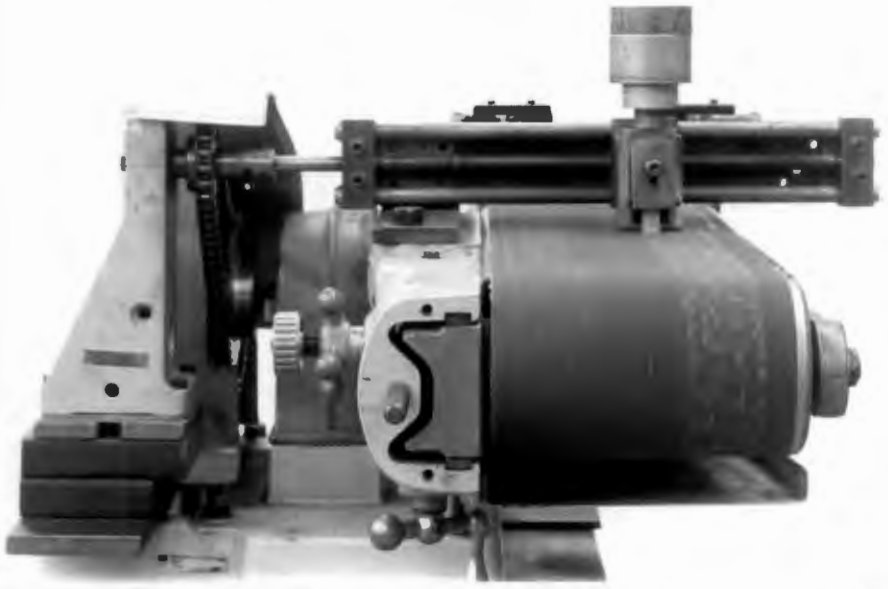

Fig.2: The abrasion test rig used for each abrasive wear experiment. The apparatus consists of a modified Rockwell belt sanding machine, where the wear specimen is made to traverse normal to the direction of the belt movement so that it always abrades against unworn particles. The specimen is clamped in a holder which is able to move freely in a vertical direction. Weights are placed above the specimen, providing a constant normal load.

Nominal Contact Pressure	0.1 MPa
Applied Load	10 N
Abrasive Type	Alumina
Abrasive Belt Speed	0.34 ms^{-1}
Abrasive Grit Mesh Nos.	220, 320, 400, 600

Table II: Conditions employed for abrasion testing of the composites and unreinforced alloys against four different grades of bonded abrasive belt.

3.4 Reciprocating Sliding Wear Tests

Reciprocating sliding wear tests were conducted with the composites and matrix alloys as sliders using a AISI431 stainless steel as the counterface material. Each counterface was heat treated to a hardness in the range 441-452 HV and surface ground to an average roughness of R_a = 0.3 μm. The rig used consists of a reciprocating base arrangement to which is attached the counterface specimen [99]. A photograph of the rig is shown in fig.3. The material to be tested is loaded against the counterface and distilled water used as a coolant and debris remover. Each of the composite and monolithic alloy sliders were machined to 10mm x 10mm x 25mm dimensions, with the 10mm x 10mm face being loaded against the counterface. All slider contact faces were

wet ground on 1200 grit silicon carbide paper prior to wear testing. The as-ground wear surfaces of the stainless steel counterfaces were 50mm long and 14mm wide. The distance traversed by the slider sample relative to the counterface, in one cycle of reciprocating motion, was 60mm.

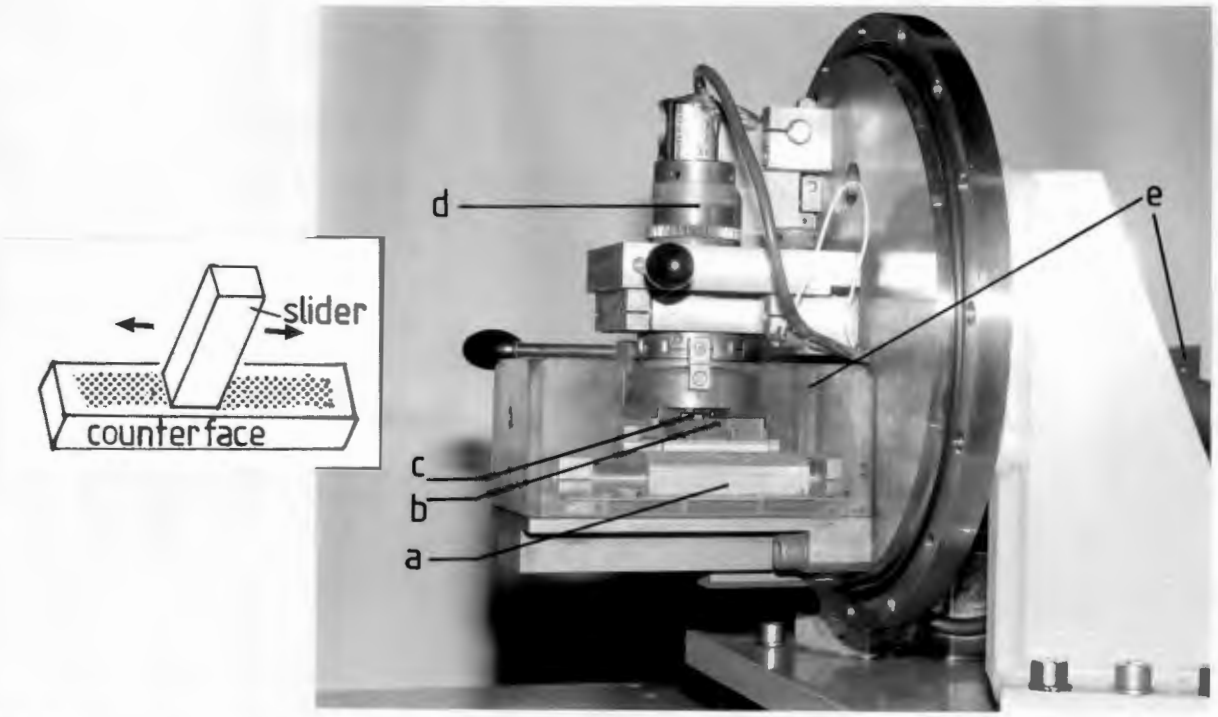

Fig.3: The reciprocating sliding wear test rig. The sliding specimen (c) is loaded against a stainless steel counterface (b) which is attached to a reciprocating base arrangement (a). The load on the wear specimen is adjusted using the spring/load-cell arrangement at (d). Water is fed into the system at (e); the outer environmental/drainage chamber has been removed to facilitate observation. The schematic shows the specimen/counterface contact geometry.

Wear tests were conducted using a counterface reciprocating rate of 31.5 cycles s^{-1} which corresponds to an average sliding speed of 1.9 ms^{-1}, and a maximum speed of 3 ms^{-1} during each cycle. A load of 20 N (0.2 MPa nominal pressure) was applied to each sliding specimen for the duration of each test, using a load cell arrangement as monitor. Mass loss/gain readings of both the sliding specimens and counterfaces were recorded at specific intervals of sliding distance. Typical sliding distance intervals used were after 10^5 cycles (6km). Total sliding distances were of the order of 10^6 cycles (60km) for the composite wear tests. Wear rates were then calculated from cumulative mass loss measurements averaged over sliding distance in the steady state wear regime. Scanning electron microscopy was employed to establish the wear mode for counterfaces and sliding specimens. Composite sliding specimens were sectioned perpendicularly and at a taper angle (5°), to their worn surfaces in order to reveal subsurface deformation. EDS X-ray mapping was used to determine the extent of material transfer between sliding specimen and counterface. In an effort to minimise the damage associated with conventional mechanical grinding and diamond polishing metallographic procedures, an

alternative approach was employed to examine the subsurface damage in sliding specimens. This involved sectioning the slider into two halves, using a diamond micro-saw, such that the cut was parallel to the sliding direction and normal to the wear face. Each half was then electropolished in an 80:20 methanol/nitric acid electrolyte so as to remove all traces of particulate damage and debris associated with the sectioning process. The two halves were then carefully bonded together again using a cyanoacrylate adhesive, followed by wear testing of the specimen. Inspection of the subsurface deformation was undertaken by separating the slider 'halves' by dissolving the adhesive away in acetone for several hours, followed by examination in the scanning electron microscope.

3.5 Solid Particle Erosion Tests

A conventional air blast type erosion rig [100] was used to erode coupon specimens of each composite and matrix alloy. A schematic diagram of the erosion testing rig is shown in fig.4. Erodent particles are fed via a vibratory hopper into an airstream at controlled pressure in which they are accelerated towards the target sample. Silicon carbide particles (120 grit, approx. 100μm in diameter) were used as the erodent. All tests were conducted using the same airstream pressure of 250 kPa which corresponded to an average particle velocity of 60 ms^{-1}. The particle velocity was determined using the double rotating disk method of Ruff and Ives [101].

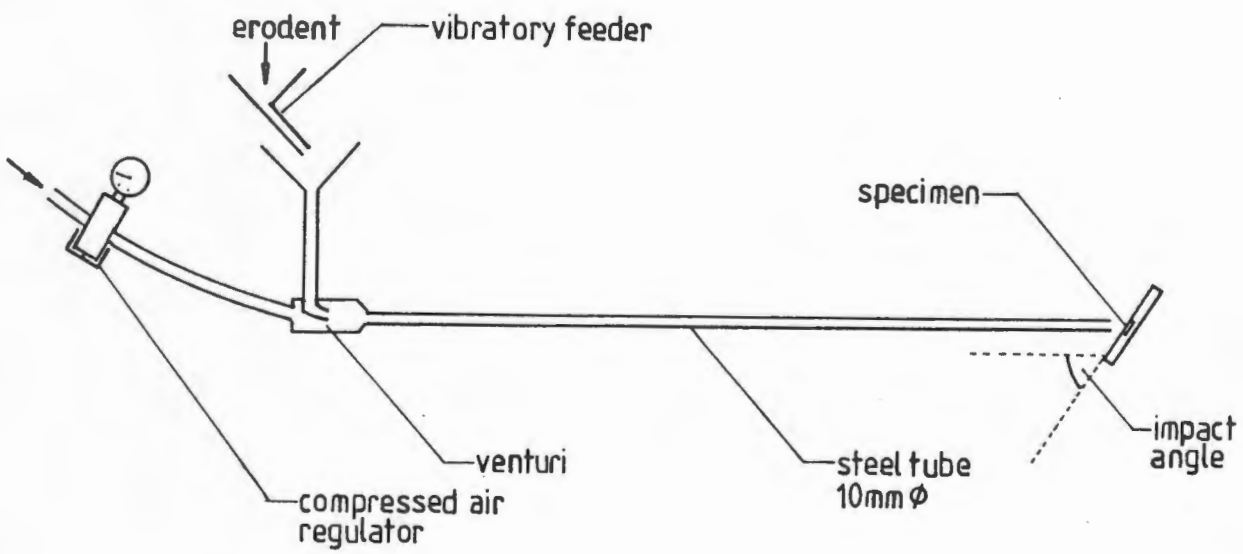

Fig.4: Schematic showing the air-blast type erosion rig used for solid particle erosion testing of each material.

Each specimen was eroded to steady state conditions with mass loss/gain measurements being made after impact by 5 grams of erodent in the incubation region, and 10 grams in the steady state regime. Erosion rates were calculated from the steady state regions on plots of cumulative mass loss as a function of total erodent mass. Erosion behaviour was determined for each specimen inclined at angles of 30° and 90° to the erodent stream. The modes of material removal for all the composites and unreinforced alloys were characterised using scanning electron microscopy. The extent of subsurface damage in each material was examined by taper sectioning of eroded sample surfaces.

3.6 Cavitation Erosion Testing

Coupon specimens of each of the composites and matrix alloys were polished to a 1μm surface finish and eroded in a vibratory cavitation erosion rig [102]. The cavitation apparatus consists of an ultrasonic drill, which generates high frequency oscillations in the 18.5 to 22 kHz range. A schematic diagram of the cavitation rig is shown in fig.5. The rig has been designed so that samples can be clamped beneath the drill tip followed by immersion in a bath containing the cavitating liquid. A separating distance between the drill tip and specimen surface of 0.35 mm was used throughout the testing routine and the vibratory amplitude of the drill tip was calibrated at between 75 μm and 100 μm.

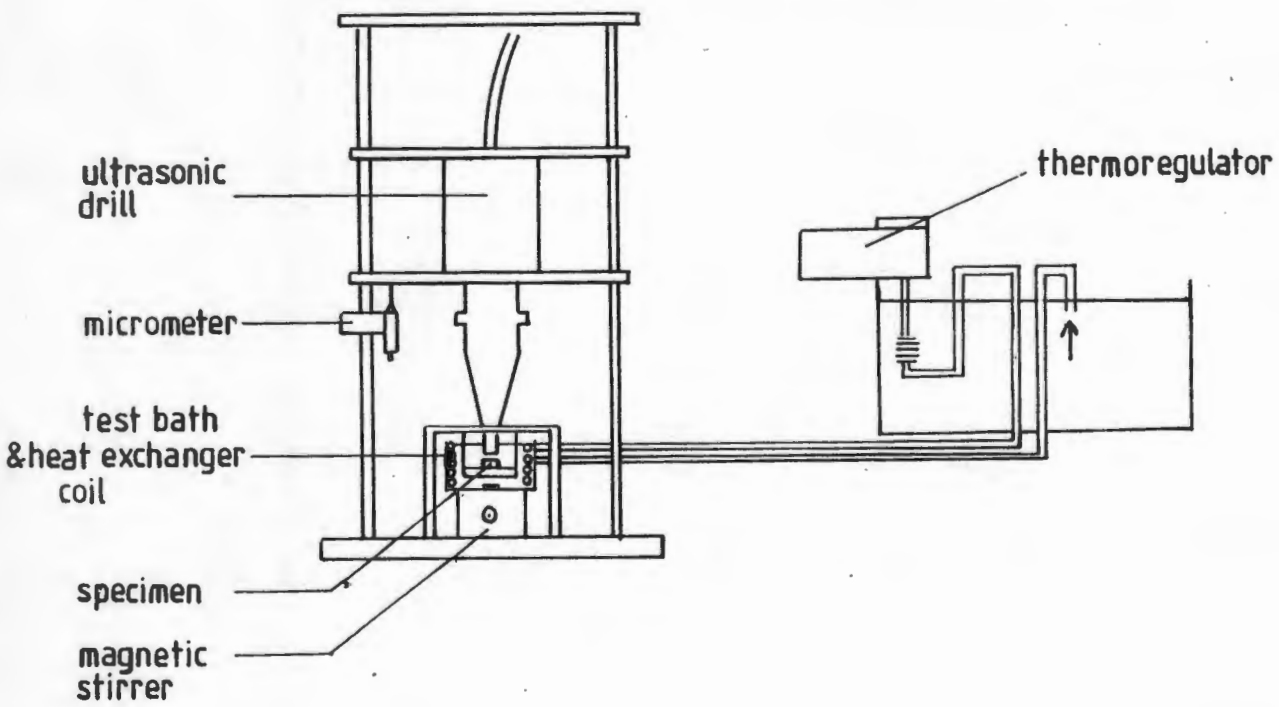

Fig.5: Schematic showing the vibratory cavitation erosion rig configuration. The apparatus consists of an ultrasonic drill (18.5-20 kHz) below which the specimens to be eroded are clamped and submerged in a bath of distilled water. - After Heathcock [102]

Distilled water was used as the cavitating liquid which was kept at a temperature of 25°C by a thermostat/cooling coil arrangement. Each specimen was eroded and weighed initially at time intervals of two minutes in order to establish their respective erosion incubation periods. Thereafter longer erosion time intervals were used in the steady state erosion region up to a total cumulative period of one hour. Cavitation erosion rates were determined from the steady state regions of cumulative mass loss and erosion time plots. The changes in surface topography of the eroded specimens were monitored using scanning electron microscopy. Subsurface damage in each composite was inspected through the use of taper sections of eroded surfaces.

3.7 Transmission electron microscopy

Attempts were made to characterise the subsurface dislocation structures associated with the various wear modes which have been investigated. Worn specimens were sectioned approximately 1mm below the wear surface using a diamond saw and aqueous cutting fluid. The as-worn surface of each specimen was protected from cutting debris, fluid and man-handling throughout the cutting and grinding procedures by coating it with proprietary lacquer (*Lacomit*). The sections were wet-ground on 800-1000 grit SiC paper to approximately 0.4mm thickness. Disc specimens, 3mm in diameter were then punched from the 0.4mm section, taking care to ensure that the direction of punching was from below the worn surface. The unworn side of each specimen was then mechanically ground on 1200 grit SiC paper, in order to obtain a disc thickness of approximately 250μm.

The discs were jet-polished on a Struers Tenupol 3 with an 80:20 methanol/nitric acid mixture using a potential of 15V. The polishing solution was cooled to around 0°C in an ice/ethanol mixture. While other researchers [28,32,33,40,103] have cooled their polishing solutions to between -10°C and -25°C when polishing aluminium matrix composites, it was decided to use a higher temperature of 0°C. This was done in order to minimise the possible re-arrangement of subsurface dislocation structures, which may arise as a result of the differential thermal contractions between the aluminium matrix and ceramic reinforcing particulates during cooling to temperatures of around -30°C. Likewise, cold-stage ion milling, a method used by many researchers to thin metal matrix composites [17,104-106], was not considered due to the likelihood of large temperature variations arising in the disc specimens during cooling, as well as the possibilty of ion beam damage occurring.

The preparation of wear microstructures for examination at different depths below, and parallel to the worn specimen surface, was undertaken by back-thinning of the disc

specimens. Polishing rates were determined from unworn composite and monolithic alloy specimens. Using these polishing rates, both sides of a TEM disc would be polished for a fixed period of time to the required depth below the worn surface. The jet-polished worn side of the disc was then protected from further thinning using lacquer (*Lacomit*). The specimen would then be back thinned until perforation, followed by removal of the lacquer by carefully suspending the foil in acetone for several minutes. In situations where the worn surface microstructure was to be examined (eg. wear transfer layers), the as-worn surface of the TEM disc was protected with lacquer, followed by back thinning to perforation and removal of the lacquer in acetone.

All foils were immediately cleaned following polishing procedures, by carefully dipping them into distilled water and then methanol. They were then stored under methanol and examined in the transmission microscope within 8-10 hours. Keeping the specimens any longer resulted in the electron transparent regions of aluminium becoming oxidised and unsuitable for examination. Microstructures were examined in a *JEOL 200CX* transmission electron microscope, operating at 200kV.

4.0 Results

4.1 Materials Characterisation

4.1.1 *Preliminary heat treatment results*

The age hardening characteristics of each reinforced and unreinforced 6061 aluminium alloy are displayed in fig.6. The monolithic alloy attains its peak hardness after some ten hours of artificial ageing, while the two alloys containing 20 vol.% alumina and 20 vol.% silicon carbide each attain peak hardness after eight hours. There appears to be little significant difference in ageing time to maximum hardness between the 15 vol.% and 10 vol.% alumina reinforced alloys in comparison to the behaviour of the monolithic alloy. These results are similar

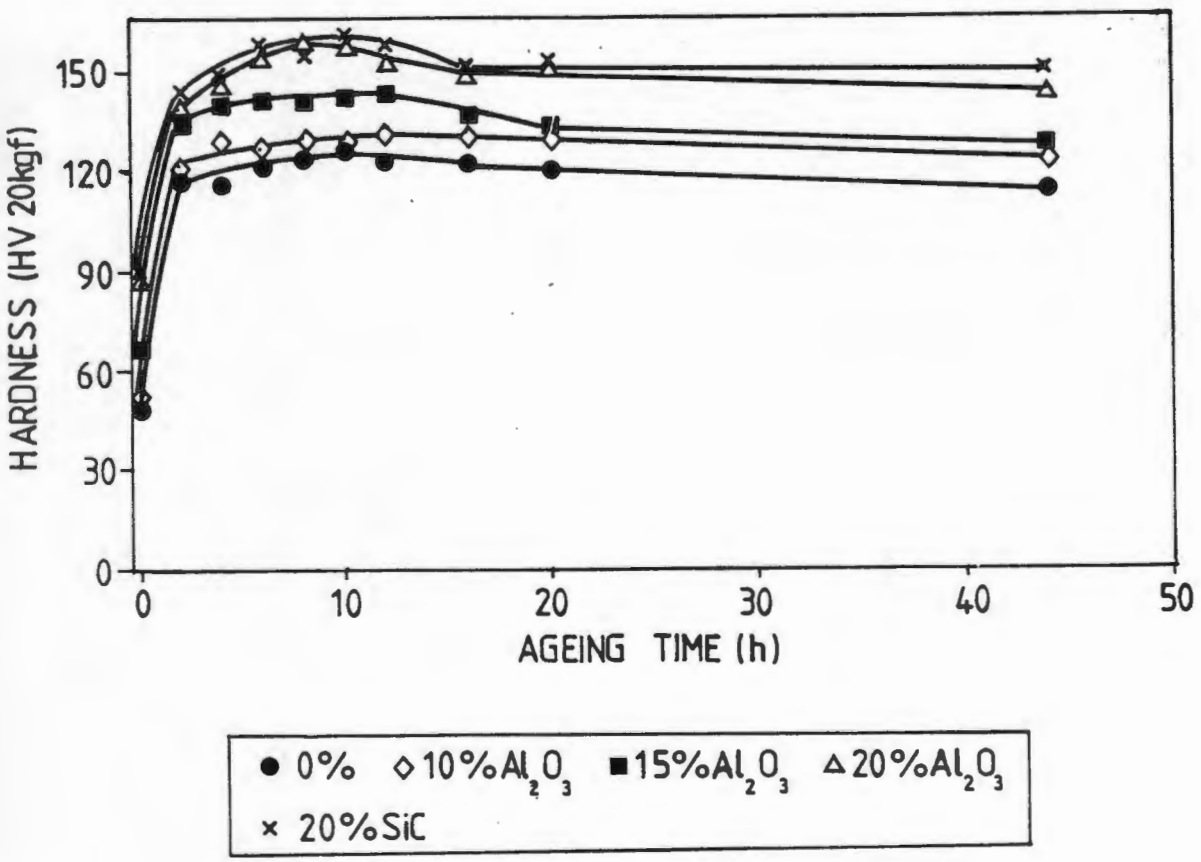

Fig.6: Age hardening characteristics of the reinforced and unreinforced 6061 matrix alloys. The heat treatment was carried out at an ageing temperature of 175°C being solution treated at 520°C, followed by quenching into water.

to those of Lloyd [36] who studied the deformation and fracture characteristics of silicon carbide reinforced 6061 alloys. Using the same heat treatment conditions as this investigation, he observed maximum tensile strengths in 10 vol.% and 20 vol.% reinforced alloys after eight hours ageing, which was close to the ten hours obtained for the monolithic matrix alloy.

The reinforced 2014 matrix composites also exhibited an accelerated ageing effect in comparison to the unreinforced 2014 matrix alloy, as is shown in fig.7. Peak hardness is attained after twelve hours of ageing in the unreinforced alloy, compared to eight hours for the 10 vol.% and 20 vol.% alumina reinforced composites. The 15 vol.% alloy represents a slight anomaly in that it takes some ten hours to attain peak hardness.

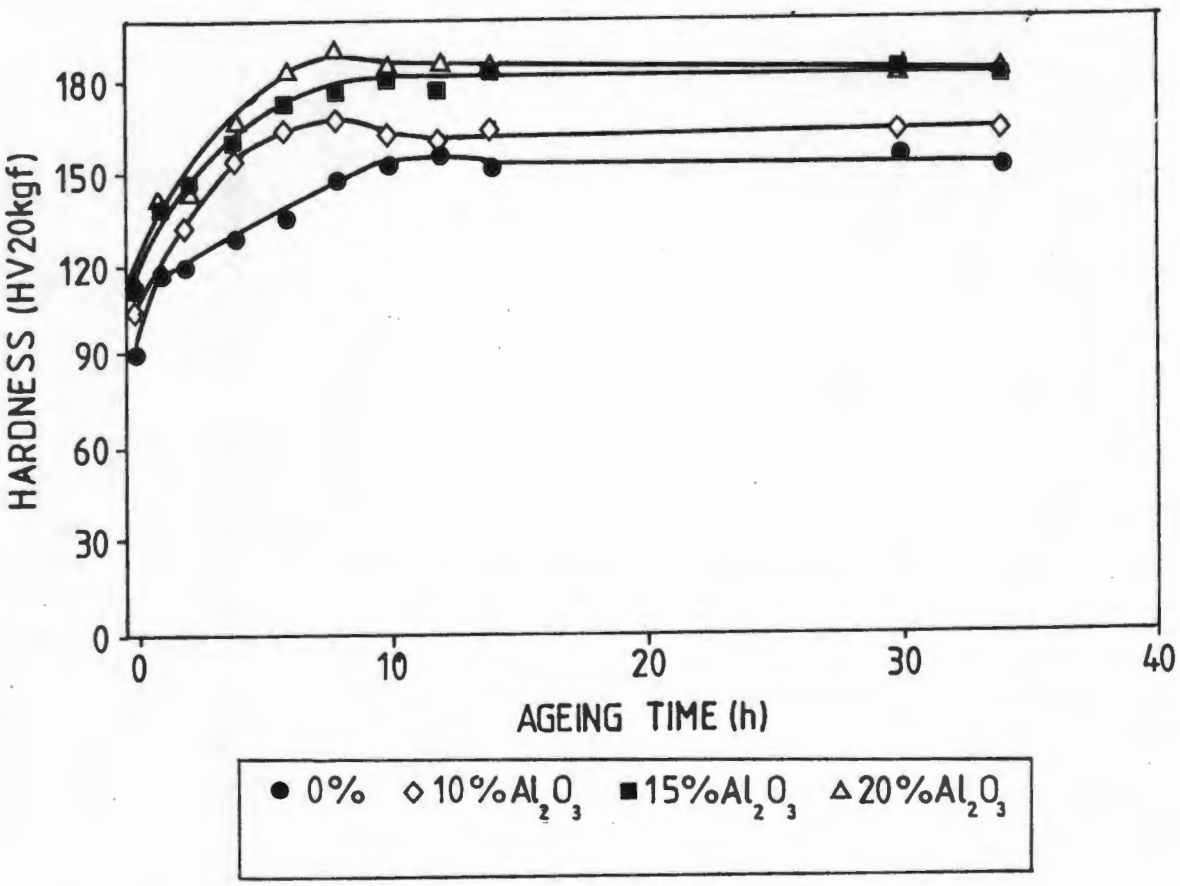

Fig.7: Age hardening characteristics of the reinforced and unreinforced 2014 matrix alloys. The heat treatment was carried out at an ageing temperature of 175°C after being solution treated at 495°C, followed by quenching into water.

4.1.2 *Heat treatment and matrix microhardness tests*

Bulk hardness values (HV_{20kg}) of each reinforced and unreinforced alloy in the peak aged condition are shown together with matrix microhardness measurements (HV_{15g}) in fig.8. The composites and monolithic alloys were solution heat treated and aged to peak bulk hardness, according to their respective optimum ageing times obtained from the preliminary heat treatment results. Both the 6061 and 2014 matrix alloys display an approximately linear increase in bulk hardness with increasing volume fractions of reinforcement.

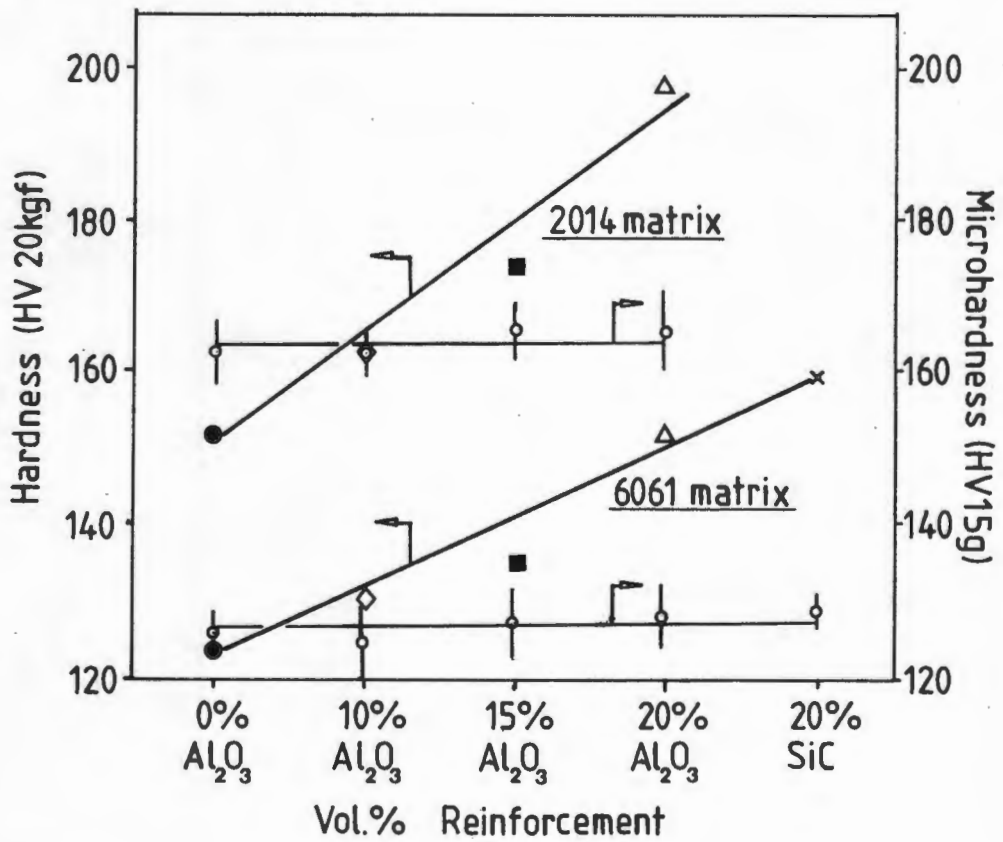

Fig.8: The plot shows bulk hardness values (HV_{20kg}) and matrix microhardness measurements (HV_{15g}) of composite and matrix alloy specimens which were solution treated and aged to their respective peak hardness values. The error bars associated with the microhardness readings, show the calculated standard deviations obtained from a minimum of twenty indents per sample.

The reinforced 2014 alloys are all harder in comparison to the 6061 matrix materials with the monolithic 2014 metal being only slightly softer than the 20 vol.% alumina reinforced 6061 composite. Of note is the silicon carbide reinforced 6061 alloy which displays a significantly greater hardness compared to that of the 20 vol.% alumina reinforced 6061 composite, despite having the same nominal volume fraction of reinforcement. The 2014 matrix composites also exhibit moderately greater increases in bulk hardness with added reinforcement in comparison to the 6061 materials with the same nominal particulate additions. This is borne out by comparing the slopes of the bulk hardness plots of the two alloy systems, where the 2014 matrix gradient is noticeably greater. The bulk hardness of each reinforced alloy is also affected by particulate size. Of all the alumina reinforced alloys, the two 20 vol.% alumina reinforced 6061 and 2014 alloys have the largest particulate size (Table III). Each of these composites show greater increments in hardness with reinforcement addition, when compared to their 10 vol.% and 15 vol.% reinforced counterparts which have smaller particulate sizes. Increased resistance to indentation arises as a result of additional plastic constraint in the matrix alloy. The matrix alloy is prevented from plastically deforming at the larger matrix-particulate interface regions in composites having bigger particulate sizes.

The microhardness results presented in fig.8 are an indication of the extent to which the matrix alloy of each composite and monolithic alloy has been artificially aged. Both the 6061 and 2014 monolithic alloys display microhardness values that fall within the same margin of error as those obtained for the composite matrices having the same alloy composition. Despite the experimental difficulties associated with taking microhardness measurements in the composites, there appears to be no significant evidence of any overageing effects. It can therefore be assumed that the inter-particulate matrix alloy of each composite has been aged to a hardness level that is similar to that of their respective unreinforced matrix alloys. Comparisons can now be made of the effect of particulate additions on the tensile and tribological behaviour of the two matrix alloys, which both have the same matrix properties as those of their various reinforced states.

4.1.3 *Monolithic alloy and Composite microstructures*

Optical micrographs of the 6061 and 2014 monolithic alloys are displayed in figs.9a and 9b respectively. The 6061 alloy has a grain size distribution which ranges

between 20 and 100μm in diameter. The higher magnification micrograph depicting the 2014 alloy, shows an extremely fine grain structure which ranges between 5 and 10μm in diameter.

Optical micrographs of each of the composites are shown in figs. 10a-10g. The distribution of reinforcing particulates in the alloys containing 15 vol.% and 20 vol.% reinforcement contents is generally uniform, with there being some evidence of clustering. The two 10 vol.% alumina reinforced alloys show significant particulate alignment in the extrusion direction. Average particulate sizes for each of the composites are listed in Table III together with their respective bulk hardness values.

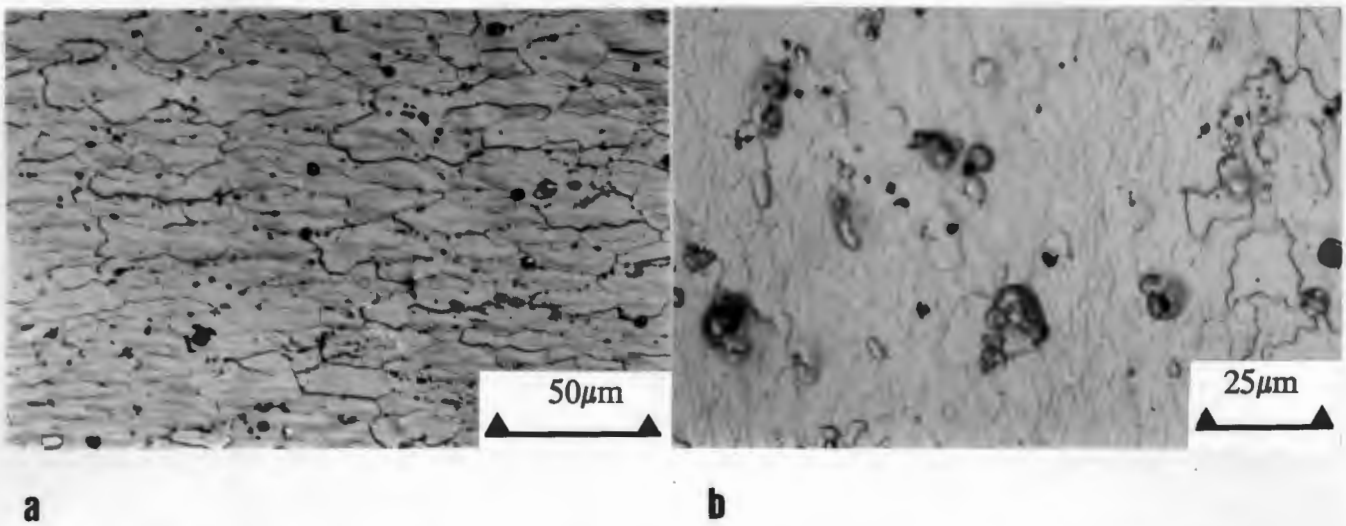

Figs.9a and 9b: Optical micrographs showing the microstructures of the 6061 and 2014 monolithic alloys respectively.

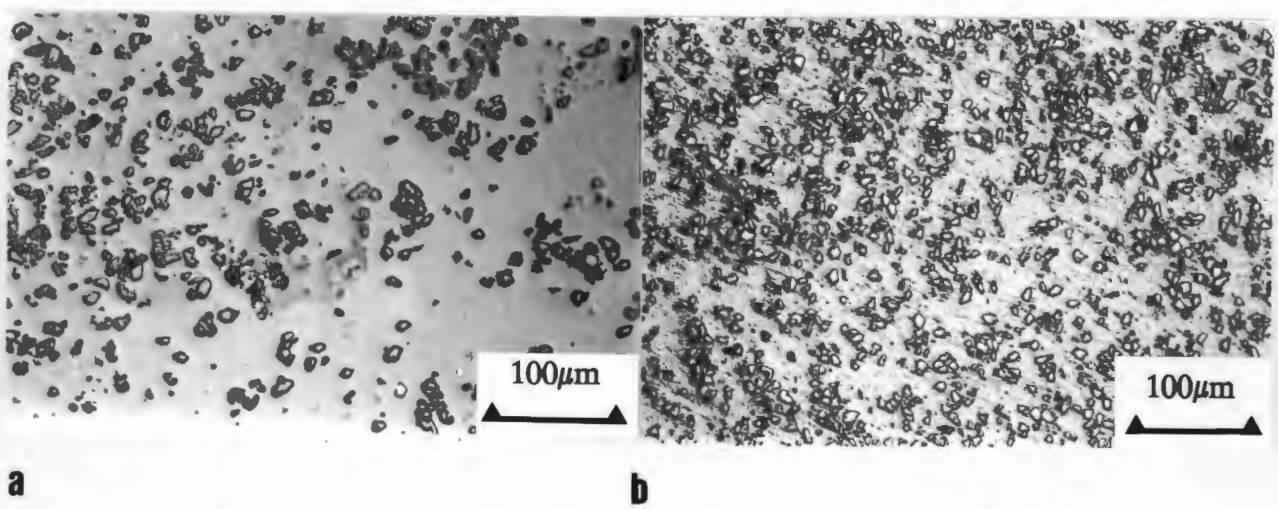

Figs.10a and 10b: Optical micrographs of the reinforced 6061 matrix alloy containing 10 and 15 vol.% Al_2O_3 respectively.

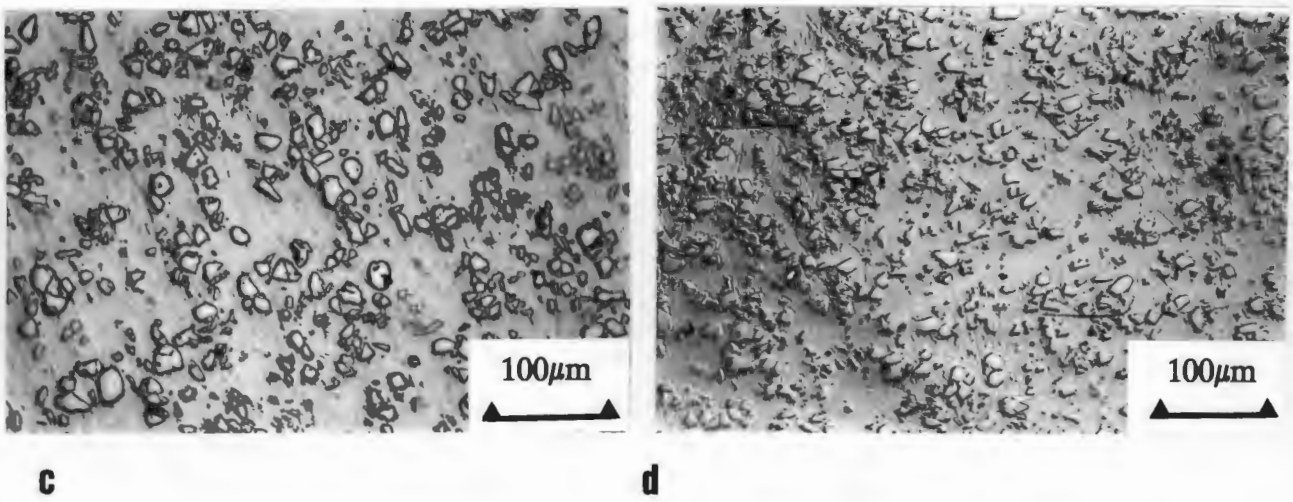

Figs.10c and 10d: Optical micrographs of the reinforced 6061 matrix alloy containing 20 vol.% Al_2O_3 and 20 vol.% SiC respectively.

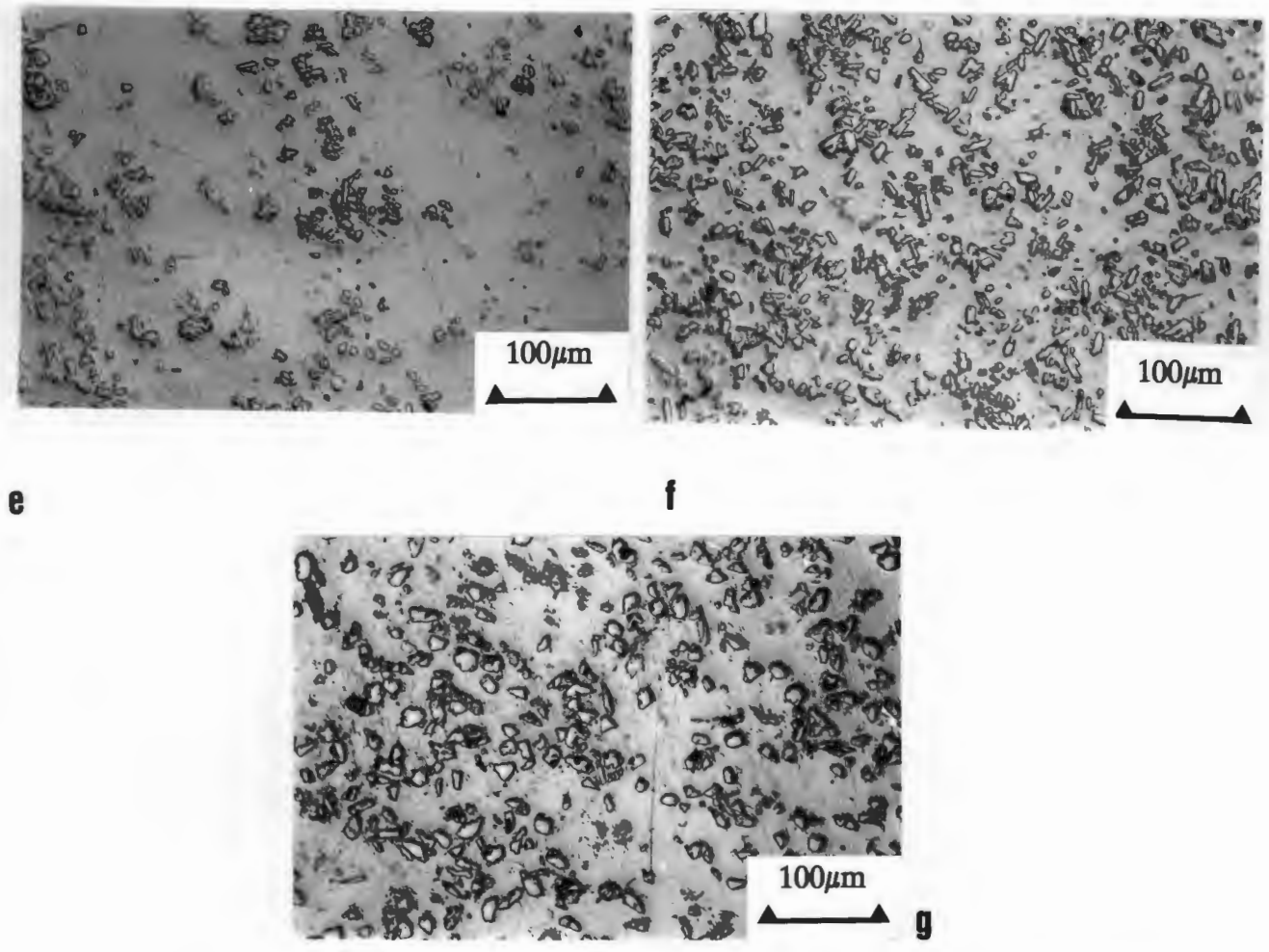

Figs.10e-g: Optical micrographs of the reinforced 2014 matrix alloy containing 10, 15 and 20 vol.% Al_2O_3 particulates respectively.

Alloy	Vol. % Reinforcement	Ave. Particulate Diameter (μm)	Hardness HV_{20kg}
6061	0	-	123.8
"	10% Al_2O_3	14.1	130.4
"	15% Al_2O_3	15.1	135.3
"	20% Al_2O_3	32.2	151.7
"	20% SiC	17.0	159.6
2014	0	-	151.4
"	10% Al_2O_3	11.4	162.5
"	15% Al_2O_3	13.6	173.8
"	20% Al_2O_3	27.2	196.9

Table III: Average diameters of reinforcing particulates in each composite and bulk hardness values of both reinforced and monolithic alloys.

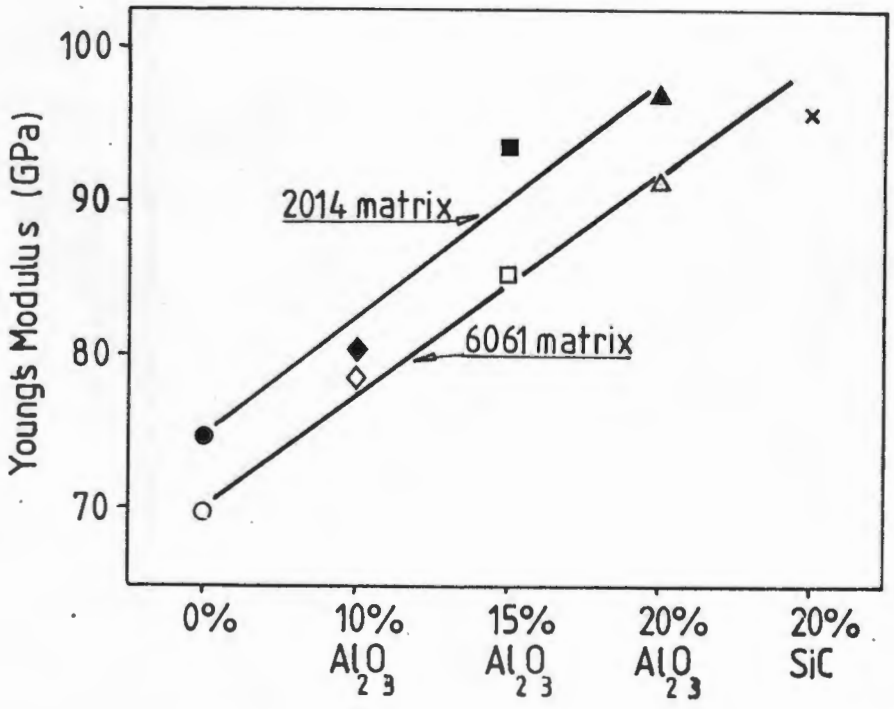

Fig.11: Plot of Young's modulus values of the composites and their respective monolithic alloys.

The largest particulates are found in the 20 vol.% alumina reinforced 6061 alloy (ave. 32.2 μm in diameter) and the 20 vol.% alumina reinforced 2014 alloy (ave. 27.2 μm in diameter), while those measured for the other alumina and silicon carbide reinforced composites were in the size range 11-17 μm. With the exception of the 15 vol.% alumina reinforced 2014 alloy, the majority of the particulates in each composite have an aspect ratio of approximately 1.0; the 15 vol.% 2014 composite has particulates that are more plate like in morphology, with a width to diameter ratio that is roughly 1:3.

4.1.4 *Young's modulus results*

A plot of the Young's modulus values of each composite and unreinforced alloy is shown in fig.11. The in-plane resonance frequencies which were measured for different disc resonance modes of each material, are displayed together with modulus calculations in Appendix I. Each matrix alloy exhibits an approximately linear increase in Young's modulus with higher volume fractions of alumina reinforcement, with the silicon carbide reinforced 6061 alloy having a proportionately greater stiffness compared to the alumina reinforced alloys.

4.2 Tensile Test Results

Tensile data together with Young's modulus and work to fracture ($E_{fracture}$) values pertaining to each composite and unreinforced alloy are summarised in Table IV. The work to fracture values were calculated from the area beneath each material's tensile curve shown in figs.12 and 13.

Alloy	Vol.%	E (GPa)	0.1% Proof (MPa)	UTS (MPa)	% Elong.	E_{frac} MJm^{-3}
6061	0	69.7	338	391	9.3	33.9
"	10% Al_2O_3	78.5	313	370	8.1	28.0
"	15% Al_2O_3	85.1	328	380	6.4	24.2
"	20% Al_2O_3	91.1	346	390	2.5	8.3
"	20% SiC	95.7	396	423	2.8	10.4
2014	0	74.4	436	508	10.5	49.9
"	10% Al_2O_3	80.4	419	481	4.6	19.5
"	15% Al_2O_3	93.6	426	465	1.6	5.4
"	20% Al_2O_3	96.9	431	455	0.9	2.2

Table IV: Summary of tensile data (UTS, 0.1% Proof stress and % Elongation) together with Young's modulus and work to fracture ($E_{fracture}$) values of each reinforced and unreinforced alloy.

The stress-strain curves obtained from uniaxial tensile tests of the 6061 matrix alloy and various composites are shown in fig.12. The 20 vol.% silicon carbide reinforced alloy displays the greatest ultimate tensile strength of 423 MPa with a failure strain of 2.8%. The 20 vol.% Al_2O_3 reinforced alloy is the strongest of the alumina reinforced 6061 matrix alloy composites at 390 MPa, having an elongation to failure of 2.5% which is considerably below those of the 10 vol.% (8.1% elong.) and 15 vol.% (6.4% elong.) alumina reinforced alloys. The ultimate tensile strength of the control alloy 6061 is similar to that of the 20 vol.% Al_2O_3 composite at 391 MPa and exceeds the strength of the 10 vol.% (370 MPa) and 15 vol.% Al_2O_3 (380 MPa) composites. Of note is the sharper yield characteristics obtained for the unreinforced alloy which work-hardens to some 8% strain whereas the yield behaviour of the composites appear less defined; indicating that microyielding is followed by a period of rapid work hardening.

The stress strain curves corresponding to the 2014 matrix alloy and various reinforced states are shown in fig.13. The elongation to failure of each composite is reduced by the addition of alumina reinforcement, with the 20 vol.% Al_2O_3 material failing at 0.9% strain. The tensile strength of each composite is also reduced with greater amounts of reinforcing particulates. The reinforced and unreinforced 2014 alloys are noticeably stronger than the 6061 matrix alloy and its composites. Note that the strains to failure of the 2014 composites are below those of their 6061 matrix alloy counterparts.

Examination of post-fractured tensile specimen gauge lengths for each of the composites revealed a number of characteristic features, the most prominent being that of reinforcing particulate fracture in the high strain region immediately below each fracture surface. Fractured particulates were also found in regions of the gauge length situated well away from the fracture surface, particularly for composites containing 15 vol.% and 20 vol.% reinforcement. However, the populations of these fractured particulates were considerably below those found in the immediate fracture surface region. The alloys containing 10 vol.% Al_2O_3 reinforcement exhibited very little particulate fracture elsewhere in the gauge length. The electron micrograph shown in fig.14 is the tensile specimen gauge length of the 20 vol.% Al_2O_3 2014 composite after it has been tested to tensile failure, the gauge length having been electropolished prior to tensile straining. An area approximately 1 mm below the fracture surface is displayed where a large

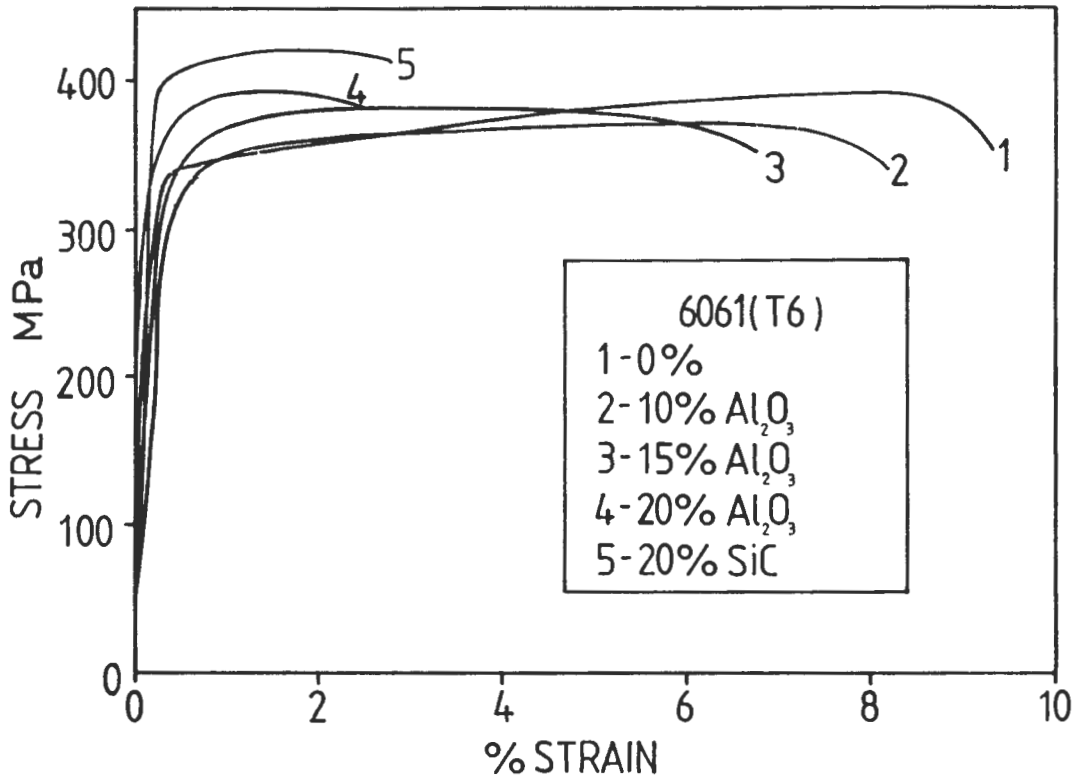

Fig.12: Tensile stress-strain curves of the reinforced and unreinforced 6061 aluminium matrix alloys.

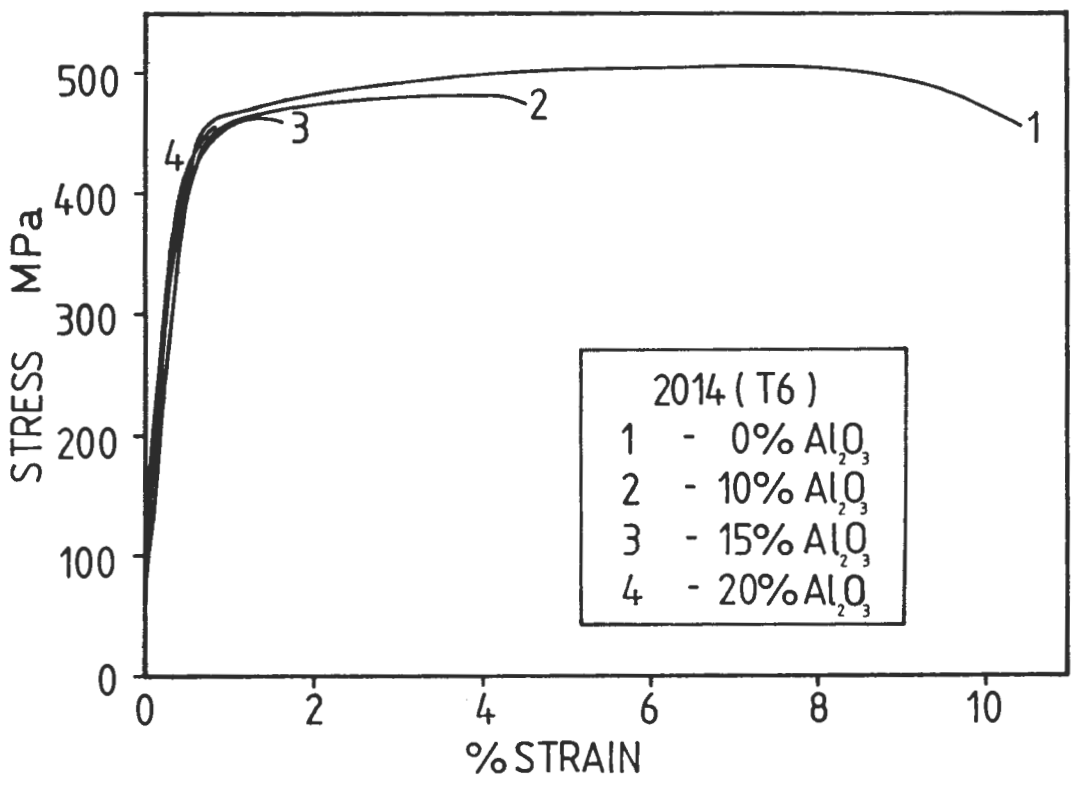

Fig.13: Tensile stress-strain curves of the reinforced and unreinforced 2014 aluminium matrix alloys.

proportion of particulates have fractured in an orientation perpendicular to the tensile direction. There is extensive evidence of void nucleation occurring in the matrix alloy especially adjacent to particulate interfaces. The bottom area of the micrograph shows crack development localised around a cluster of particulates. This is a common feature found in gauge lengths of each composite, particularly those containing 10 vol.% Al_2O_3 reinforcement, where inhomogeneous distribution of particulates was prevalent.

The tensile specimen gauge length of the lower strength 6061 alloy, reinforced with 15 vol.% Al_2O_3 particulates is shown in the electron micrograph in fig.15. The specimen has been tensile tested to failure and the area shown is a region of particulate damage just below the fracture surface, where a large amount of localised slip is associated with the formation of a cavity in the matrix alloy in the immediate vicinity of the cracked particulates. All the composites containing 15 vol.% and 20 vol.% reinforcement, showed evidence of intense shear in regions of interparticulate matrix alloy which were associated with localised deformation and cavity formation at cracked particulates and their interfaces.

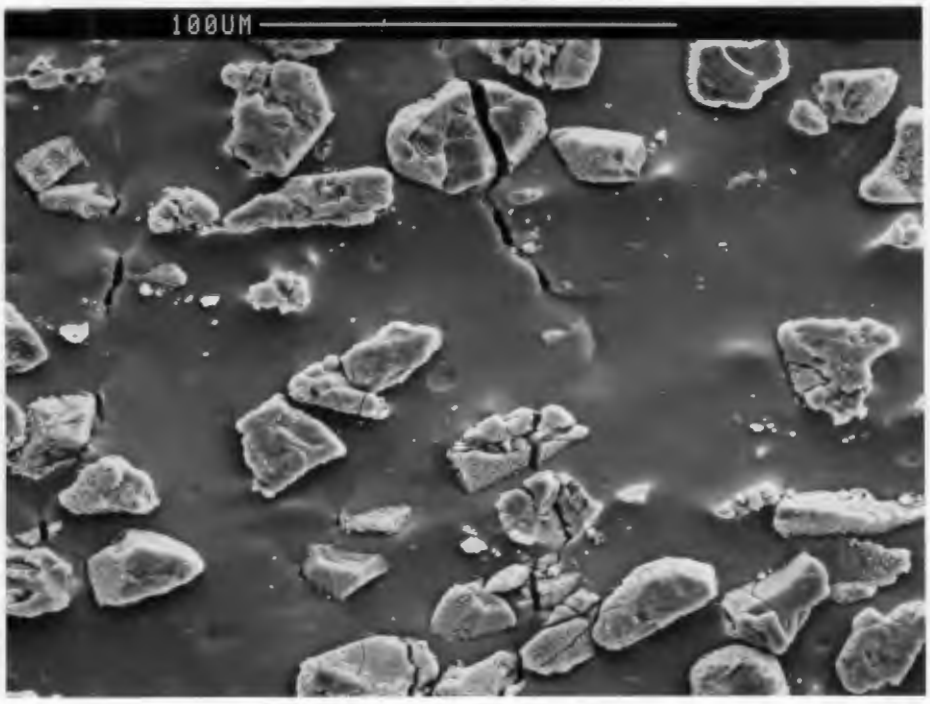

Fig.14: Electron micrograph of the 20 vol.% Al_2O_3 reinforced 2014 alloy gauge length after tensile failure. The area shown is approximately 1 mm below the specimen fracture surface. Arrows indicate tensile axis.

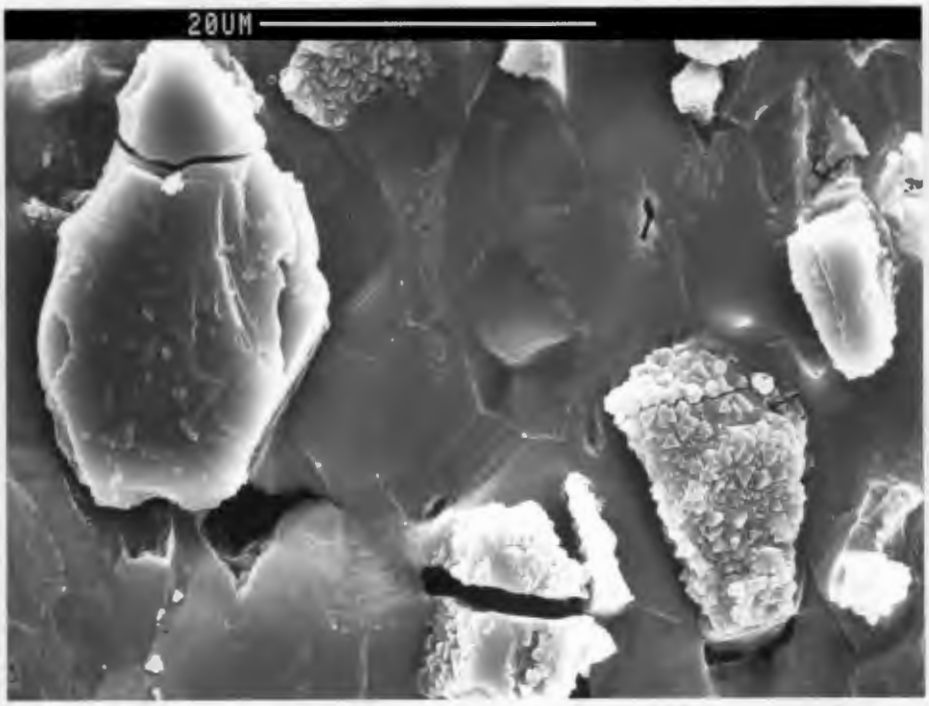

Fig.15: Electron micrograph of the 15 vol.% Al_2O_3 reinforced 6061 alloy gauge length after tensile failure. The area shown is approximately 0.5 mm below the specimen fracture surface where particulate cracking and cavity formation associated with localised tearing of the matrix alloy is evident. Note the presence of $MgAl_2O_3$ spinel crystals on particulate surfaces - it is possible that these act as additional stress raisers and crack initiators on alumina particulates. Arrows indicate tensile axis.

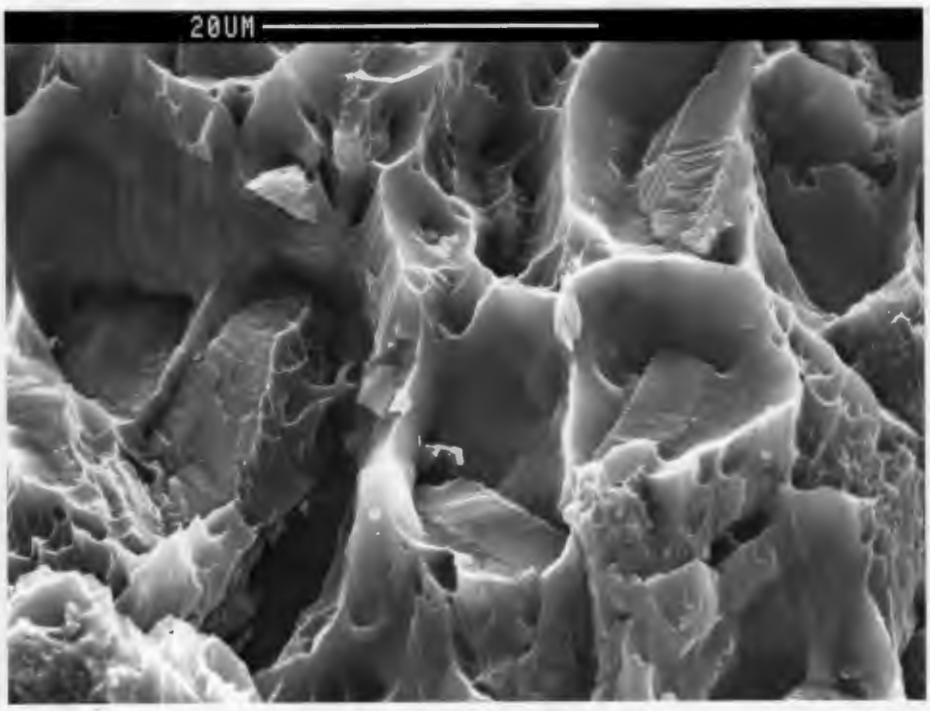

Fig.16: Electron micrograph showing the tensile overload fracture surface of the 6061 alloy reinforced with 15 vol.% Al_2O_3 particulates. Particulates have fractured in the plane normal to the tensile direction, forming regions of intense shear and cavities of torn matrix alloy. Isolated patches of small dimples are also visible on the fracture surface.

An electron micrograph of the fracture surface of the 6061 alloy reinforced with 15 vol.% Al_2O_3 is displayed in fig.14. Several fractured reinforcing particulates are observed, each partially or completely surrounded by a ridge of plastically deformed matrix alloy (described as "tear ridges" by Davidson [39]) with isolated patches of small dimples (2-3 μm) in the surrounding matrix. There is evidence for intense shear and delamination of matrix alloy in regions adjacent to particulate interfaces. Features similar to these were found on the fracture surfaces of all the composites, with the reinforced 2014 alloys displaying significantly less ductility associated with tear ridge formation and larger populations of very fine dimples (0.5 - 1.0μm). A typical example of fracture surface morphology of the less ductile 20 vol.% Al_2O_3 reinforced 2014 alloy is shown in fig.17. Particulates have undergone extensive fracture accompanied by intense shear of the matrix alloy adjacent to the interfaces. The micrograph in fig.18 shows similar features on the fracture surface of the SiC reinforced 6061 alloy. This composite has a higher level of ductility associated with the heavily sheared regions surrounding fractured particulates, compared to the 2014 composite in fig.17.

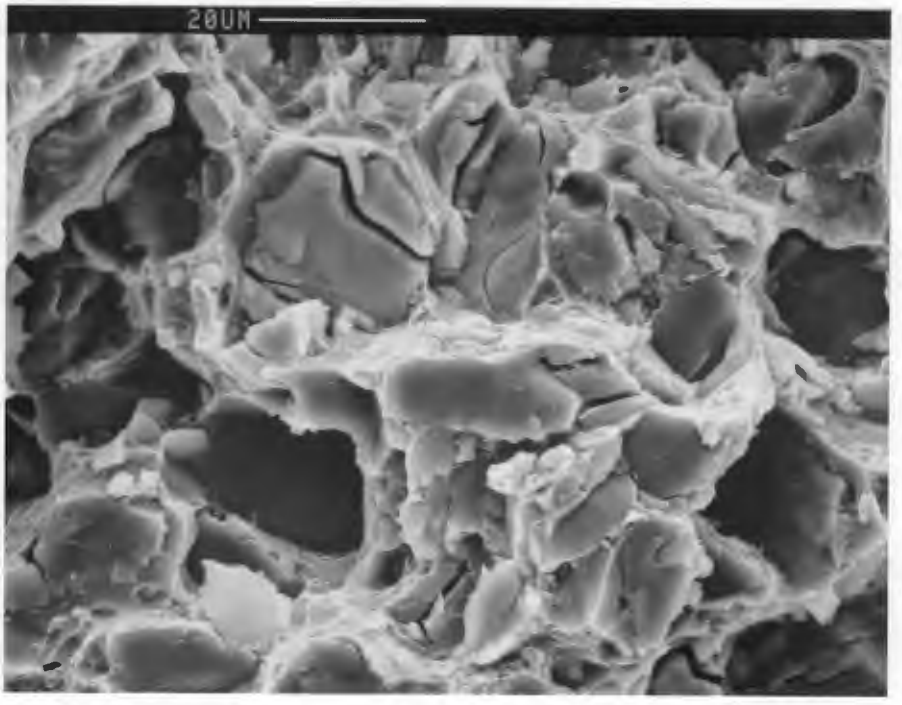

Fig.17: Electron micrograph showing tensile overload fracture surface of the 2014 matrix alloy reinforced with 20 vol.% Al_2O_3 particulates.

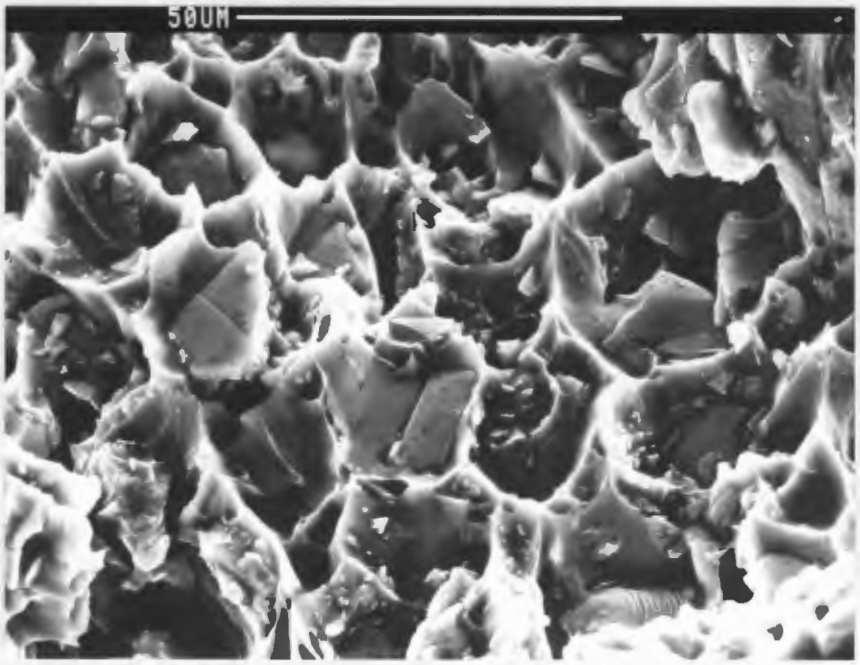

Fig.18: Electron micrograph showing the tensile overload fracture surface of the 6061 alloy reinforced with 20 vol.% SiC.

4.3 Abrasive Wear Results

The surface morphologies of the coarse grade (220 grit) and the fine grade (600 grit) bonded alumina abrasive belt used in this investigation are shown in figs 19a and 19b respectively. These two grades of abrasive show differences in both abrasive particle size and distribution density; the details of which are listed in Table V, along with those of the 320 grit and 400 grit abrasive belts which were also used.

Abrasive Grit Mesh no.	220	320	400	600
Abrasive Grit Diameter (μm)	56	44	34	16
No. Abrasive Particles/mm^2	123	218	377	1502

Table V: The average abrasive grit diameters (nearest μm) and distribution densities measured for each grade of abrasive paper.

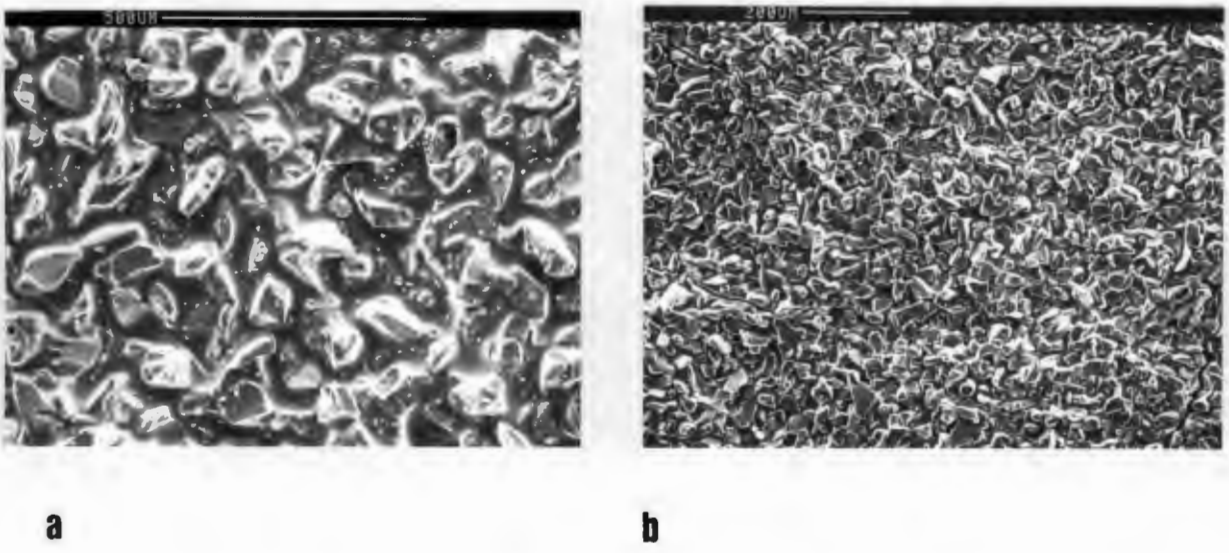

a b

Fig.19a and 19b: Surface morphologies of the coarse grade (220 grit) and fine grade (600 grit) bonded alumina abrasive belts respectively.

The abrasive wear rates for each of the 6061 and 2014 matrix alloys and their composites are shown in fig.20 and fig.21 respectively. Overall, the composites show distinct improvements in abrasion resistance compared to the unreinforced alloys. This is particularly the case when they are worn against the finer grit sized abrasives. The 6061 matrix alloy displays the largest wear loss during abrasion against all sizes of abrasive grit. In general, the 6061 matrix composites show greater wear rates than their 2014 matrix alloy counterparts, with the exception of the SiC reinforced 6061 alloy which is the most abrasion resistant of all the composites. It is interesting to note that the 20 vol.% SiC composite, with a hardness of 159.6 HV, which is below that of all the 2014 matrix alloy composites, is most abrasion resistant. In addition, of all the alumina reinforced alloys, the 6061 alloy reinforced with 20 vol.% Al_2O_3 has an abrasion resistance that is only exceeded by that of the 20 vol.% Al_2O_3 reinforced 2014 alloy. This is in spite of the fact that the 6061 matrix composite has a hardness of 151.7 HV, which well below that of all the other 2014 matrix alloy composites.

There is a distinct improvement of wear resistance of reinforced alloys, compared to those of their respective matrix alloys, especially when they are subjected to low stress wear conditions associated with the use of finer abrasive grit sizes. This pattern is more appropriately displayed in fig. 22 and fig.23, which show values of composite abrasion resistance calculated relative to those of the 6061

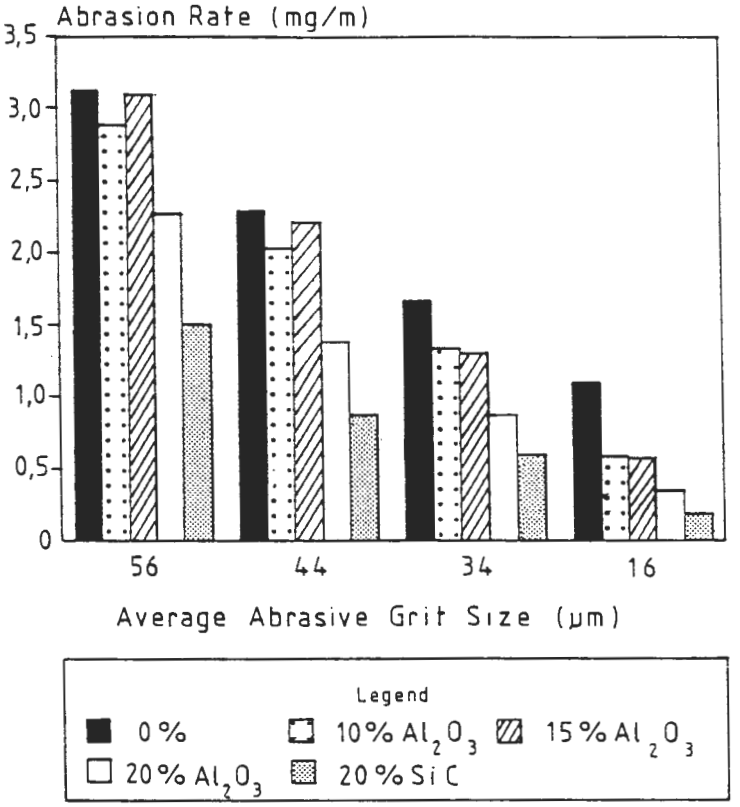

Fig.20: Abrasive wear rates of the 6061 matrix alloy and respective composites, determined as a function of abrasive grit size (alumina).

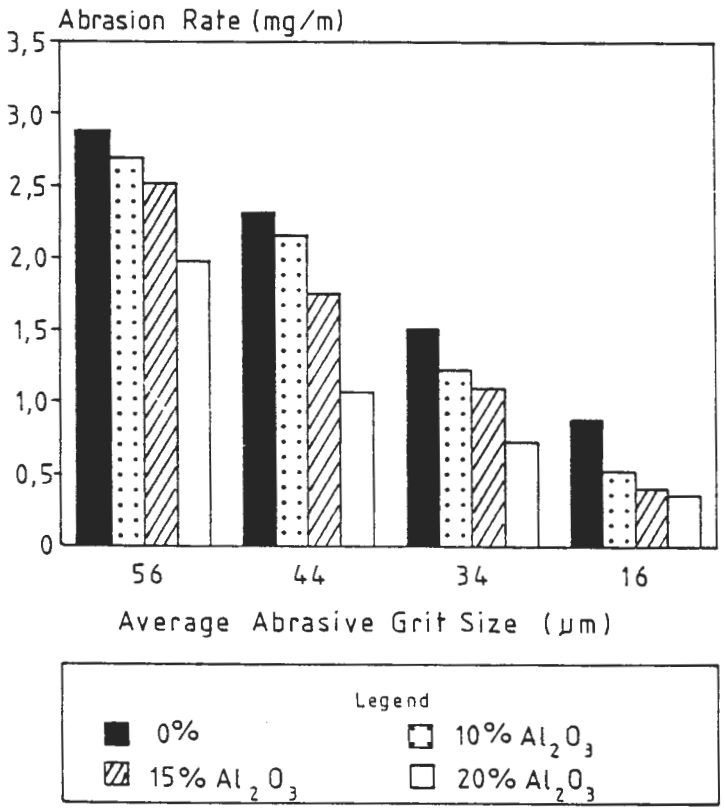

Fig.21: Abrasive wear rates of the 2014 matrix alloy and respective composites, determined as a function of abrasive grit size (alumina).

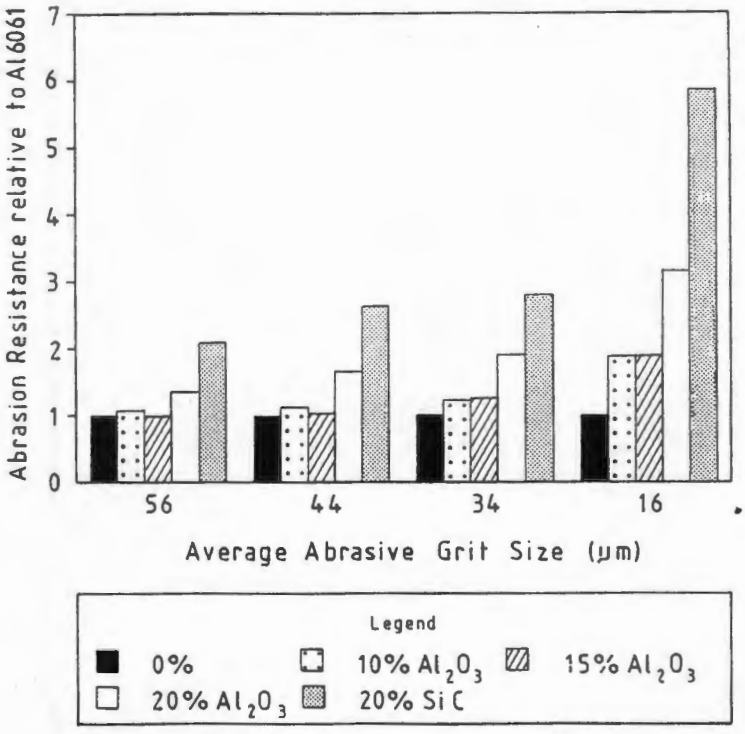

Fig.22: Abrasive wear resistances of the reinforced 6061 alloys, determined relative to the unreinforced matrix alloy and as a function of abrasive grit size (alumina).

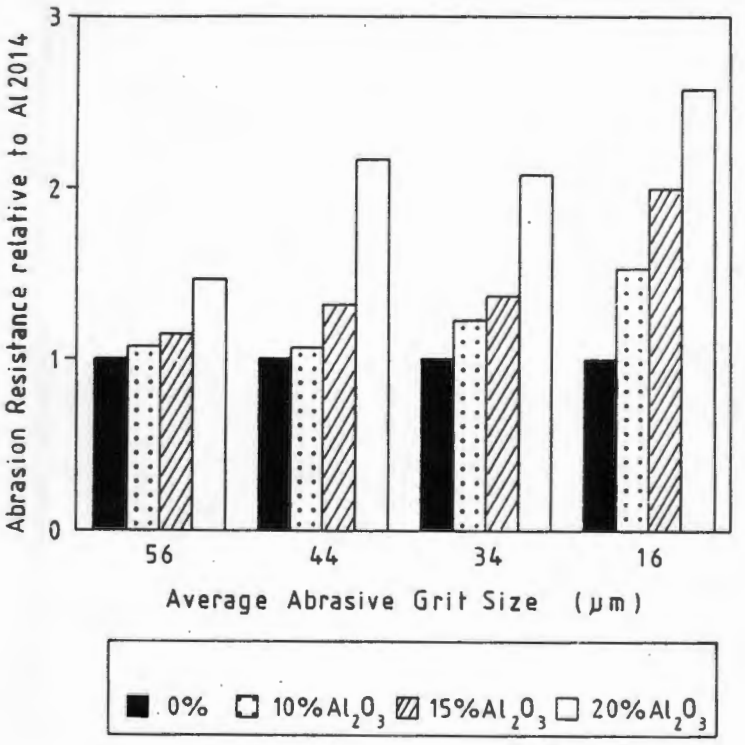

Fig.23: Abrasive wear resistances of the reinforced 2014 alloys, determined relative to the unreinforced matrix alloy and as a function of abrasive grit size.

and 2014 matrix alloys respectively, for each abrasive grit size. The SiC reinforced 6061 alloy exhibits the greatest increase in relative abrasion resistance, when compared to the behaviour of the other composites during abrasion against finer abrasive grit sizes. An abrasion resistance 5.7 times that of the 6061 matrix alloy is obtained when the SiC reinforced alloy is worn against the finest abrasive grit size. In contrast, the alumina reinforced composites of both matrix alloys display significantly lower relative abrasion resistances to those found for the SiC composite.

Composites containing higher volume fractions of reinforcement show proportionately greater improvements in relative abrasion resistance when subjected to low stress wear against finer abrasives. This tendency is evident in the behaviour of both the 2014 and 6061 matrix composites. The wear resistance of each composite, with the exception of the SiC reinforced 6061 alloy, approaches those of their respective matrix alloys upon being abraded by the coarsest abrasive grit.

The scanning electron micrographs of figs.24a and 24b show typical representations of the plastic cutting wear mode found in the unreinforced matrix alloys. The two micrographs display the 6061 alloy after abrasion by the largest and smallest abrasive grits respectively, with the only difference being in the depth and width of wear grooves on each surface. Abrasion by the coarse alumina abrasive has resulted in the formation of large wear grooves which are approximately 30 to 40μm wide on the surface of the monolithic alloy. In comparison, the groove widths and depths on the alloy surface after abrasion by the finest grit are significantly smaller, averaging between 5 and 10μm wide. Electron micrographs of abraded surfaces of the 6061 alloy reinforced with 20 vol.% SiC are shown in figs.25a and 25b. The composite surface after being subjected to high stress abrasion by the coarsest abrasive grit is shown in fig.25a, where extensive chipping of the matrix alloy and particulate fracture is evident. Wear grooves on the worn surface are significantly deeper compared to the same composite worn under low stress conditions using the finest abrasive grit, shown in fig.25b. The worn surface exhibits little particulate damage and the wear mode is characteristically attritive in nature. Similar transitions in wear mode were noted for the 15 vol.% and 20 vol.% alumina reinforced composites of both matrix alloys but to a lesser extent for the 10 vol.% alumina reinforced materials, where the wear mode was predominantly plastic cutting, with some particulate fracture and

chip formation at clustered regions of reinforcement.

A scanning electron micrograph of the abraded surface of the 15 vol.% Al_2O_3 reinforced 2014 alloy reinforced composites is shown in fig.26a. The composite has been abraded with the coarsest abrasive grit and the morphology of the reinforcing particulates is revealed by removing the surrounding plastically deformed matrix alloy by electropolishing for 1-2 seconds in a methanol/nitric acid mixture. Extensive fracture and crumbling of the alumina reinforcement is evident indicating that the stress imparted to the composite surface during abrasion, is high enough to damage the reinforcing particulates. However, the nature and extent of particulate damage is markedly decreased upon abrasion by the finest grit abrasive, as shown in fig.26b for the same composite as fig.26a. Particulate damage is minimal showing the upper surface of each particulate having been removed by a polishing mechanism. This abrasion mode was found to be characteristic in each composite, especially in those containing larger volume fractions of reinforcement. Similar particulate damage characteristics were found in the SiC reinforced 6061 alloy and the other alumina reinforced composites when abraded with the finer grit abrasive belts.

a b

Figs.24a and 24b: Electron micrographs of the 6061 matrix alloy after abrasion by the coarse grade (220 grit - 56 μm) and fine grade (600 grit - 16 μm), abrasive papers respectively.

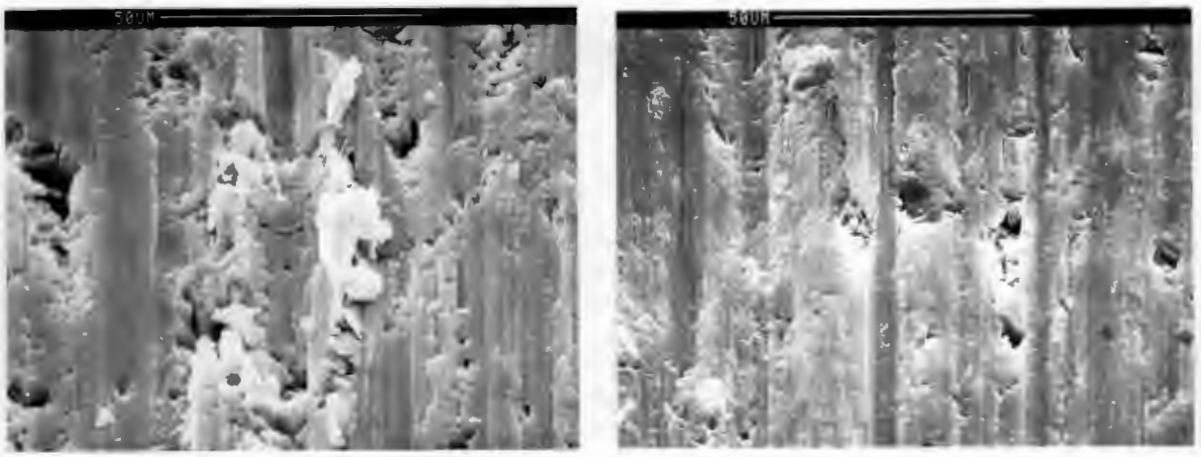

Figs.25a and 25b: Electron micrographs of the 20 vol.% SiC reinforced 6061 alloy after abrasion by the coarse grade (220 grit - 56 μm) and fine grade (600 grit - 16 μm), alumina abrasive papers respectively. Note the larger groove depths associated with abrasion against the coarse abrasive. The reinforcing particulates are approximately 10μm apart which is similar to the width of the wear grooves.

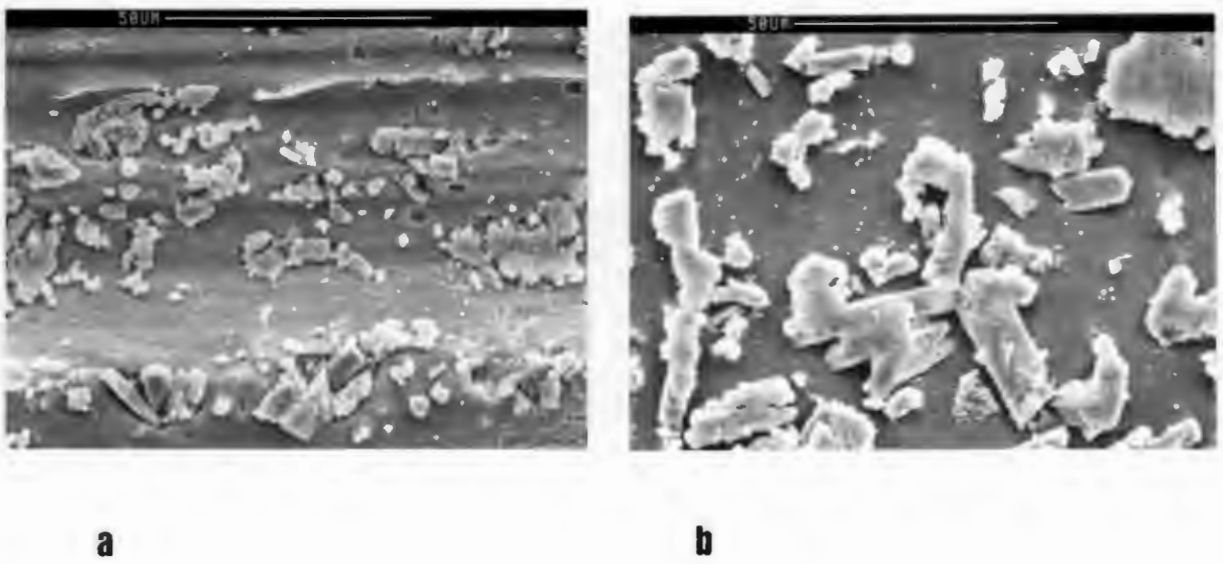

Fig.26a and 26b: Subsurface damage in the 15 vol.% Al_2O_3 reinforced 2014 alloy after abrasion by the coarsest (56 μm) and finest (16 μm) abrasive grits respectively. The worn surfaces were electropolished for 1-2 seconds to reveal particulate damage. Note the extensive fragmentation in the case of the abrasion with the coarse grit.

4.3.1 *Abrasion resistance against a silicon carbide abrasive.*

The effect of using an abrasive that is harder than alumina, such as silicon carbide, is demonstrated by the results displayed in the bar chart in fig.27. Each composite was worn against a 220 grit silicon carbide abrasive belt, using the same load and speed conditions that were outlined in Table II. The wear resistances of each material, relative to their respective unreinforced matrix alloys, are compared for abrasion against 220 grit alumina and silicon carbide abrasives. All the composites show a distinct decrease in abrasion resistance relative to their matrix alloys, when worn against the harder abrasive. The alumina reinforced alloys deteriorate in abrasion resistance to levels that are similar or below those of their respective matrix alloys, whereas the silicon carbide reinforced alloy shows a moderate reduction in relative wear resistance from 2.08 to 1.47 when worn against the silicon carbide.

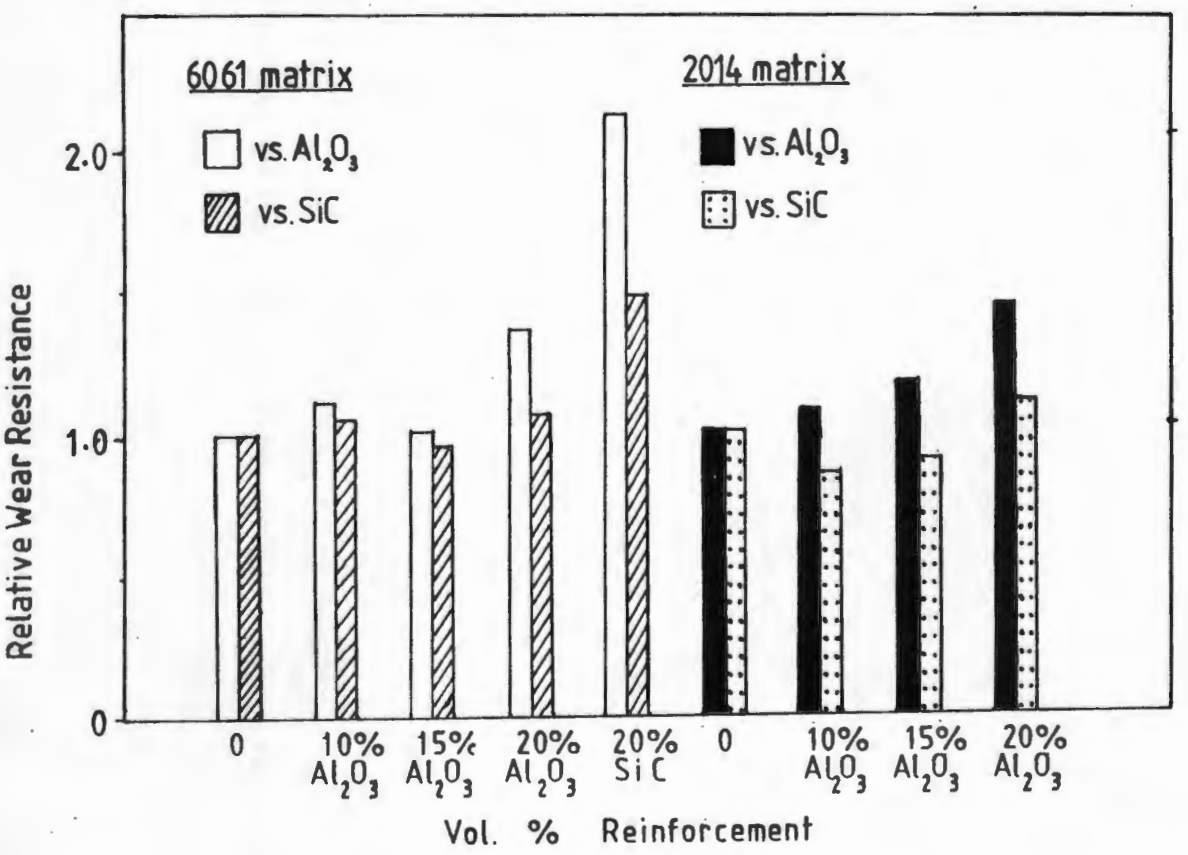

Fig.27: Bar chart showing the wear resistances of each of the reinforced alloys calculated relative to their respective matrix alloys. The relative wear resistances shown, are for abrasion against alumina and silicon carbide abrasive belts (220 grit - 56μm grit size).

4.4 Reciprocating Sliding Wear Results

The reciprocating sliding wear rates obtained for each of the 6061 and 2014 matrix alloy composites, the unreinforced alloys and the stainless steel counterfaces are represented in figs. 28 and 29. These wear rates were calculated from steady state regimes of material loss, over a minimum sliding distance of 24km, except for the unreinforced alloys where a minimum sliding distance of 3km was used. Each composite displayed an initial run-in period during which the wear sample achieved full geometrical contact with the steel counterface. The run-in period was almost immediate for the low volume fraction composites, whereas that for the higher volume fractions of reinforcement took up to 30km (eg. 6061 alloy reinforced with 20 vol.% SiC).

Very large improvements in sliding wear resistance are obtained when the aluminium alloys are reinforced with ceramic particulates. Wear resistances of the composites are improved by factors of up to three orders of magnitude in comparison to the monolithic alloys. A characteristic feature of the wear behaviour of all the reinforced alloys tested is the loss of material from both counterface and composite sliding sample. The unreinforced aluminium alloys show wear losses that exceed those of the composites by almost three orders of magnitude with no removal of counterface material occurring. These monolithic aluminium sliding samples had steady state wear rates of 272 $mgkm^{-1}$ and 28 $mgkm^{-1}$ for the 6061 and 2014 matrix alloys respectively. With the addition of 10 vol.% Al_2O_3 reinforcement to the 6061 and 2014 matrix alloys, the composite sliding samples showed wear rates of 0.78 $mgkm^{-1}$ and 0.15 $mgkm^{-1}$ and had counterface wear rates of 3.67 $mgkm^{-1}$ and 1.13 $mgkm^{-1}$ respectively.

The 6061 matrix composites and associated counterfaces display a trend towards lower wear rates with increasing volume fraction of reinforcement. The wear rate of the 20 vol.% SiC reinforced material is approximately half that of the 20 vol.% Al_2O_3 reinforced 6061 alloy and displays a markedly lower counterface wear rate. When the wear behaviour of the 6061 composites is compared to those of the 2014 composites shown in fig. 29, the 2014 composites reinforced with 10 vol.% Al_2O_3 and 15 vol.% Al_2O_3 particulates, exhibit lower slider and counterface material removal rates with the exception of the 6061 alloy reinforced with 20 vol.% SiC; this material has the lowest counterface wear rate of all the composites.

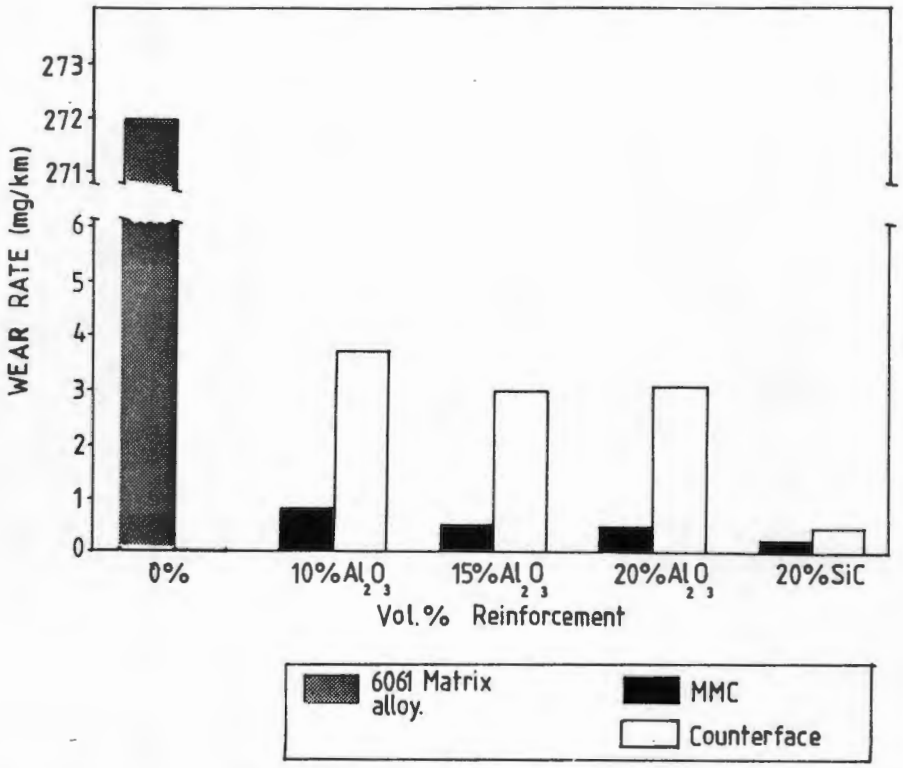

Fig.28: Reciprocating sliding steady-state wear rates for each of the 6061 composites, the unreinforced 6061 matrix alloy and respective stainless steel counterfaces.

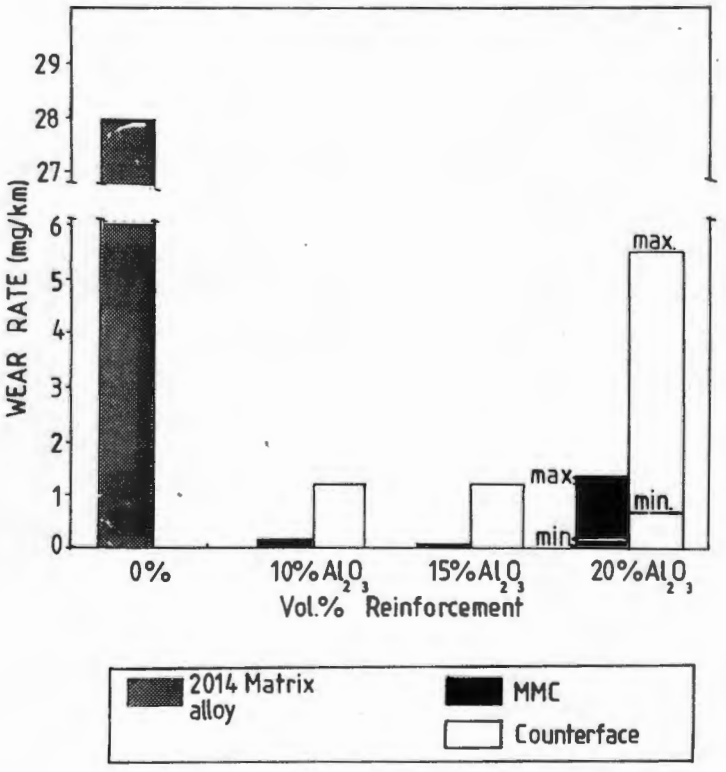

Fig.29: Reciprocating sliding steady-state wear rates for each of the 2014 composites, the unreinforced 2014 matrix alloy and respective stainless steel counterfaces. The wear behaviour of the 20 vol.% Al_2O_3 composite was noticeably erratic, showing, in most tests, an initial low wear rate followed by a period of greater slider and counterface material loss.

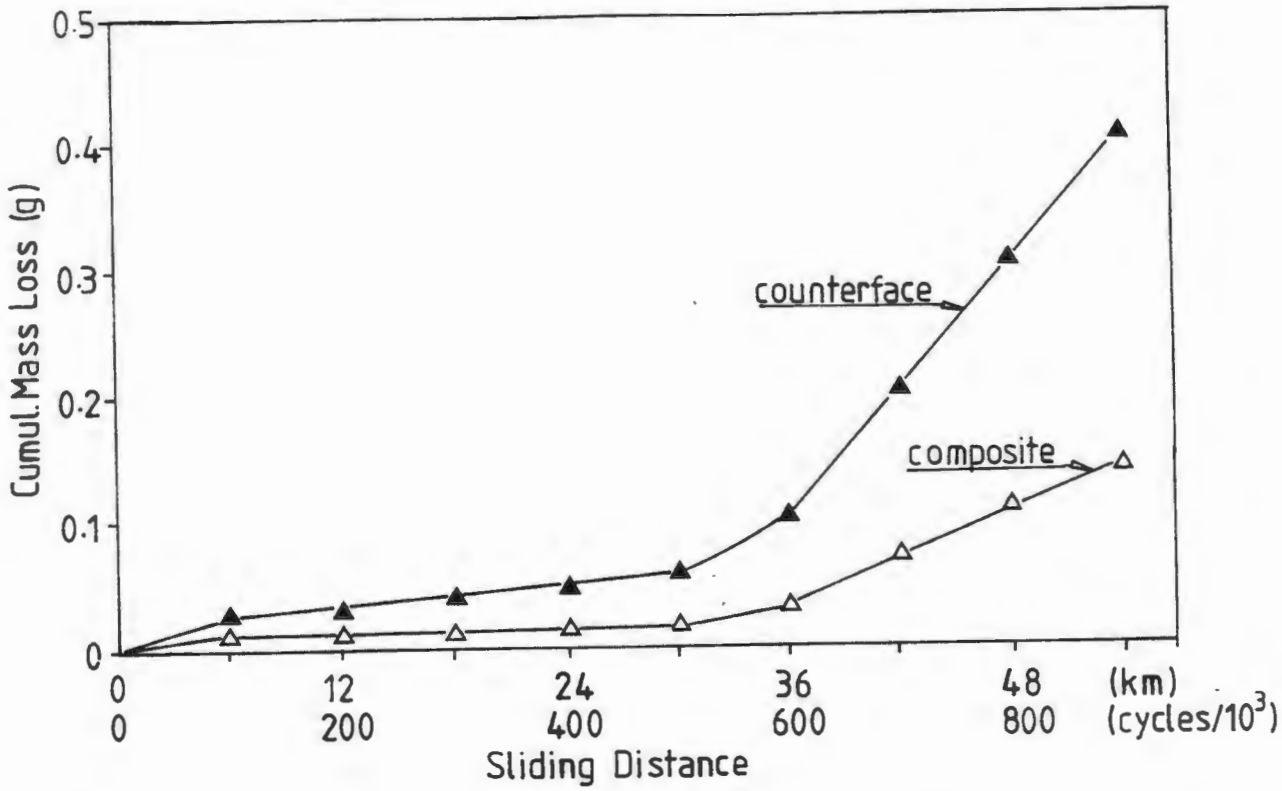

Fig.30: Cumulative mass losses of the 2014 alloy reinforced with 20 vol.% Al_2O_3 and counterface from a typical reciprocating sliding wear test. The onset of a high wear regime is a characteristic feature of the wear test.

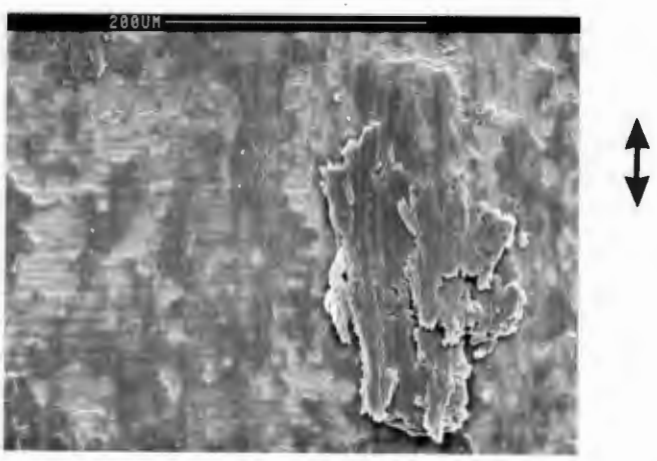

Fig.31: Electron micrograph of a stainless steel counterface after being worn to steady state against the 6061 matrix alloy. Aluminium has transferred to the counterface surface during the sliding process together with the generation of flake-like debris. Arrow indicates sliding direction.

The 20 vol.% Al_2O_3 reinforced 2014 alloy displayed a somewhat erratic wear behaviour, exhibiting both high and low steady state wear regimes. A plot of cumulative mass losses from a typical sliding wear test is shown as a function of sliding distance in fig.30. The composite has an initial low wear loss regime which is followed by a period of higher slider and counterface wear loss. The onset of the high wear rate regime occurs in the region of $5x10^5$ reciprocating cycles, although in other tests this was erratic, occurring anywhere between $8x10^5$ to around 1.5 x 10^6 cycles.

The surface of a counterface worn by the unreinforced 6061 alloy is shown in fig.31. The counterface shows evidence of typical adhesive wear phenomena with the formation of an aluminium transfer film on its surface. A large flake-like debris particle is shown, which is about to decohere from a thinner, older transfer film. The 2014 alloy showed a similar transfer mode but there was less evidence of large flake debris formation.

A scanning electron micrograph of the 20 vol.% SiC reinforced 6061 alloy after 60 km of sliding is shown in fig.32a. The worn surface of the composite has been taper sectioned and polished to reveal the extent of subsurface damage. The micrograph shows the base of a wear groove where fractured particulate debris is evident together with stainless steel transfer from the counterface. The counterface material is lighter in contrast compared to the surrounding matrix alloy and is concentrated in the area near the base of the wear groove. An Fe X-ray map of the same area in fig.32a is displayed in fig.32b showing the distribution of the counterface fragments in the subsurface wear zone. Similar features were observed in taper sections of each worn composite. The electron micrograph shown in fig.33 is a counterface which has been worn by the 15 vol.% Al_2O_3 reinforced 6061 alloy. The original grinding marks on the counterface have been completely worn away in the region of contact and there is no evidence of aluminium transfer from the sliding sample to the steel surface. In some instances, counterfaces worn by the alumina reinforced alloys showed evidence of transfer of sliding sample material. This was particularly so for the 10 vol.% Al_2O_3 6061 composite and the 20 vol.% Al_2O_3 reinforced 2014 alloy and fig. 34 is an example of this phenomenon showing patches of transferred material adhering to a counterface, after it has been worn to steady state against the 20 vol.% Al_2O_3 2014 composite.

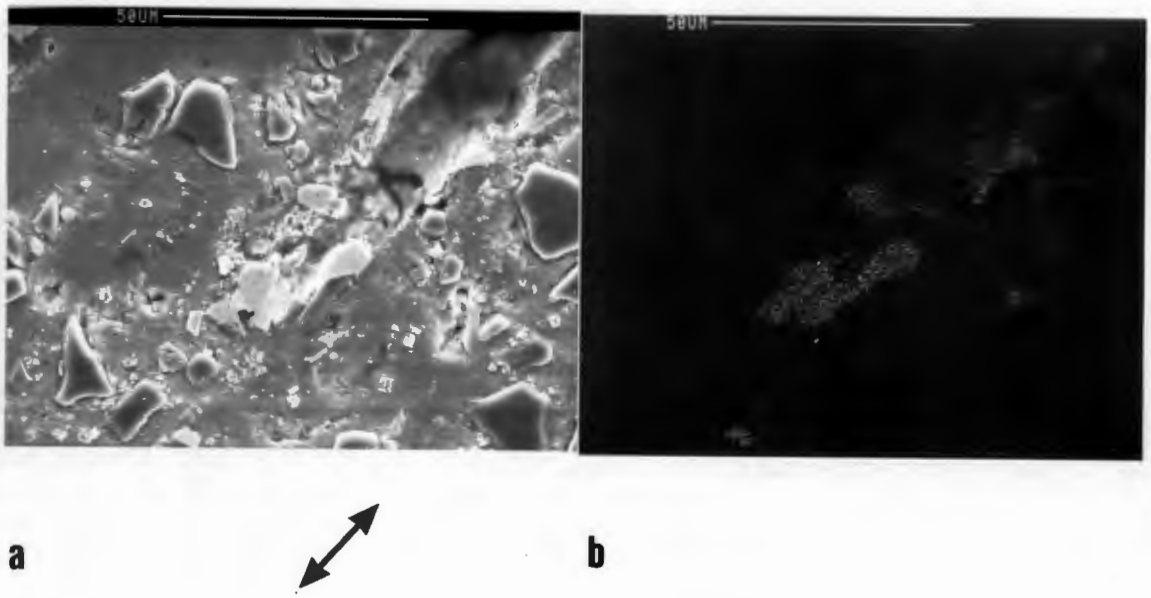

Fig.32a and 32b: Taper section (5°) of the 20 vol.% SiC reinforced 6061 alloy surface after being worn to steady state during reciprocating sliding, against a stainless steel counterface. Stainless steel debris, transferred during the sliding process, is visible as lighter inclusions in the subsurface region of a wear groove. Arrow indicates sliding direction and taper direction. The top of the micrograph is the wear surface region. Fig.32b shows an Fe-Xray map of the same region shown in fig.32a, displaying the distribution of steel debris in the subsurface wear zone.

A scanning electron micrograph of the steady state worn surface of the 20 vol.% Al_2O_3 6061 composite sliding sample is shown in fig.35. The worn surface is typical of that found for the alumina reinforced 6061 alloys and the 10 vol.% and 15 vol.% Al_2O_3 reinforced 2014 alloys, where a smooth layer of oxide products and particulate fragments have smeared over the contact surface during the sliding operation. The electron micrograph in fig.36a shows a very similar worn surface morphology of the 15 vol.% Al_2O_3 6061 composite, at higher magnification. Both counterface debris and particulate fragments are embedded in the composite's surface, showing up as lighter inclusions in the darker matrix. The presence of counterface debris is verified by the Fe-Xray distribution map of the same region displayed in fig.36b. Oxidation products are also visible on the worn surface.

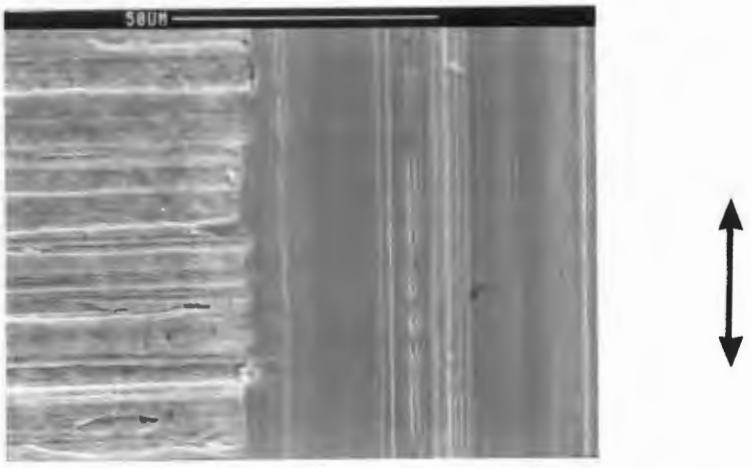

Fig.33: Electron micrograph showing abrasive wear mode of stainless steel counterface after reciprocating sliding against the 15 vol.% Al_2O_3 reinforced 6061 alloy. Arrow indicates sliding direction.

Fig.34: Counterface surface after being worn by the 20 vol.% Al_2O_3 reinforced 2014 alloy, showing debris transfer to the stainless steel surface. Arrow indicates sliding direction.

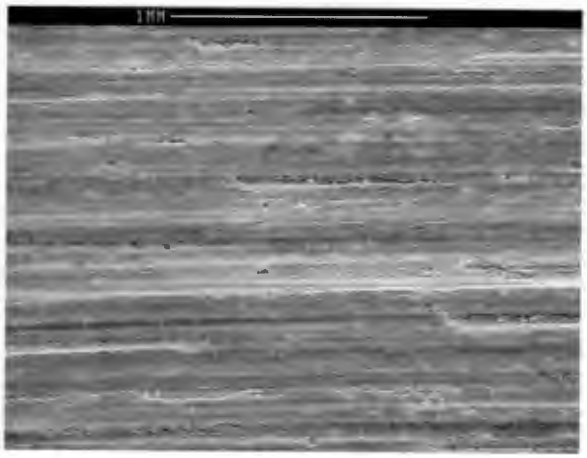

Fig.35: Low magnification scanning electron micrograph of the surface of the 20 vol.% Al_2O_3 reinforced 6061 alloy, having been worn to steady state conditions. The surface morphology is typical of that found for all of the alumina reinforced alloys.

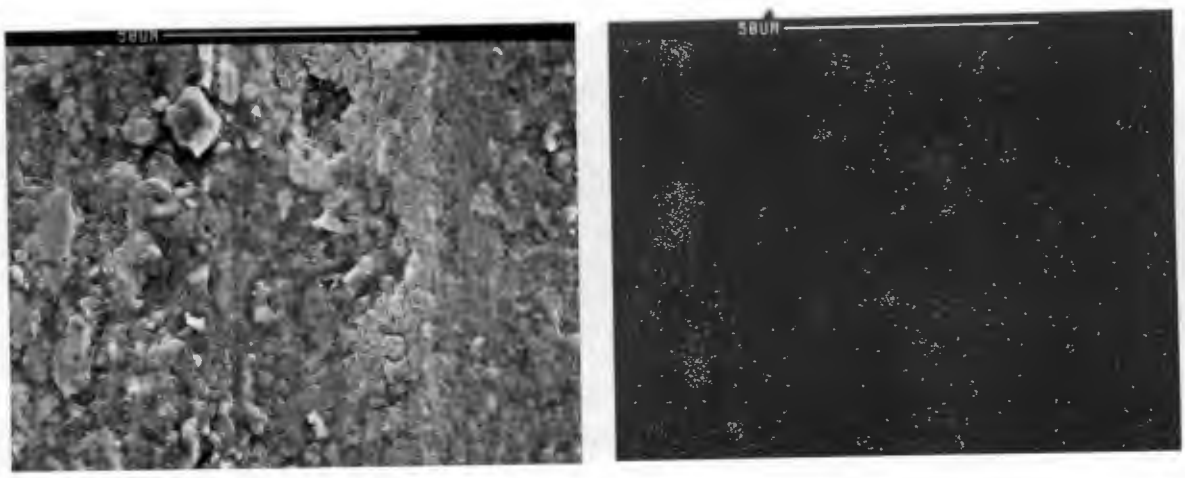

a **b**

Fig.36a and 36b: Fig.36a shows a high magnification scanning electron micrograph showing the steady-state worn surface of the 15 vol.% Al_2O_3 reinforced 6061 alloy. Both counterface debris and alumina fragments are embedded in the worn surface, showing up as lighter inclusions. The surface morphology is typical of that found for the alumina reinforced alloys. Fig.36b shows an Fe X-ray map of the same area displayed in fig.36a, showing the distribution of steel counterface debris in the worn surface.

The steady state worn surface of the 20 vol.% SiC reinforced 6061 alloy is shown in fig. 37. When compared to the other 6061 composites, and the 10 vol.% and 15 vol.% Al_2O_3 2014 composites, the surface morphology is decidedly more irregular in appearance, consisting of raised areas of smoothed matrix alloy amongst deep abrasion tracks and heavily deformed regions. Closer examination of the smoothed asperities, shown in the high magnification micrograph in fig.38, reveals significantly less oxide, counterface and reinforcing particulate debris entrainment, when compared to the worn surfaces of the alumina reinforced alloys.

Worn specimens of the 15 vol.% and 20 vol.% Al_2O_3 reinforced 2014 alloys, are displayed in figs.39 and 40 respectively. The surface of the 20 vol.% reinforced alloy is noticeably more fractured in appearance in comparison to the 15 vol.% material. Patches of transferred material containing particulate and counterface debris, which show up as lighter regions of contrast in the micrograph, appear to have decohered, thus exposing the underlying material giving a more fractured and plastically deformed appearance.

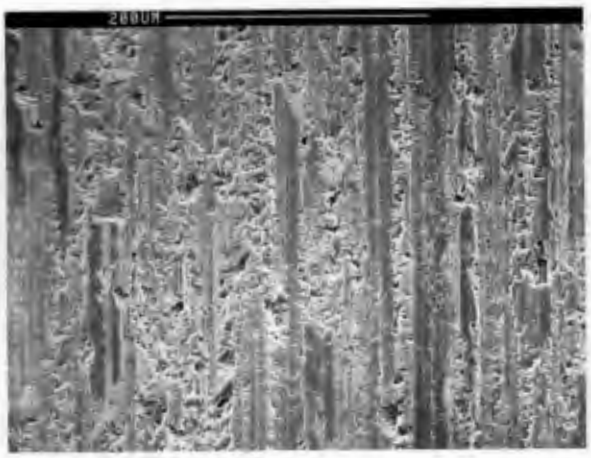

37

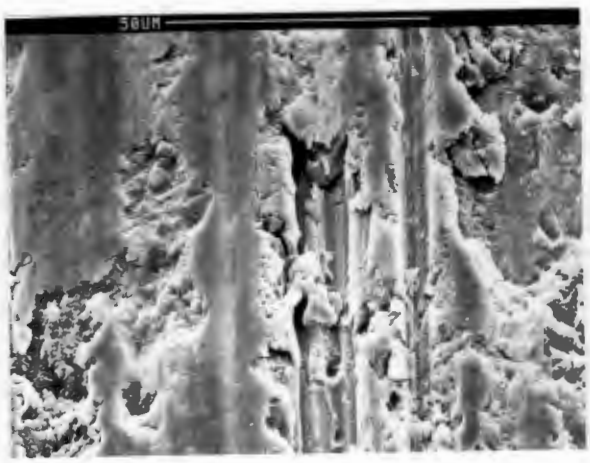

38

Fig.37: Steady state worn surface of the 20 vol.% SiC reinforced 6061 alloy. The surface morphology consists of raised areas of smoothed matrix alloy amongst patches of heavily deformed material.

Fig.38: High magnification electron micrograph of the worn composite surface that is exhibited in fig.37. A smoothed asperity is displayed, showing less reinforcing particulate and counterface debris entrainment as compared to what is observed for the worn surfaces of the alumina reinforced alloys.

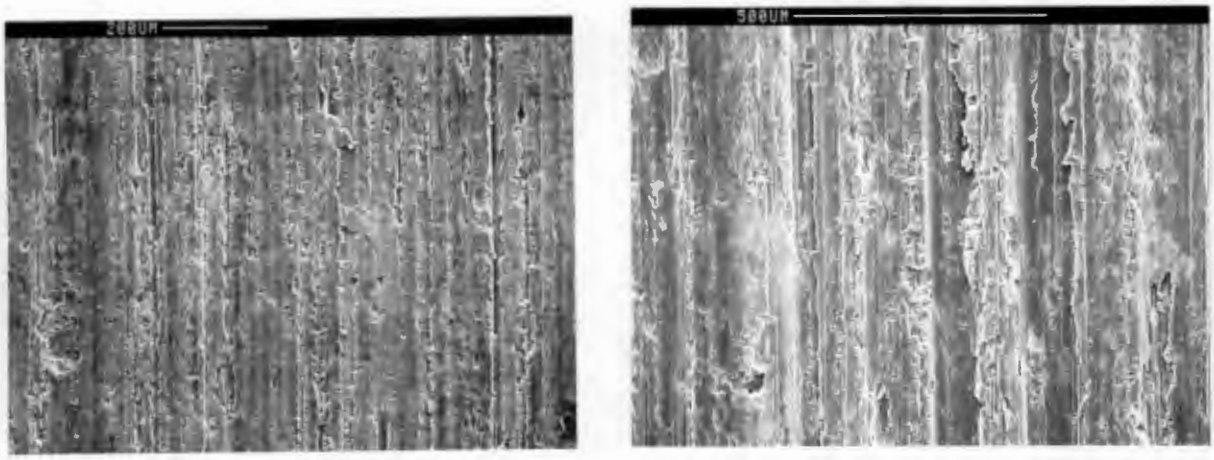

39 40

Fig.39: The steady-state worn surface of the 15 vol.% Al_2O_3 reinforced 2014 alloy.

Fig.40: The steady-state (high wear rate regime) worn surface of the 20 vol.% Al_2O_3 reinforced 2014 alloy. Note the fractured appearance of the worn surface compared to that displayed in fig.39.

Optical micrographs depicting the subsurface deformation in each of the unreinforced 6061 and 2014 alloys, which have been worn to steady state conditions, are displayed in figs. 41 and 42 respectively. Each alloy specimen has been sectioned perpendicular to the worn surface and parallel to the direction of sliding, so as to reveal the extent of plastic strain accommodation in the subsurface wear regions. The accumulation of subsurface shear is revealed by the presence of two sets of slip lines in the 6061 alloy, which extend to some 100-150μm below the contact surface. In contrast, the 2014 alloy has a greater subsurface strain gradient, where plastic deformation of the metal extends to around 30μm below the worn surface. The 2014 alloy has a much smaller grain size (5-10μm) compared to that of the 6061 alloy (20-100μm), making the detection of any slip lines within their interiors difficult. Of note is the large degree of plastic bending of the grains in one direction in the 2014 alloy, despite the fact that the specimen traverses in reciprocating motion against the counterface. There appears to be no major evidence of directionality in the subsurface regions of the 6061 alloy. The 2014 alloy shows an appreciable amount of work hardening in the subsurface wear region, as is revealed in the microhardness plot in fig.43. In comparison, the 6061 alloy undergoes very little hardening, despite showing prominent slip accommodation to much larger subsurface depths in the range 100-150μm.

With the addition of ceramic reinforcement to each of the aluminium alloys,

subsurface plastic strain gradients are increased during the sliding process and shear of the aluminium matrix becomes highly localised near the wear surface. These effects are more dramatic in the 6061 composites as is evident in fig.44, where the subsurface region of the 15 vol.% Al_2O_3 6061 composite is displayed. The micrograph shows a section taken parallel to the sliding direction, where plastic deformation and shear is localised to a region of approximately 40μm below the worn surface. There is extensive evidence for shear failure in the matrix alloy in the heavily sheared region immediately below the wear surface, probably arising at particulate interfaces. There is also evidence of particulate fracture in this narrow region.

Large strain gradients are also visible in the subsurface sections of the 10 vol.% and 20 vol.% Al_2O_3 reinforced 2014 composites in figs.45 and 46a respectively. There is evidence for subsurface cracking below the worn surface of the 10 vol.% composite, but this is confined to the heavily sheared transfer layer region. The 20 vol.% composite on the other hand, exhibits subsurface fracture of particulates to depths of approximately 40μm below its worn surface. Note that there is very little plastic shear of the matrix material in this region. Evidence for subsurface cracking of the transfer layer was also found, as is displayed in fig.46b.

The extent to which work-hardening occurs in the subsurface regions of interparticulate matrix alloy, in the two 2014 matrix composites containing 10 vol.% and 20 vol.% alumina is presented in fig.47. Subsurface microhardness measurements were made on 5° taper sections beneath the worn surfaces of each composite, and are compared to the subsurface work-hardening data of the monolithic 2014 alloy originally displayed in fig.43. The peak hardness values obtained for the two composites are below those found in the near surface region of the unreinforced alloy. Of the two composites, the one containing 20 vol.% alumina has the lowest peak subsurface hardness. Both composites display a sharper drop in hardness with depth below their respective worn surfaces, in comparison to that obtained for the monolithic alloy which has a gentler subsurface hardness gradient. There is no significant difference between the subsurface hardness gradients obtained for the two composite materials.

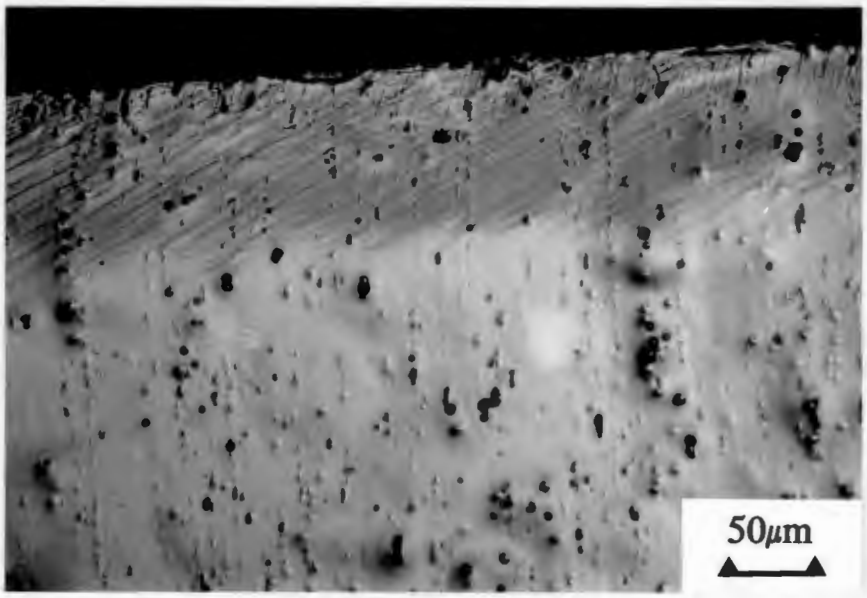

Fig.41: Optical micrograph of the subsurface deformation (perpendicular section) present in the unreinforced 6061 alloy, after being worn to steady state in reciprocating sliding conditions. The region shown is an anomalously large single grain in the subsurface wear region - all the slip lines are oriented in the same direction. Arrow indicates sliding direction.

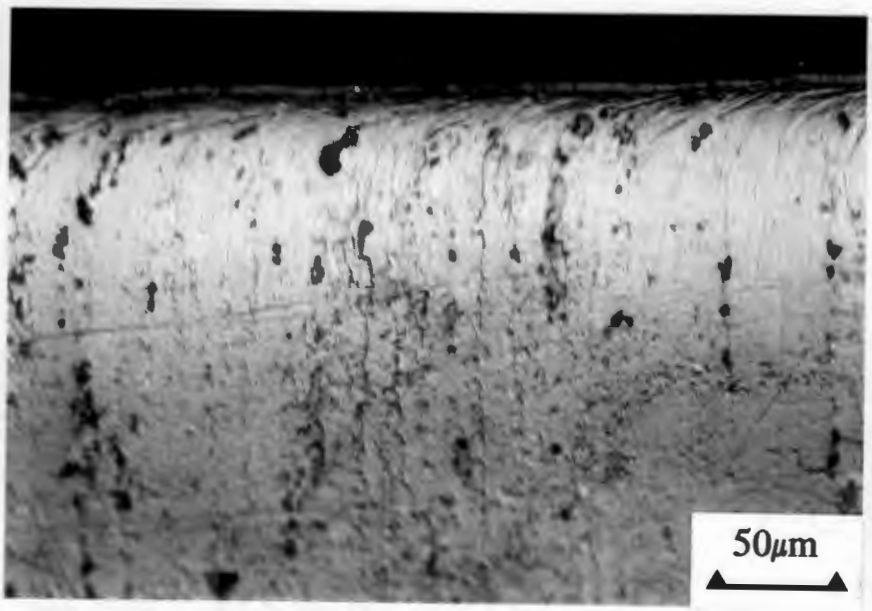

Fig.42: Optical micrograph of the subsurface deformation (perpendicular section) present in the unreinforced 2014 alloy, after being worn to steady state in reciprocating sliding conditions. Arrow indicates sliding direction. Note that this alloy has a larger subsurface strain gradient compared to the 6061 alloy shown in fig.41.

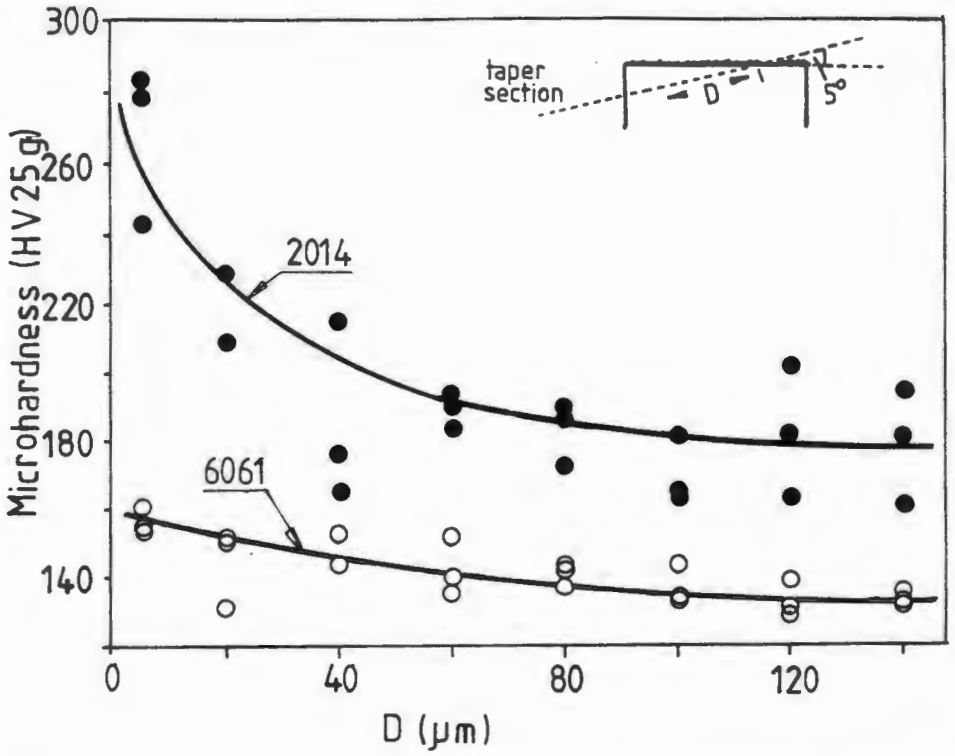

Fig.43: Plot of subsurface microhardness variations beneath the steady-state worn surfaces of the monolithic 6061 and 2014 alloys.

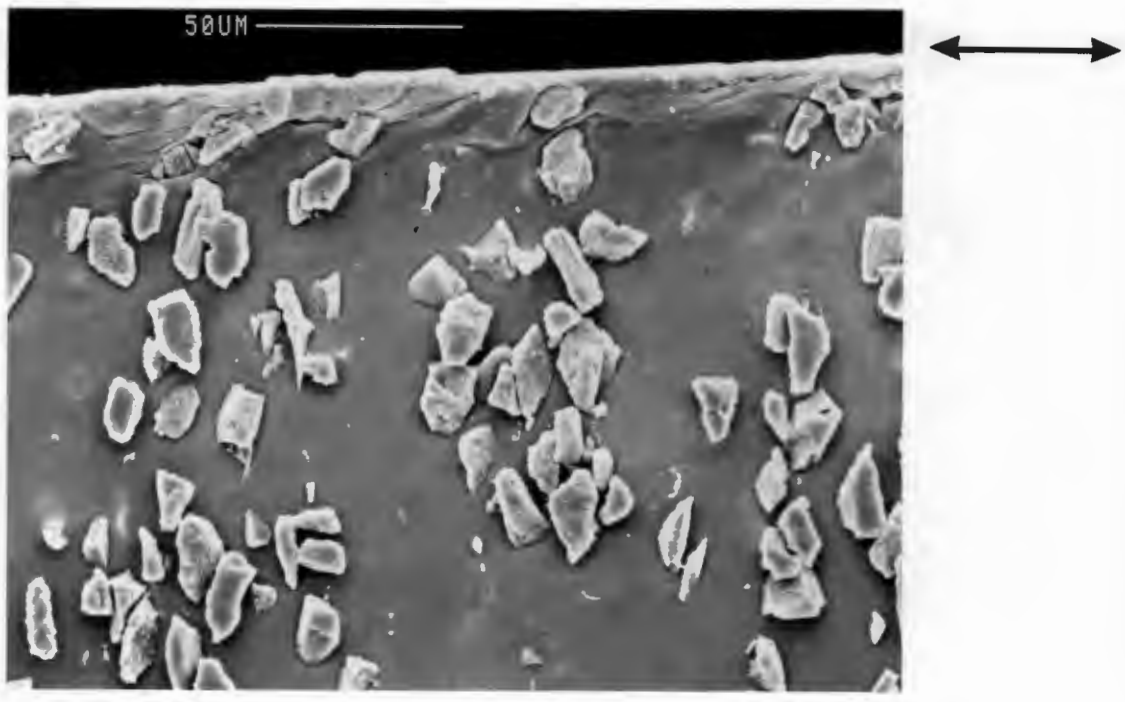

Fig.44: Scanning electron micrograph of the subsurface region (perpendicular section) of the steady state worn 15 vol.% Al_2O_3 reinforced 6061 alloy. Shear failure of the matrix alloy accompanied by some particulate fracture, has occurred in the heavily sheared region immediately below the worn surface.

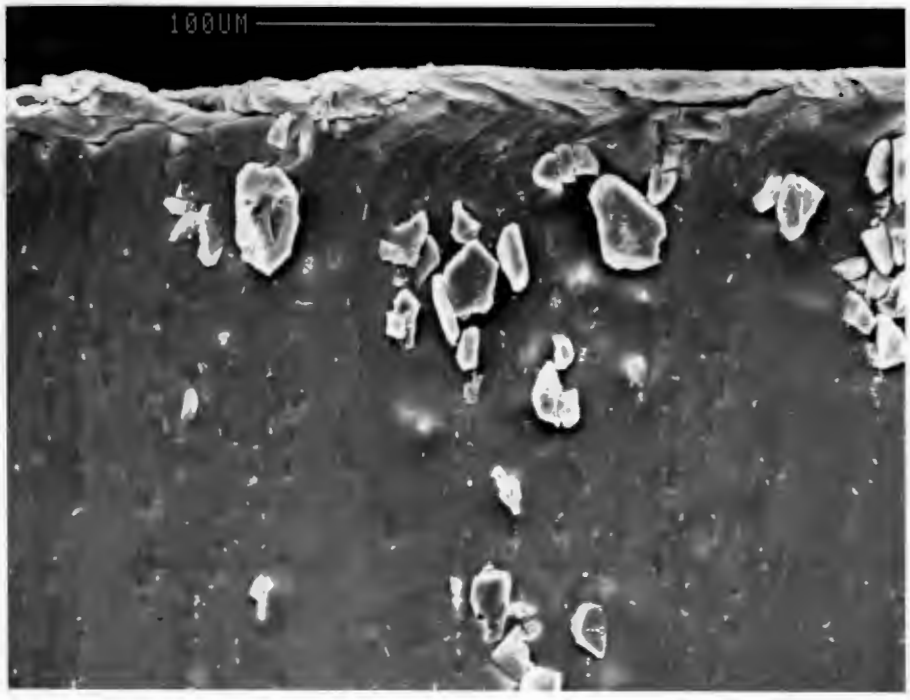

Fig.45: Scanning electron micrograph of the subsurface region (perpendicular section) of the steady state worn 10 vol.% Al_2O_3 reinforced 2014 alloy. Extensive shear failure of the matrix alloy has occurred in the surface wear zone.

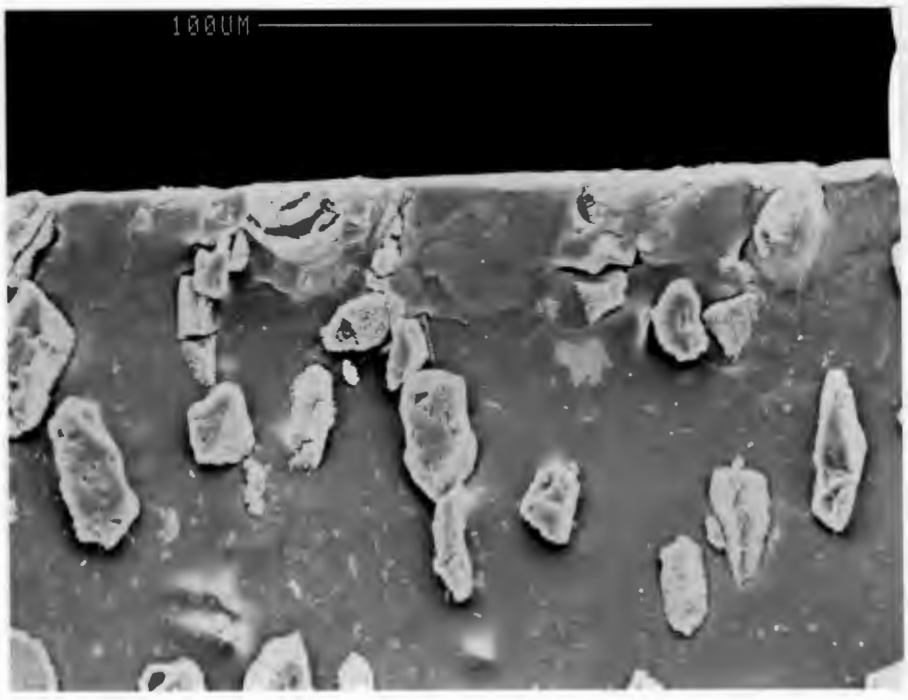

Fig.46a: Electron micrograph of the subsurface region (perpendicular section) of the steady state worn (high wear regime) 20 vol.% Al_2O_3 reinforced 2014 alloy. There is evidence for subsurface cracking of particulates approximately 40μm below the worn surface. Arrow indicates sliding direction.

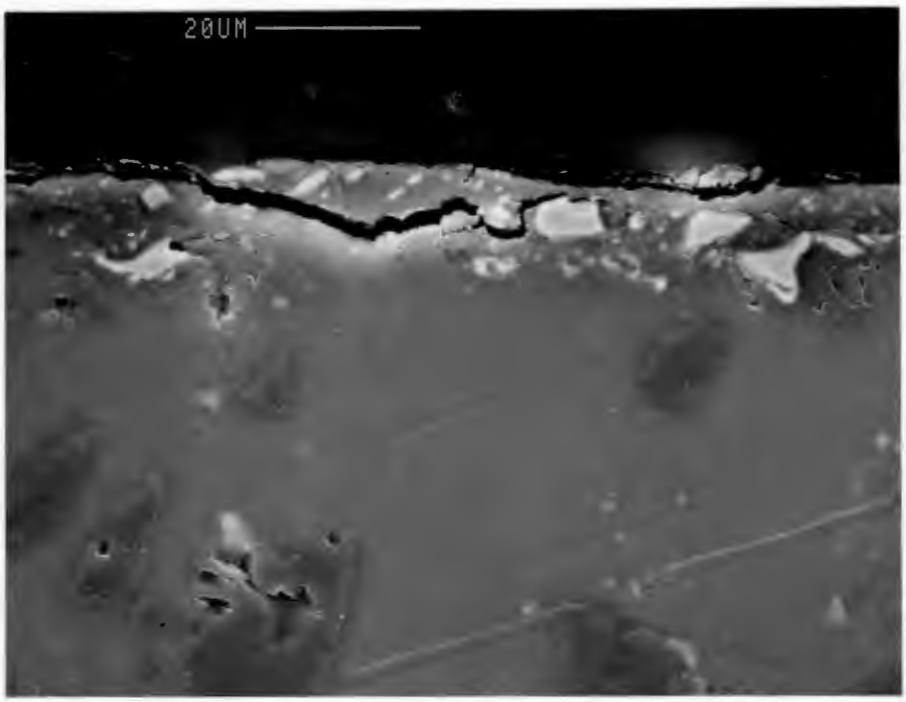

Fig.46b: Electron micrograph showing delamination of surface transfer layer in the 20 vol.% Al_2O_3 reinforced 2014 alloy. The subsurface section was obtained from a composite sample that had been worn into the steady-state high wear rate regime.

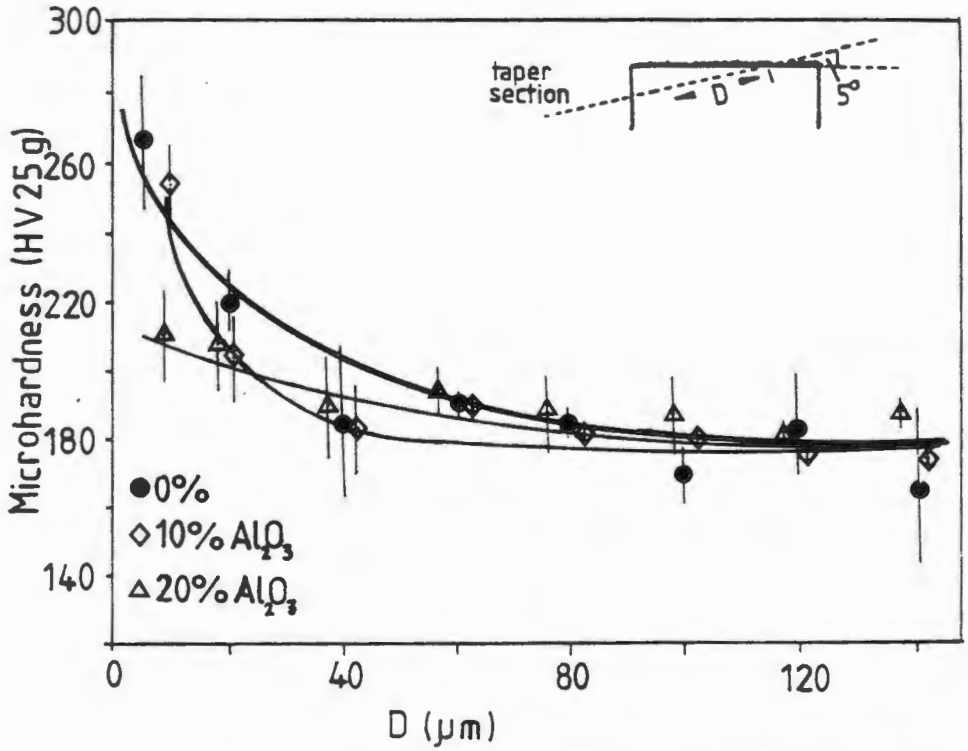

Fig.47: Plot of subsurface microhardness variations beneath the steady state worn surfaces of the monolithic 2014 alloy and the two 10 vol.% and 20 vol.% alumina reinforced 2014 alloy composites.

4.4.1 *Dislocation substructures and transfer layer characterisation*

The subsurface dislocation configurations associated with the worn 6061 monolith and two reinforced 6061 matrix composites, containing 10 vol.% and 20 vol.% alumina particulates, are shown in figs. 48 to 50 respectively. The micrographs in figs. 48 and 49 were obtained from TEM foil specimens which had been thinned to a depth of approximately 60 μm below the worn surface of each material. In the 20 vol.% alumina reinforced alloy, the microstructure shown (fig.50) is from a region approximately 20 μm below the worn surface. Each specimen had been worn to steady state conditions, corresponding to over 10^5 cycles of reciprocating contact.

The dislocation substructures observed in both the composites and monolithic alloy closely resemble those found in face centered cubic metals having a high stacking fault energy, and which have been subjected to fatigue deformation [107-112]. The microstructure associated with the unreinforced alloy in fig.48a shows an extremely high density of dislocations which are arranged in a distinct cell-like morphology. A higher magnification micrograph in fig.48b shows the cell walls and their interiors, within which dislocations are barely resolved. There is no detectable crystallographic misorientation or tilt contrast between cells, indicating that the total Burgers vector in them approaches zero so that the long range interactions between positive and negative dislocations cancel each other [107].

The regions of high dislocation density are comparable in morphology to the persistent slip band (PSB) features found in cyclically deformed copper single crystals [107,108,111,112]. Cell features develop from labyrinth structures of PSB walls and dislocation deficient matrix veins as the imposed plastic strain amplitude (γ_{pl}) is increased to levels greater than about 10^{-3} [108].

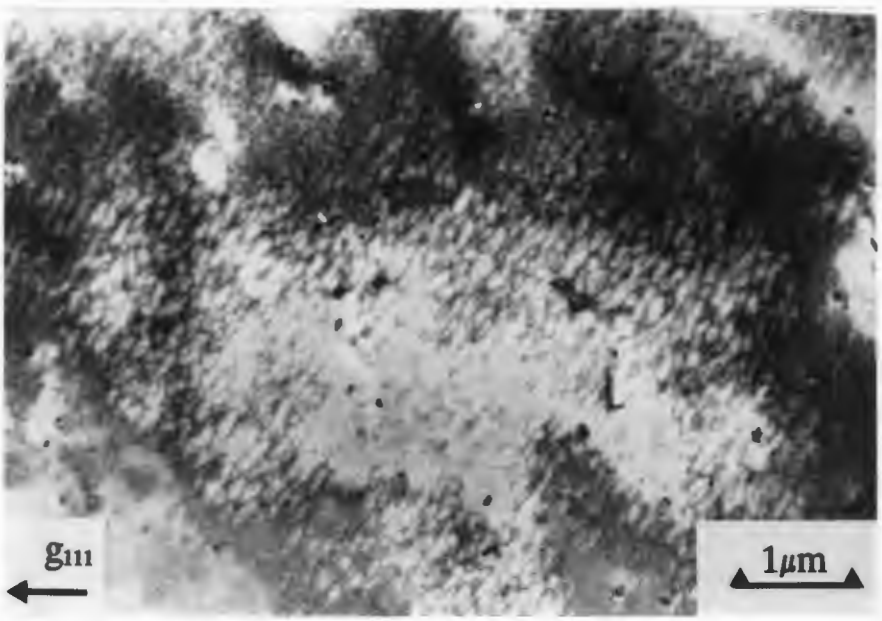

Fig.48a: Transmission electron micrograph showing cell-like dislocation substructure in the unreinforced 6061 alloy, which has been worn to steady state under reciprocating sliding conditions. The region shown is approximately 60μm below the worn surface of the slider.

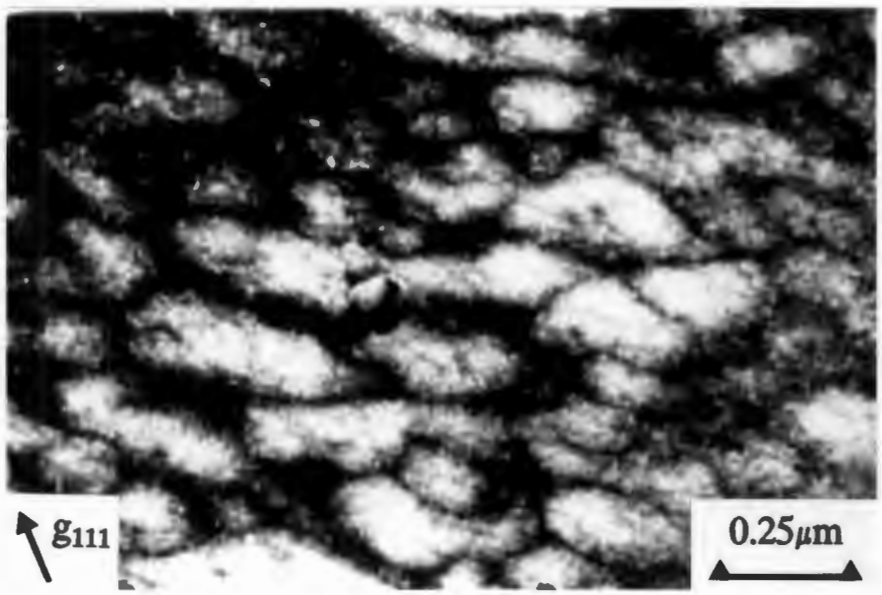

Fig.48b: Higher magnification micrograph of the cell structure shown in fig.48a. Note the extremely high dislocation density in the cell walls, where it is difficult to resolve individual dislocations.

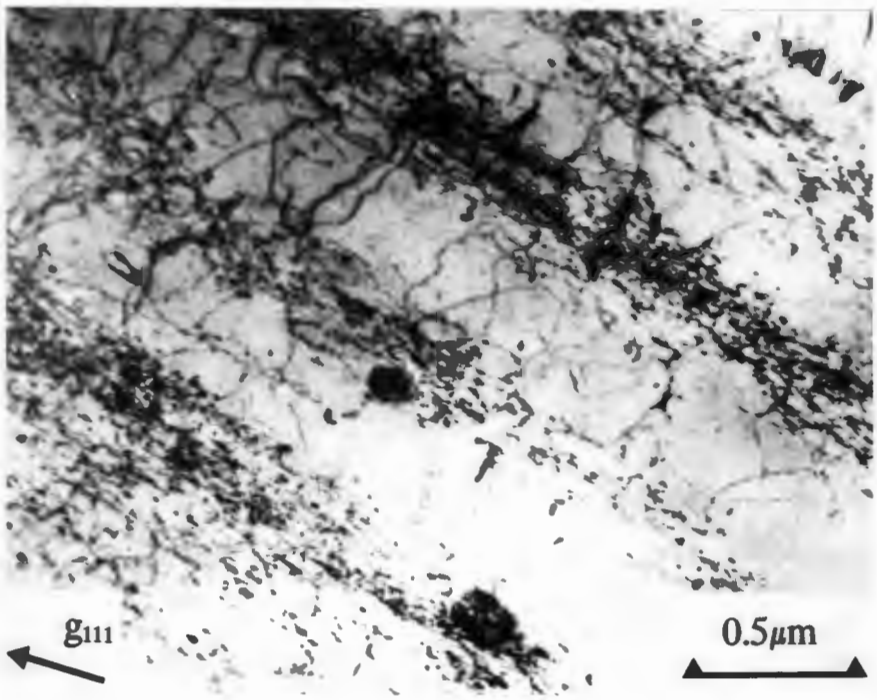

Fig.49a: Transmission electron micrograph of the dislocation substructure found in the 10 vol.% Al_2O_3 reinforced 6061 alloy, which has been worn to steady state (> 10^5 reciprocating cycles). The region displayed is approximately 60μm below the worn surface and shows a characteristic persistent slip band (PSB) "ladder" structure [109].

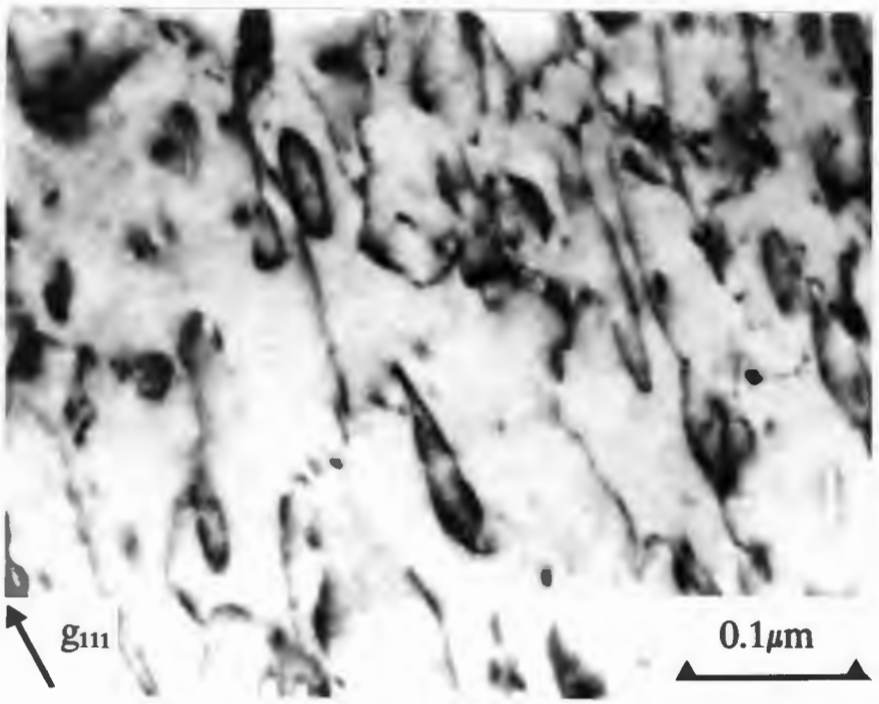

Fig.49b: Persistent slip band structure showing a high concentration of dislocation loops and jogs.

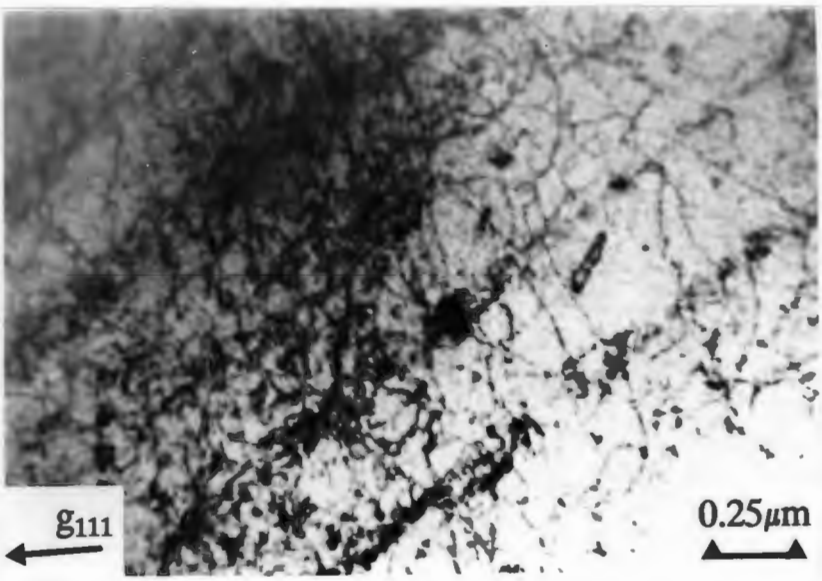

Fig.50: Transmission electron micrograph of the dislocation substructure found in the 20 vol.% Al_2O_3 reinforced 6061 alloy, which has been worn to steady state (> 10^5 reciprocating cycles). The region displayed is approximately 20 μm below the worn surface and also shows a PSB "ladder" structure, which is not as well defined as that exhibited in the 10 vol.% Al_2O_3 reinforced alloy.

In contrast, the dislocation substructure found in the 10 vol.% alumina reinforced alloy can be associated with the characteristic PSB "ladder" structure found in face centered cubic metals, which have been cyclically deformed at lower plastic strain amplitudes ie. $\gamma_{pl} < 10^{-3}$ [108,112]. The structure is composed of evenly spaced PSB regions of high dislocation density, separated by relatively dislocation free matrix regions. Closer inspection of the band structure in fig.49b, reveals a high concentration of dislocation loops and jogs, which are typical features of PSB's formed under low plastic strain amplitude cycling [109,111]. A similar, but less well defined "ladder" structure is found in the subsurface microstructure of the 20 vol.% alumina reinforced 6061 alloy in fig.50. The PSB walls are evenly spaced, being separated by matrix regions that are more heavily dislocated in comparison to those of the 10 vol.% alumina reinforced alloy.

Examination of the transfer layers formed on the steady-state worn contact surfaces of composites, was conducted on back thinned disc specimens of the composite wear layers, in the transmission electron microscope. The micrograph in fig.51 shows the transfer layer morphology associated with the 20 vol.% alumina reinforced 6061 alloy, displaying regions that are extremely fine grained in nature (approx. 20-100 nm). An area adjacent to this region is shown in fig.52, where the

fine grained transfer layer appears to have been removed by the thinning process. The micrograph shows a heavily deformed cell type substructure which is similar in morphology to that obtained by You et al [74], in their studies of subsurface deformation of aluminium matrix composites. In addtion the micrograph shows cell like crystallites which are approximately 100-300nm in diameter and show no preferred orientation. The small size of the crystallites is an indication that they are constantly being re-worked at the sliding interface, with there being little time available for grain growth by recovery and recrystallisation effects. The high sliding speeds used in this investigation are probably conducive to large flash temperatures arising at the sliding interface [113] although the presence of water would probably lower these heating effects to some extent; thereby reducing the chances of significant recovery and recrystallisation from occurring.

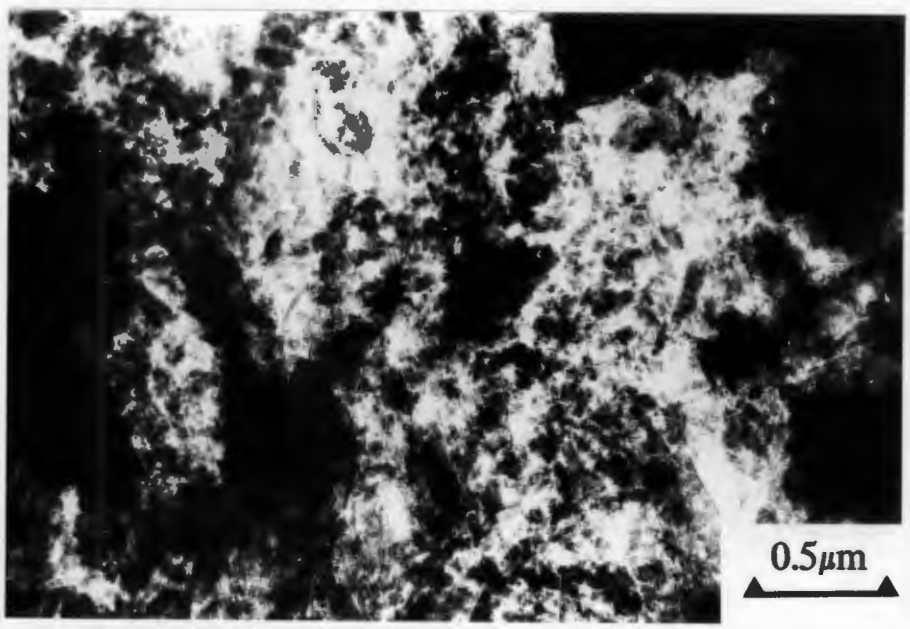

Fig.51: Transmission electron micrograph of the surface transfer layer formed during steady-state reciprocating wear of the 20 vol.% Al_2O_3 reinforced 6061 alloy. The microstructure is extremely fine grained in nature, with particle sizes ranging between 20-100nm.

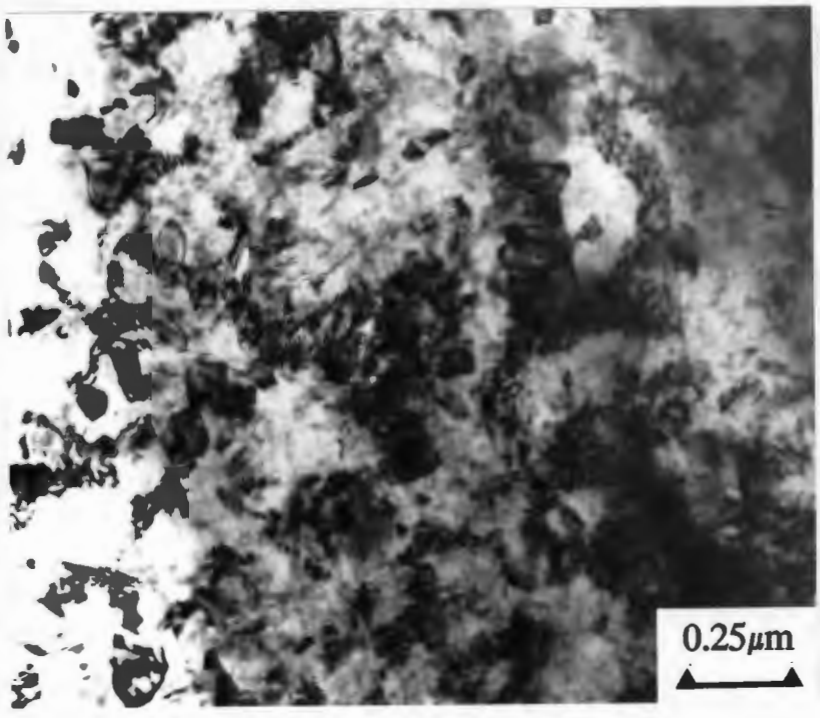

Fig.52: Transmission electron micrograph showing a heavily deformed cell/crystallite type microstructure, from a region of matrix alloy immediately below the fine grained transfer layer shown in fig.51.

A typical selected area diffraction pattern (SADP) of the wear transfer layer of the 20 vol.% alumina reinforced 6061 alloy, consisting of several rings, is shown in fig. 53. The fine grained structure of the transfer layer gives rise to several Debye-Scherrer rings. A Debye-Scherrer pattern of the 20 vol.% SiC reinforced 6061 alloy's wear transfer layer is presented in fig.54. The ring diameters were measured to an accuracy of 0.2 mm using a glass ruler, and the camera length of the TEM was calibrated using aluminium matrix reflections from several zone axis diffraction patterns. Lattice spacings associated with the prominent reflections in the diffraction patterns of the transfer layers of the two composites are listed in Table VI together with matching d-spacings of possible constituents. Common to both the alumina reinforced and silicon carbide reinforced alloys are the two strongest reflections having measured d-spacings of 2.02Å and 2.34Å, which correspond closely with Al_{200} (d = 2.02Å), Fe_{011} (d = 2.03Å) and Al_{111} (d = 2.33Å) reflections respectively. The presence of iron in the transfer layers is consistent with the observations made showing transfer of stainless steel to composite slider surfaces in figs.32 and 36b. The transfer layer of the alumina reinforced composite shows several d-spacings which correspond to those of alumina and which are absent in the SADP of the silicon carbide composite's layer.

Fig.53: Typical selected area diffraction pattern taken from the steady state wear transfer layer of the 20 vol.% alumina reinforced 6061 alloy.

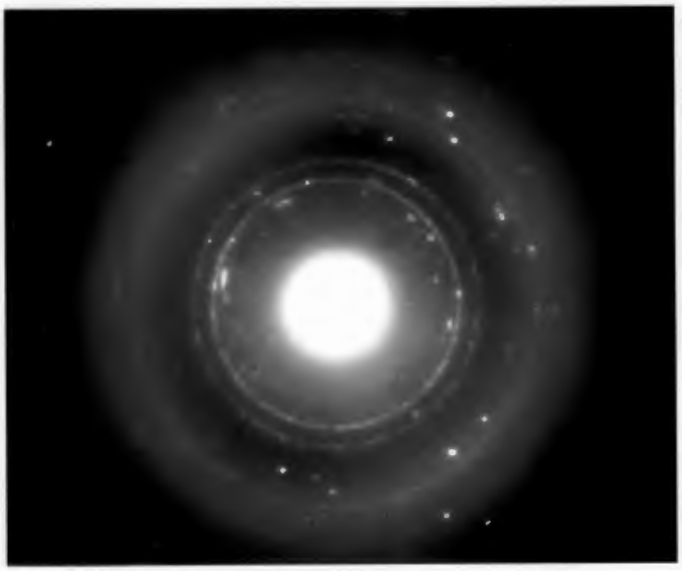

Fig.54: Typical selected area diffraction pattern from the steady state wear transfer layer of the 20 vol.% SiC reinforced 6061 alloy.

20 vol.% Al_2O_3 d-spacings (Å)	20 vol.% SiC d-spacings (Å)	Indexation of possible constituents
3.45	-	3.479Å - Al_2O_3 (012)
2.54	-	2.552Å - Al_2O_3 (104)
-	2.59	2.620Å - SiC (6H) (101)
2.34 (s)	2.35 (s)	2.338Å - Al (111)
2.02 (s)	2.02 (s)	2.025Å - Al (002)
		2.027Å - Fe (011)
1.60	-	1.601Å - Al_2O_3 (116)
1.42	1.43	1.432Å - Al (022)
		1.433Å - Fe (002)
1.38	-	1.374Å - Al_2O_3 (030)
1.22	-	1.221Å - Al (113)
		1.215Å - $MgAl_2O_4$ (700)
1.16	1.18	1.170Å - Fe (112)
		1.169Å - Al (222)

Table VI: Measured d-spacing values obtained from selected area Debye-Scherrer diffraction patterns of wear transfer layers from the 20 vol.% Al_2O_3 and 20 vol.% SiC reinforced 6061 alloys. Possible constituents and their d-spacings (ASTM powder diffraction data) have been assigned to the measured reflections. Note the strongest reflections "(s)", which are common to both composites.

4.5 Solid Particle Erosion

Plots of cumulative mass loss for solid particle erosion tests, conducted at an erosive impact angle of 90° to the sample surface for the 6061 and 2014 unreinforced and reinforced alloys, are shown in figs.55 and 56 respectively. Steady state erosion conditions are achieved after erosion by about 20g of erodent for the 6061 and 2014 alloys containing 20 vol.% Al_2O_3 as well as the 20 vol.% SiC reinforced 6061 alloy. Erosion behaviour for the other 6061 composites and unreinforced alloy is characterised by an initial mass gain "incubation period", with steady state behaviour noticeable after erosion by 35 grams of erodent in the case of the unreinforced 6061 alloy. The unreinforced 2014 alloy reaches steady state after erosion by 25 grams of erodent and is noticeably less erosion resistant than the softer 6061 alloy. All the reinforced alloys show a definite trend towards greater erosion rates with increasing volume fractions of reinforcement.

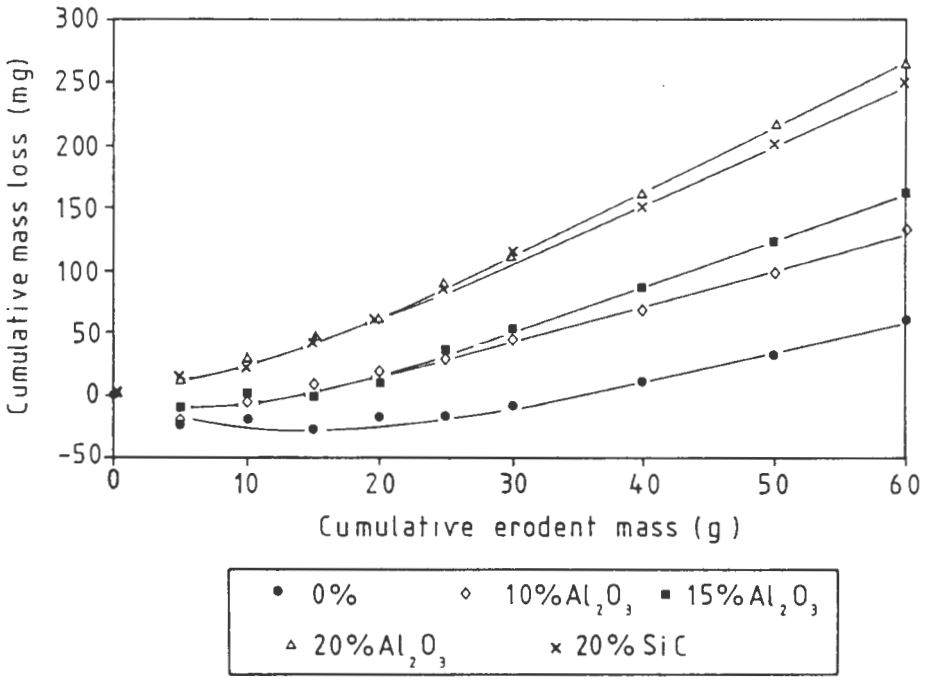

Fig.55: Cumulative mass losses of the 6061 matrix alloy and composites, for erosion by 120 grit SiC particles at a 90° impact angle and an average velocity of 60 ms^{-1}.

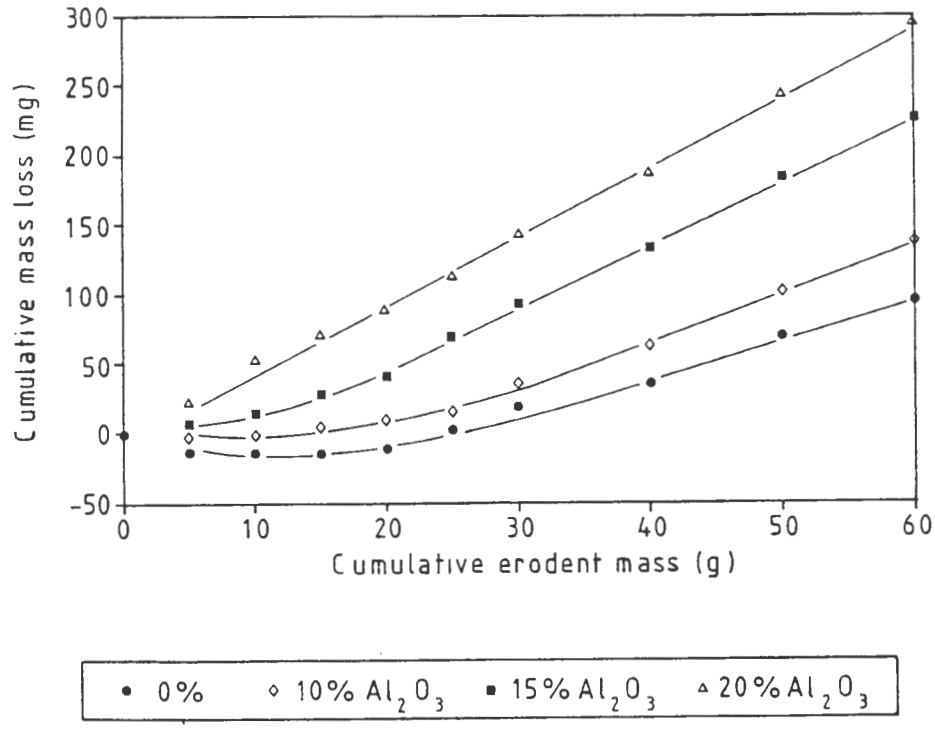

Fig.56: Cumulative mass losses of the 2014 matrix alloy and composites, for erosion by 120 grit SiC particles at a 90° impact angle and an average velocity of 60 ms^{-1}.

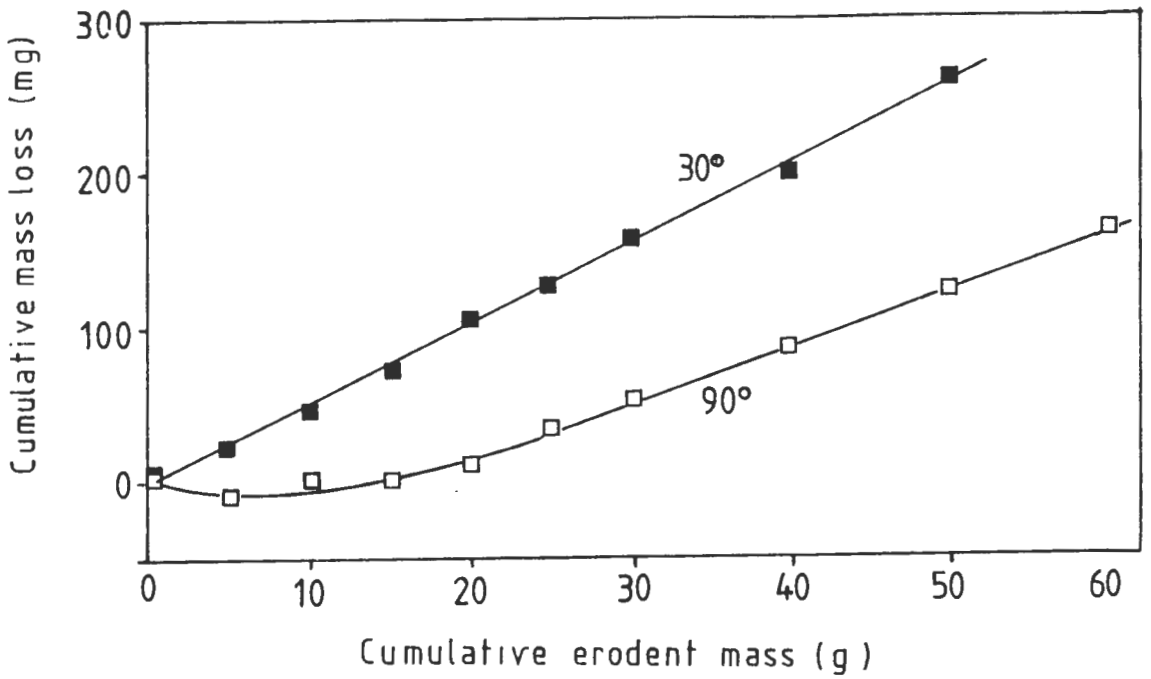

Fig.57: Plot showing the erosion behaviour of the 15 vol.% Al_2O_3 reinforced 6061 alloy at erosion impact angles of 90° and 30°.

Erosion at a 30° impact angle of all the composites is characterised by the immediate onset of steady state conditions. The plot in fig.57 compares the cumulative erosion losses of the 15 vol.% alumina reinforced 6061 alloy at both the 90° and 30° erosion impact angles. When the composite is eroded at 90°, it features an initial incubation period of mass gain, associated with the embedding of erodent particles and the build up of strain in its surface. Erosion at 30° shows no such incubation period which is an indication that the operative wear mode features minimal strain accumulation and work hardening effects accompanied by a more efficient removal of surface material by a possible cutting mechanism. The bar chart in fig.58 shows steady state erosion rates obtained at 90° and 30° impact angles for each material. Steady state erosion rates were determined from the slopes of linear regions (steady state) of the cumulative erosion mass loss curves of each material. The erosion rates at the 30° impact angle are higher for every composite and both unreinforced alloys compared to those found under 90° impact conditions. Both the unreinforced and 10 vol.% Al_2O_3 reinforced 6061 alloys display erosion rates at 30° impact conditions that are higher than those of their 2014 counterparts of equivalent volume fraction. Under eroding conditions at 90° impact, this trend is reversed where the softer 6061 monolithic alloy and 10 vol.% Al_2O_3 composite have lower erosion rates compared to their 2014 matrix

alloy counterparts. The 20 vol.% Al_2O_3 reinforced 6061 alloy exhibits similar erosion rates to those of the 2014 alloy reinforced with the same alumina content, at both impact angles. In comparison to the other 6061 matrix composites, the 20 vol.% SiC reinforced 6061 alloy exhibits a smaller difference in erosion rate between the two impacting conditions. Moreover, this composite shows erosion rates which are less than both of the 20 vol.% Al_2O_3 reinforced alloys.

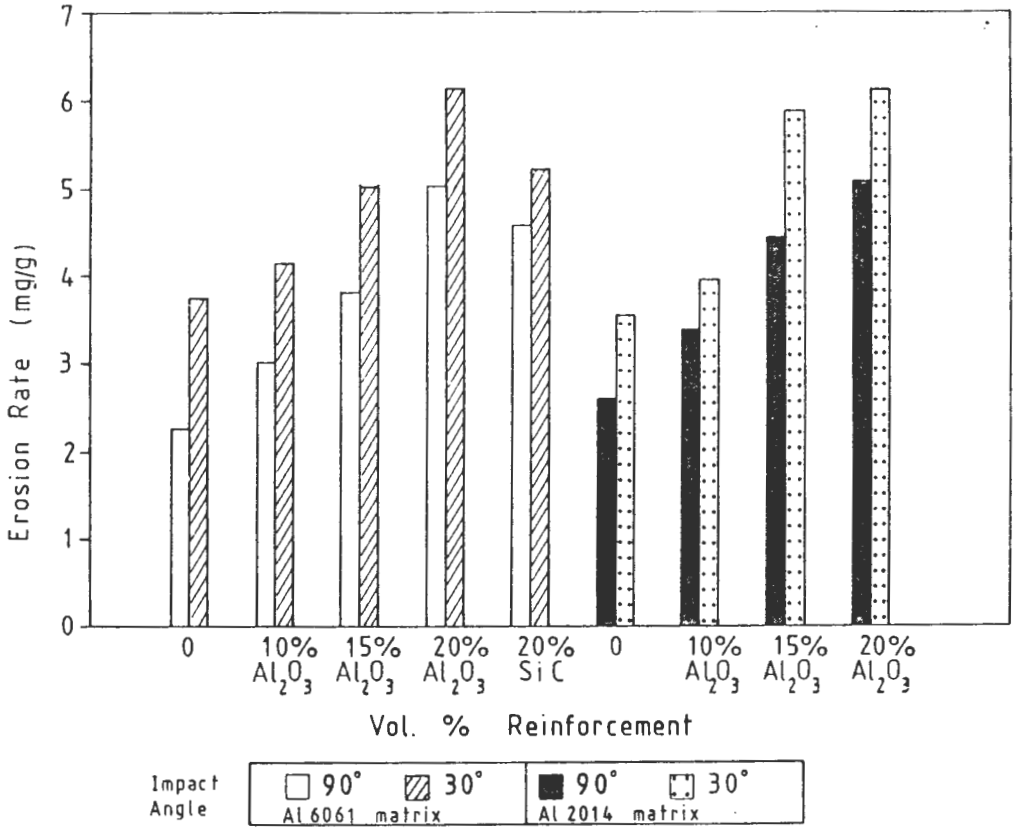

Fig.58: Steady-state solid particle erosion rates for the two matrix alloy composite systems at erodent impact angles of 90° and 30°.

Electron micrographs of the unreinforced 6061 alloy and its 20 vol.% SiC reinforced counterpart, showing typical steady state eroded surfaces at impact conditions of 90° and 30°, are displayed in figs. 59a to 59d. The unreinforced alloy eroded at 90° in fig.59a shows extensive plastic deformation and ductile shear fracture of its surface. The predominance of micromachining and cutting of material is observed when the impact angle is 30° in the micrograph shown in fig.59b. The surface of the composite eroded at 90° also shows extensive plastic deformation and shear fracture, but is considerably less ductile and more fractured in appearance compared to the monolithic alloy at the same eroding conditions. This micrograph also shows evidence of an eroding particle fragment having embedded into its surface. The eroded surface of the composite at 30° impact conditions in fig.59d, shows a similar transition to cutting and

micromachining as that found in the monolithic alloy. However, the composite's eroded surface features a distinct lack of ductility accompanied by extensive fracture and fragmentation of material in each impact zone.

Single impact sites on the surfaces of monolithic and reinforced alloys, at the two impact angles, are shown in figs.60a-d. The scanning electron micrograph in fig.60a shows a pair of 90° impact sites on the surface of the monolithic 6061 alloy. The impacting particles have made a deep impressions in the alloy which are surrounded by plastically deformed metal with there being no apparent evidence of fracture or material loss. A micrograph showing the same monolithic alloy with a 30° impact site on its surface is displayed in fig.60b. The impact area shows evidence of micromachining marks and an extruded lip of deformed metal where the particle has cut through the target surface at a low angle. Here again, the metal at the impact site has undergone a ductile microforging process with there being little evidence of any material removal.

A scanning electron micrograph depicting a single impact site at 90° to the surface of the 2014 alloy reinforced with 20 vol.% alumina, is shown in fig.60c. The impacting particle has deformed the matrix alloy accompanied by multiple fracture of a nearby particulate. There is evidence of intense deformation, as well as highly constrained extrusion and fracture of the matrix alloy having occurred in the region adjacent to the reinforcing particulates in the impact site. The micrograph in fig.60d shows the same composite surface with a 30° impact site. The impacting particle has displaced the matrix alloy in a similar micromachining operation to that found in the monolithic alloy in fig.60b, but is also accompanied by fracture of alumina reinforcing particulates and microextrusion and fracture of displaced metal.

The nature and extent of subsurface deformation in both the 6061 and 2014 unreinforced alloys, at erodent impact angles of 90° and 30°, are shown in figs.61. The figures show optical micrograph taper sections (5°) of each alloy's steady state eroded surface. The subsurface deformation strain in the 6061 alloy eroded at 90° in fig.61a, extends to a greater depth compared to that found under 30° eroding conditions in fig.61b. A similar comparison can be made for the harder 2014 monolithic alloy, eroded at the 90° and 30° impact conditions and displayed in figs 61c and 61d respectively. The 2014 alloy shows less subsurface strain accommodation compared to the softer 6061 alloy at 90° impact, yet there is no significant difference in depth of deformation strain between the two alloys at 30° eroding conditions. Both alloys show extensive evidence of erodent particle

fragments having embedded and fractured in their eroded surfaces under 90° impact. There is little evidence for this having occurred at 30° impact in either of the alloys. In addition, there appears to be no significant difference in the degree of deformation that has occurred in each alloy at either impact angle; the surface metal showing equivalent and extensive deformation and fragmentation in each micrograph.

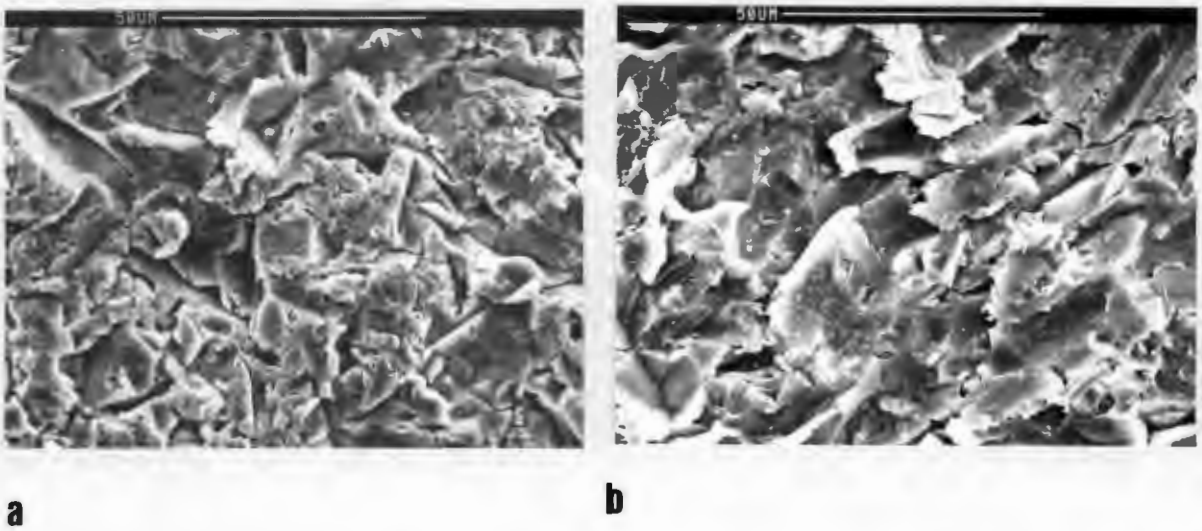

Figs.59a and 59b: Steady-state solid particle eroded surfaces of the unreinforced 6061 alloy, at erodent impact angles of 90° and 30° respectively.

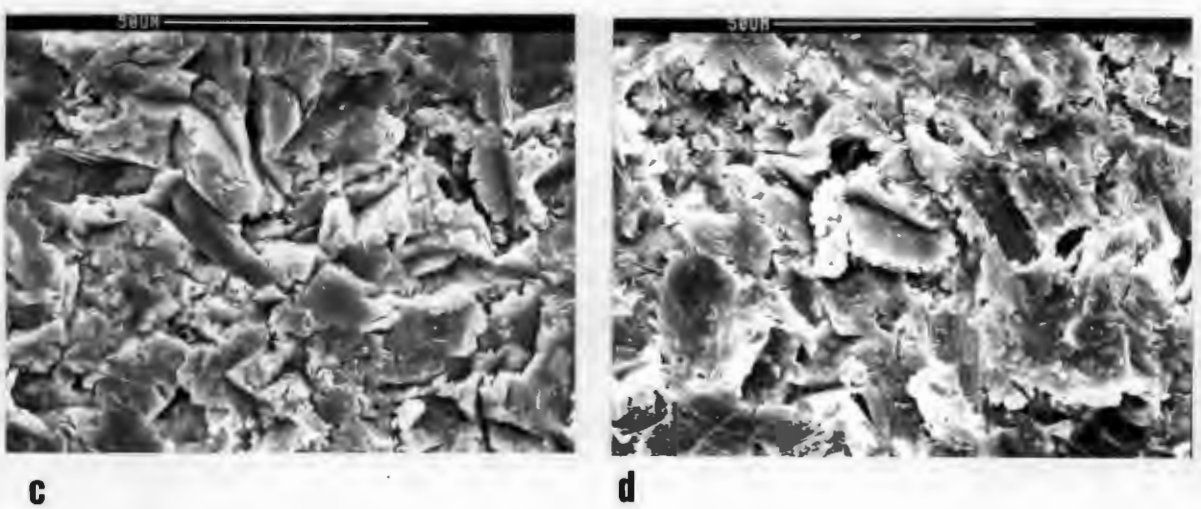

Figs.59c and 59d: Steady-state solid particle eroded surfaces of the 20 vol.% SiC reinforced 6061 alloy, at erodent impact angles of 90° and 30° respectively.

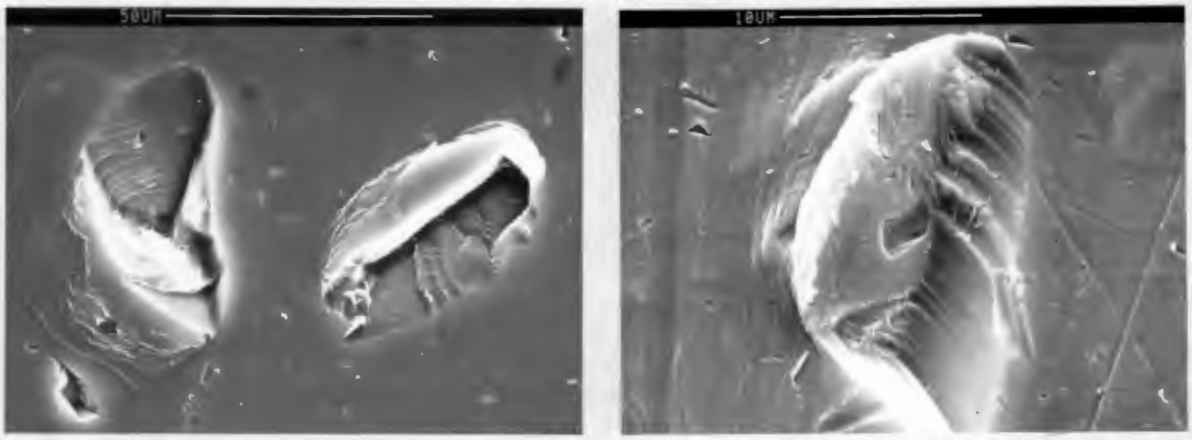

a b

Fig.60a and 60b: Scanning electron micrographs of single impact sites in the monolithic 6061 alloy at 90° and 30° impact angles respectively. Note the large amount of ductility associated with each impact. The 30° impact site shows micromachining and displacement of aluminium to form an extruded lip.

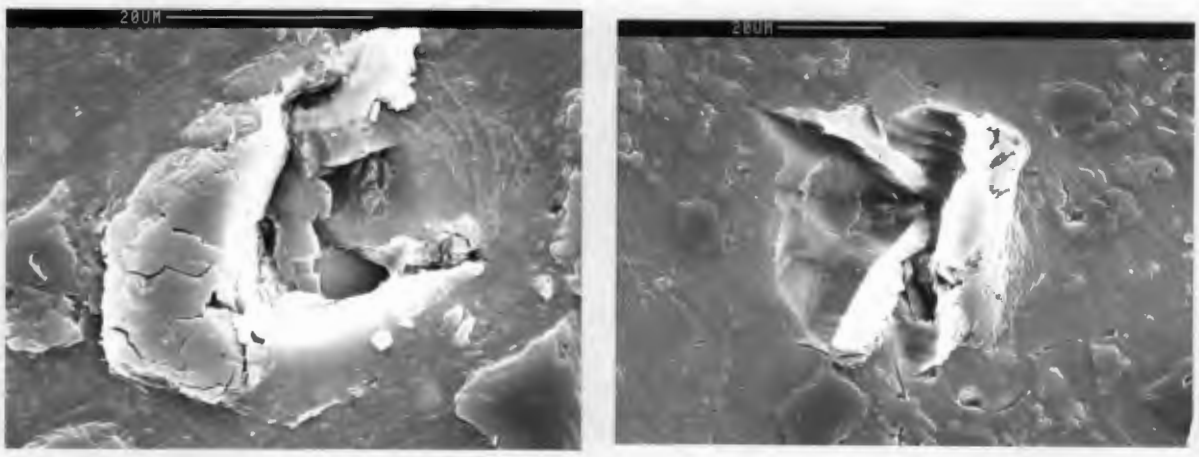

c d

Fig.60c and 60d: Scanning electron micrographs of single impact sites in the 2014 alloy reinforced with 20 vol.% alumina, at 90° and 30° impact angles respectively. Note the lack of ductility and extensive fracture associated with each impact site.

Subsurface taper section (5°) optical micrographs in figs. 62a and 62b, show the extent of microstructural deformation in the 20 vol.% SiC reinforced 6061 alloy at erosion impact conditions of 90° and 30° respectively. Widespread particulate fracture accompanied by extensive plastic deformation in the subsurface regions at

both impacting angles, is evident in the two micrographs. The depth of damage accumulation is greatest in the composite eroded at 90°, yet does not appear to show as significant a difference with that found in the 30° eroded composite, compared to the larger difference obtained in the 6061 monolithic alloy in figs.61a and 61b.

The transmission electron micrograph in fig.63 shows the dislocation substructure obtained in the matrix of the 20 vol.% Al_2O_3 reinforced 6061 alloy after solid particle erosion at 90° impacting conditions. The structure is from a region approximately 50μm below the eroded surface of the composite and is comprised of a subgrain structure consisting of walls of loose tangles of dislocations surrounding comparatively dislocation free areas. Similar subgrain structures have been observed in eroded copper specimens [114] and closely resemble the subgrain dislocation configurations found in cold worked aluminium [115,116].

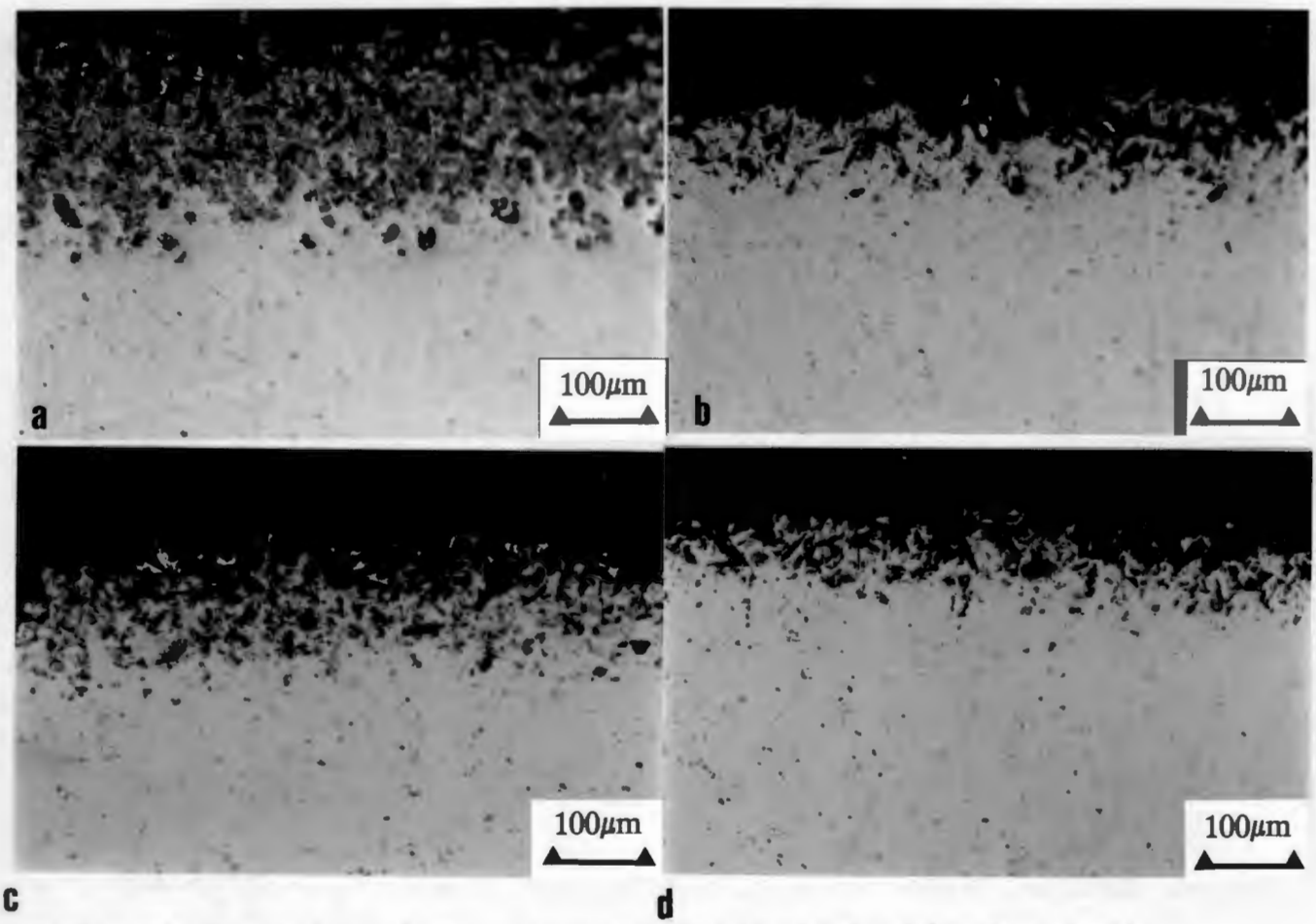

Fig.61a to 61d: Optical micrographs (5° taper section) showing the subsurface deformation obtained in the unreinforced 6061 and 2014 alloys, after having been eroded to steady state under 90° and 30° impacting conditions. Figs.61a and 61b show erosion at 90° and 30° impact angles in the 6061 alloy respectively. Figs.61c and 61d show erosion at 90° and 30° impact angles in the 2014 alloy respectively. Note the greater subsurface deformation associated with erosion under 90° impact conditions.

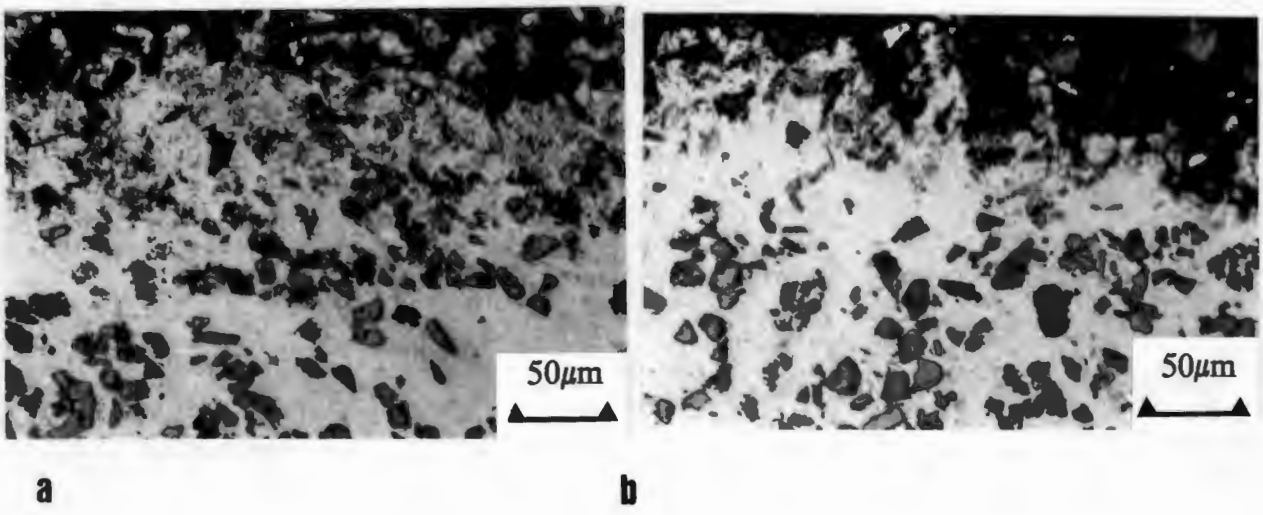

Fig.62a and 62b: Optical micrographs (5° taper section) showing the subsurface deformation and particulate fracture obtained in the 20 vol.% SiC reinforced 6061 alloy, after having been eroded to steady state under 90° and 30° impacting conditions respectively.

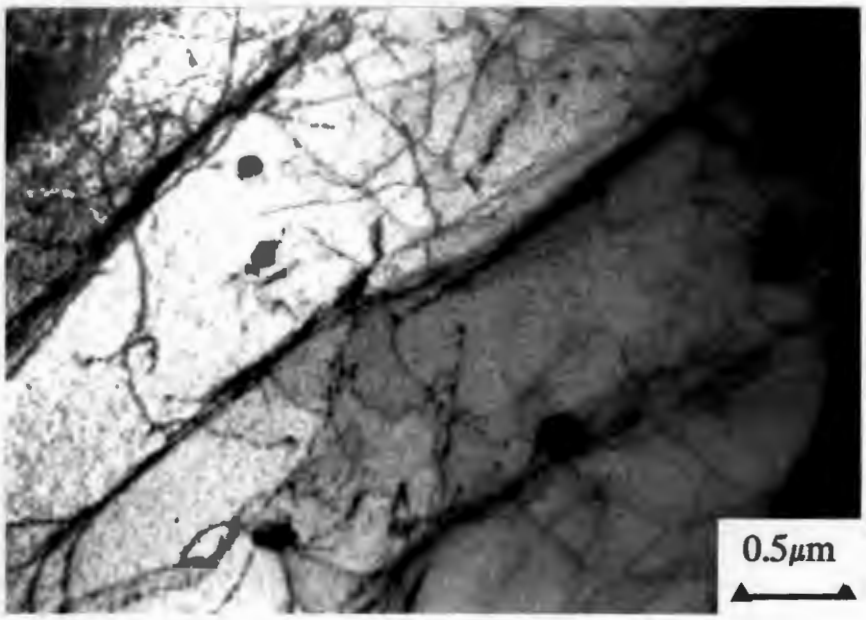

Fig.63: Transmission electron micrograph showing the dislocation structure in the matrix of the 20 vol.% Al_2O_3 reinforced 6061 alloy, after being eroded by solid particles to steady state conditions. The microstructure is from a region of material some 50μm below the eroded surface and shows a subgrain structure comprised of loose tangles of dislocations surrounding relatively dislocation free regions.

4.6 Cavitation Erosion Results

The plots of cumulative mass losses for each of the 6061 composites and monolithic alloy as a function of cavitation erosion time, are shown in fig.64. Each composite and unreinforced alloy display an initial incubation period of some four minutes before appreciable material losses occur. Mass losses extend into a steady state regime with the alumina reinforced composites displaying higher erosion rates. The erosion rate of the unreinforced alloy is below that of the alumina reinforced composites and is marginally above that of the SiC reinforced alloy.

Cavitation erosion mass losses for each of the 2014 composites and monolith are shown in fig.65. Each of the 2014 materials display incubation erosion periods of some six minutes; these are slightly greater than those obtained for the 6061 matrix materials. A bar chart showing the steady state erosion rates of the two matrix alloys and various composites is presented in fig.66. Overall, the 2014 composites and unreinforced alloy display erosion rates below those of their 6061 counterparts. A definite trend in erosion loss, based on volume fraction of reinforcement is evident in the 2014 materials, with the 20 vol.% Al_2O_3 reinforced 2014 alloy showing the highest and its unreinforced matrix alloy the lowest erosion rates in the steady state regime.

Scanning electron micrographs showing the surface of the unreinforced 2014 alloy after having been exposed to cavitating conditions for approximately two, five and sixty minute periods are displayed in figs.67a-c respectively. The micrograph sequence shows the nucleation of ductile shear deformation occurring at grain boundaries (5-10μm in diameter) in the initial stages of erosion, followed by more extensive plastic deformation in the steady state. The eroded surface of the 2014 alloy containing 20 vol.% alumina particulates is shown in figs. 68a and 68b after erosion times of approximately five and ten minutes respectively. The matrix alloy has undergone extensive deformation accompanied by void nucleation and intense shear at particulate interfaces. The particulates have also become more exposed during the erosion process.

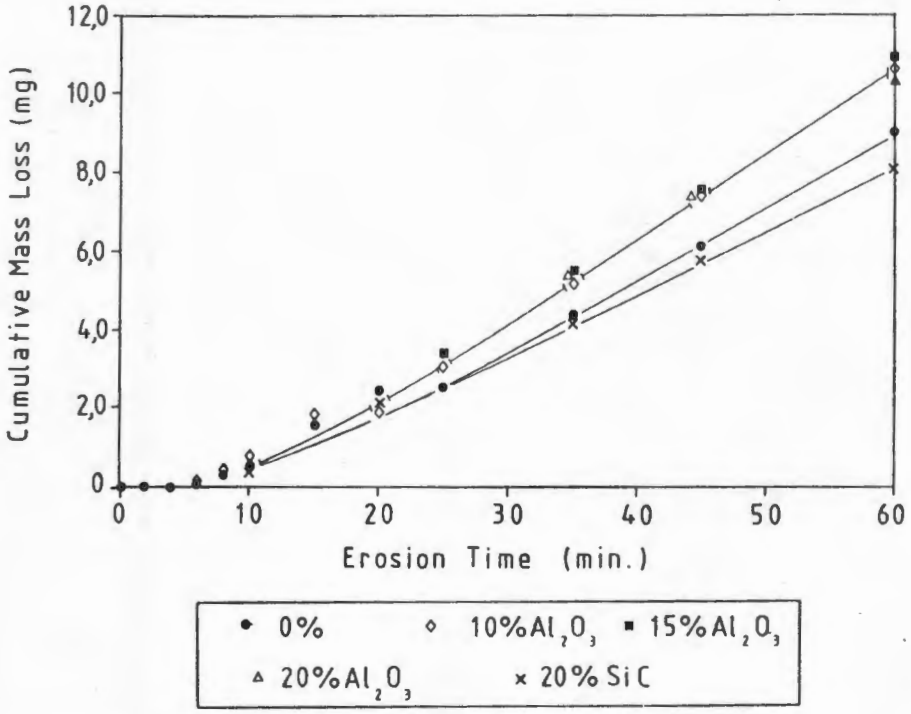

Fig.64: Cumulative mass losses of the unreinforced and reinforced 6061 matrix alloys shown as a function of exposure time to vibratory cavitation erosion.

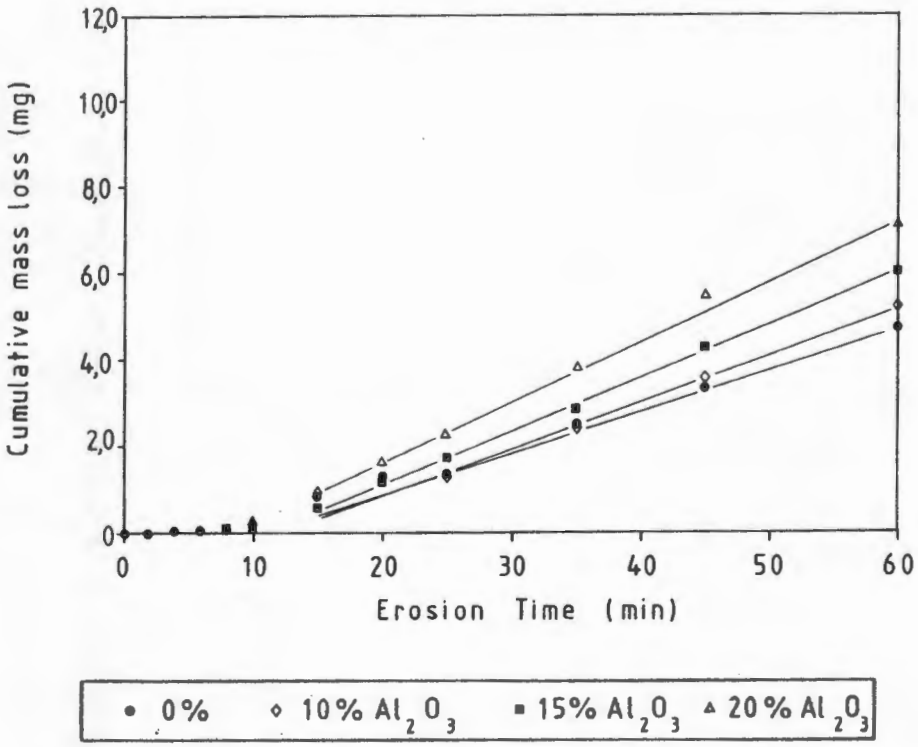

Fig.65: Cumulative mass losses of the unreinforced and reinforced 2014 matrix alloys shown as a function of exposure time to vibratory cavitation erosion.

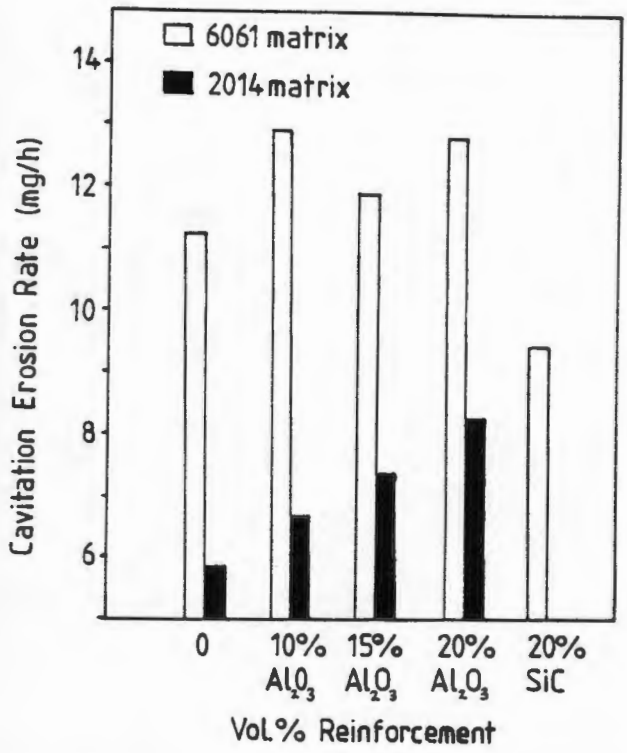

Fig.66: Bar chart showing the steady state cavitation erosion rates of the two matrix alloys and their various composites.

Scanning electron micrographs of the surface of the SiC reinforced 6061 alloy, after exposure to cavitation erosion for two, five and sixty minutes are displayed in figs.69a to 69c respectively. The same area of composite is shown for the two and five minute exposures, displaying an overall increase in plastic deformation of the matrix alloy with cavity formation at particulate interfaces and within the matrix itself. Particulates become more exposed as matrix alloy is eroded away but their integrity does not appear to be affected at this stage of the erosion process. Massive plastic deformation of the composite surface is evident after one hour of cavitation and particulates are difficult to discern from the surrounding heavily deformed alloy.

In an attempt to facilitate the examination of particulates after erosion in the steady state cavitated surface, the eroded surfaces of composites were electropolished in an 80:20 methanol/nitric acid electrolyte for 1-2 seconds, so as to remove approximately 5μm of deformed matrix alloy and expose the reinforcement. The micrograph in fig.70a shows the surface of the 20 vol.% Al_2O_3 reinforced 2014 alloy after it has been exposed to cavitation erosion for about one hour, followed by electropolishing. There is some evidence of microfracture having occurred at particulate-matrix interface, where the spinel interfacial layer

has been removed. The micrograph in fig.70b is of the same sample showing an exposed alumina reinforcing particulate where it has fractured at the interface with the surrounding matrix alloy. A scanning electron micrograph showing the electropolished surface of the cavitated 6061 alloy, reinforced with 20 vol.% SiC is shown in fig.70c. There is some evidence of particulate fracture, yet this appears to be internal as opposed to the interfacial degradation observed in the alumina reinforced alloys.

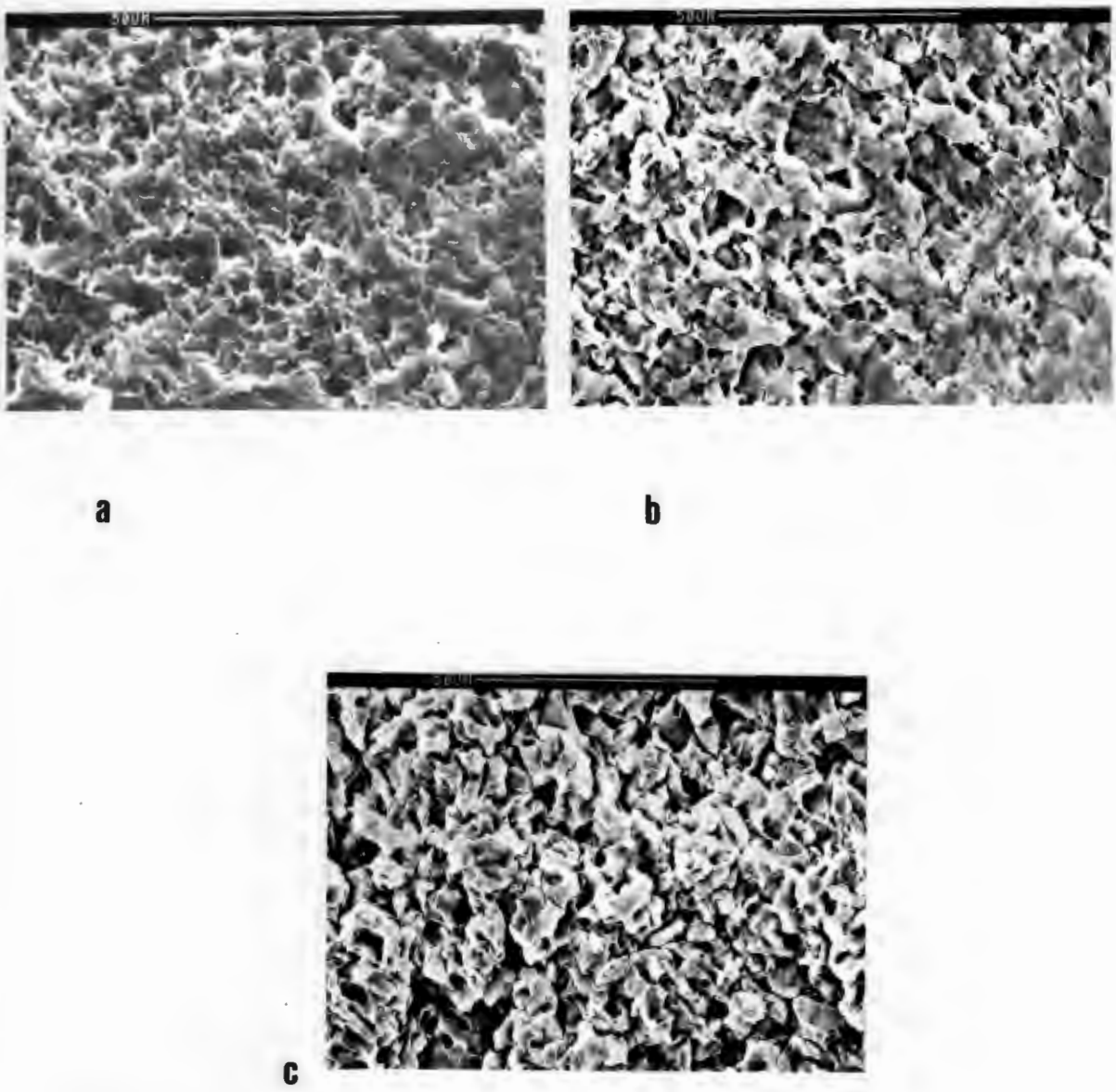

Figs.67a to 67c: Scanning electron micrographs of the cavitation eroded surface of the unreinforced 2014 alloy, after erosion periods of approximately two, five and sixty minutes respectively.

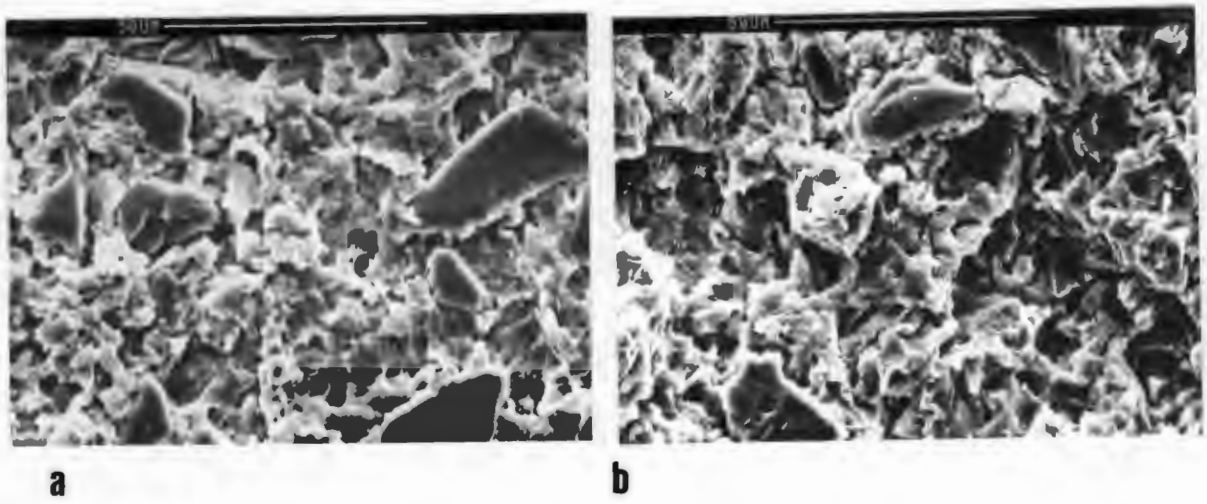

Figs.68a and 68b: Scanning electron micrographs of the 20 vol.% alumina reinforced 2014 alloy surface, after exposure to cavitating conditions of approximately five and ten minutes respectively. The matrix alloy has undergone extensive ductile deformation accompanied by intense shear at particulate interfaces.

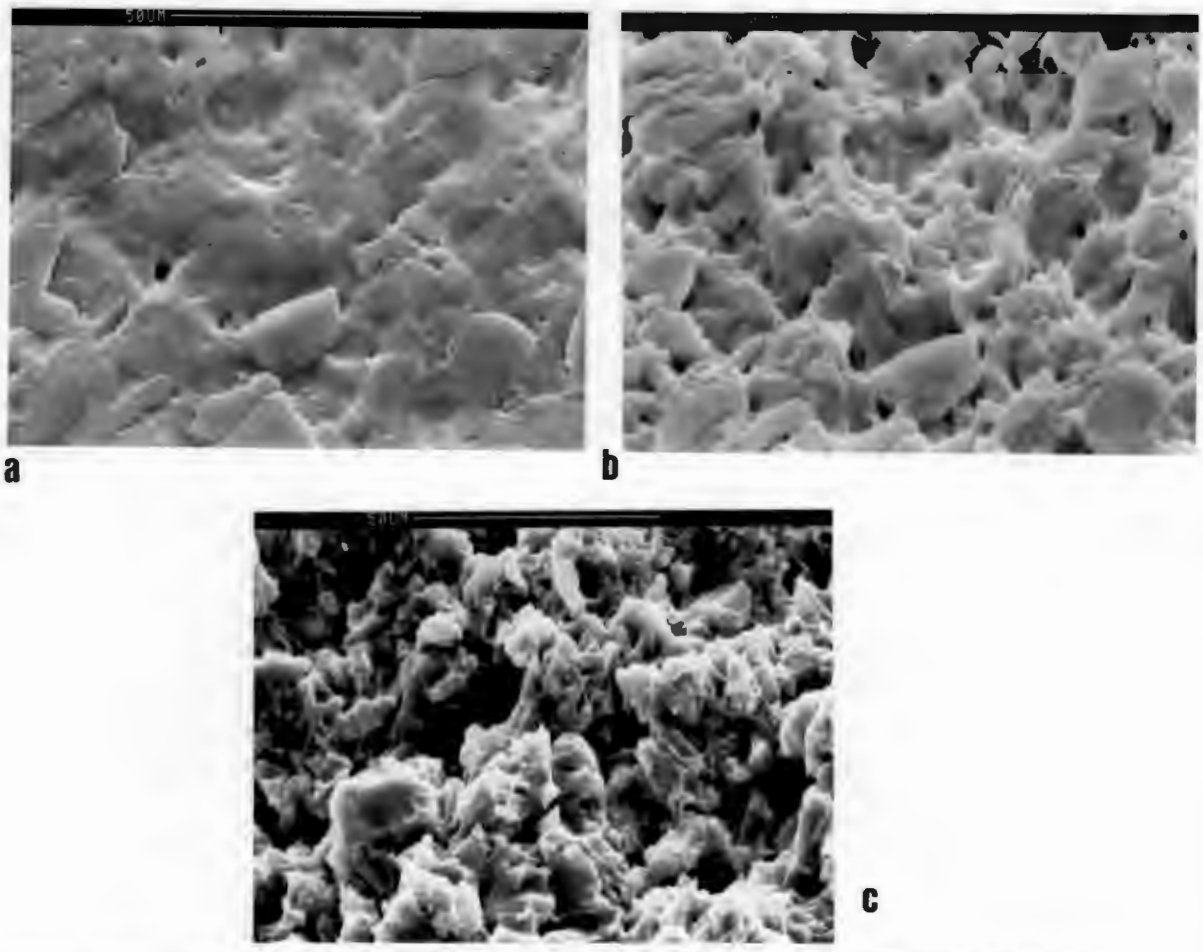

Figs.69a to 69c: Electron micrographs of the SiC reinforced 6061 alloy after exposure to cavitation erosive conditions for two, five and sixty minutes respectively. The same region of composite is shown in figs.60a and 60b.

An optical micrograph taper section (5°) of the steady state cavitated surface of the unreinforced 2014 matrix alloy is displayed in fig.71a. The section shows evidence of material removal by ductile deformation along narrow paths beneath the alloy's surface. A plot of the microhardness profile beneath the eroded surface of this alloy is depicted in fig.71b showing no appreciable subsurface hardening, even in the near surface regions. This observation is an indication that the ductile fracture process is occurring via a process of very intense shear of the alloy at the surface, with there being no appreciable accumulation of strain at greater depths.

The optical micrograph taper sections in figs.72a and 72b, show the cavitation eroded subsurface regions of the 20 vol.% SiC reinforced 6061 alloy and the 20 vol.% Al_2O_3 reinforced 2014 alloy respectively. Both micrographs display evidence of matrix ductile fracture paths 'following' and exposing the reinforcing particulates. The matrix alloy has sheared in regions extremely close to the particulate interfaces, further exposing them to the cavitating liquid. This is more noticeable in the 2014 matrix composite in fig.72b where a thin coating of matrix alloy is seen adhering to the alumina particulates with surrounding metal having been eroded away. Neither of the composites shows any evidence of extensive fracture of their reinforcing particulates in the subsurface regions.

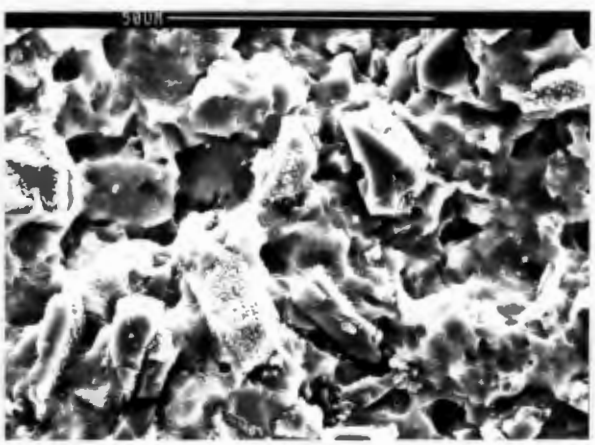

Fig.70a: Scanning electron micrograph of the 20 vol.% Al_2O_3 reinforced 2014 alloy after it has been exposed to cavitation erosion for one hour. The surface of the sample was electropolished for a few seconds, thus exposing the alumina reinforcement. Some particulates show evidence of microfracture having occurred along their interfaces, where the spinel interfacial layer has been removed.

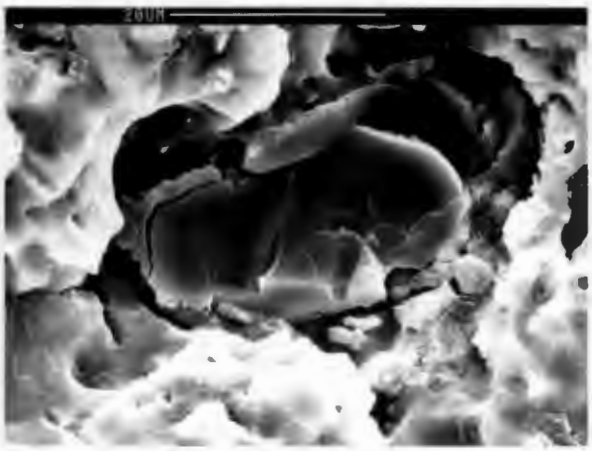

Fig.70b: Shows a scanning electron micrograph of the same composite sample in fig.70a, where a particulate has fractured along its interface after exposure to cavitation erosion.

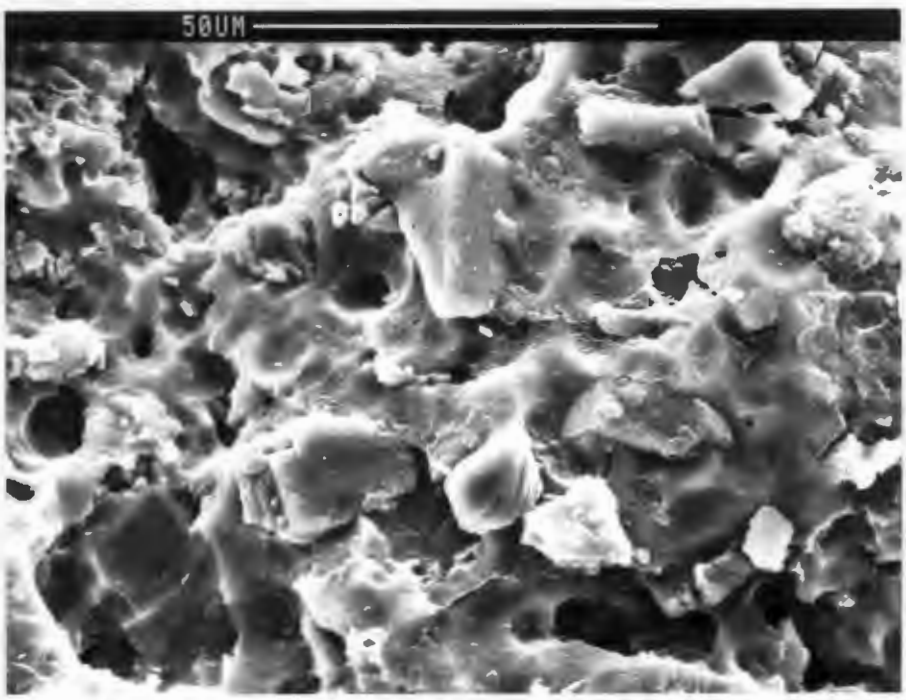

Fig.70c: A scanning electron micrograph of the 20 vol.% SiC reinforced 6061 alloy after having been subjected to cavitation erosion until steady state. The surface has been electropolished to reveal some evidence of particulate fracture and cracking. There appears to be no evidence of matrix-reinforcement interfacial failure.

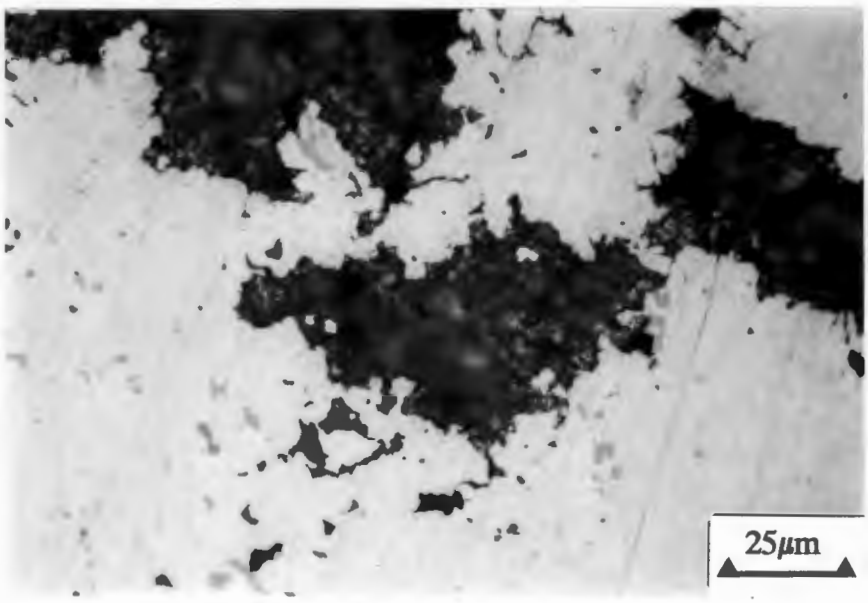

Fig.71a: Optical micrograph taper section (5°) of cavitation eroded 2014 matrix alloy, showing the extent of subsurface ductile fracture below the eroded surface.

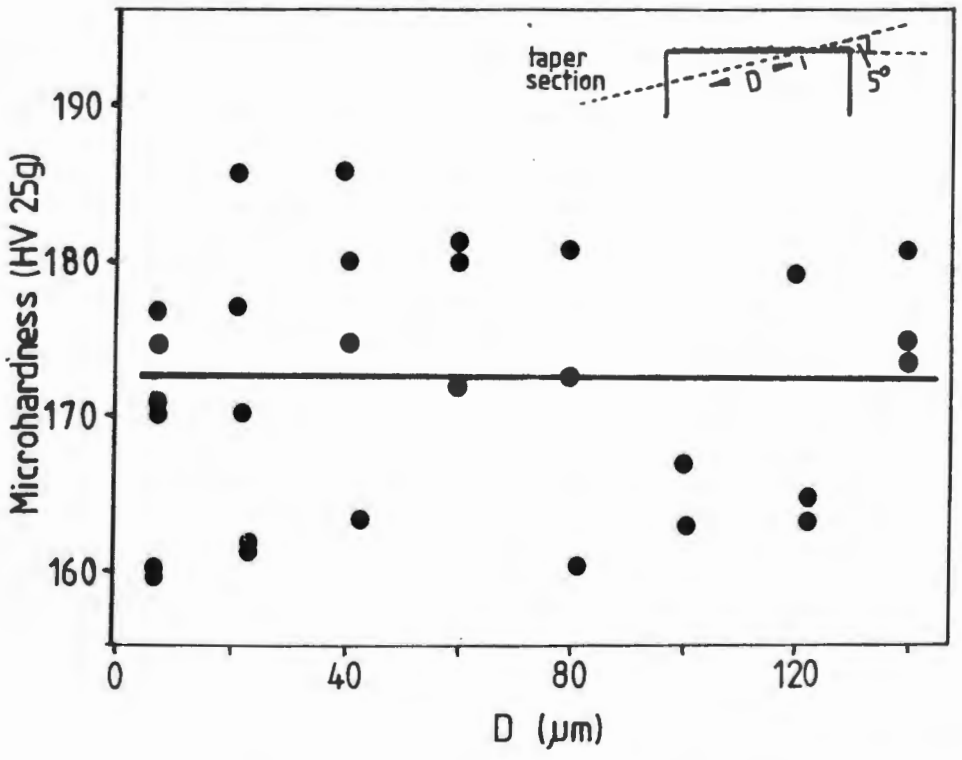

Fig.71b: Microhardness profile taken from the taper section of the eroded 2104 alloy exhibited in fig.71a. There is no evidence of any significant work hardening below the eroded surface.

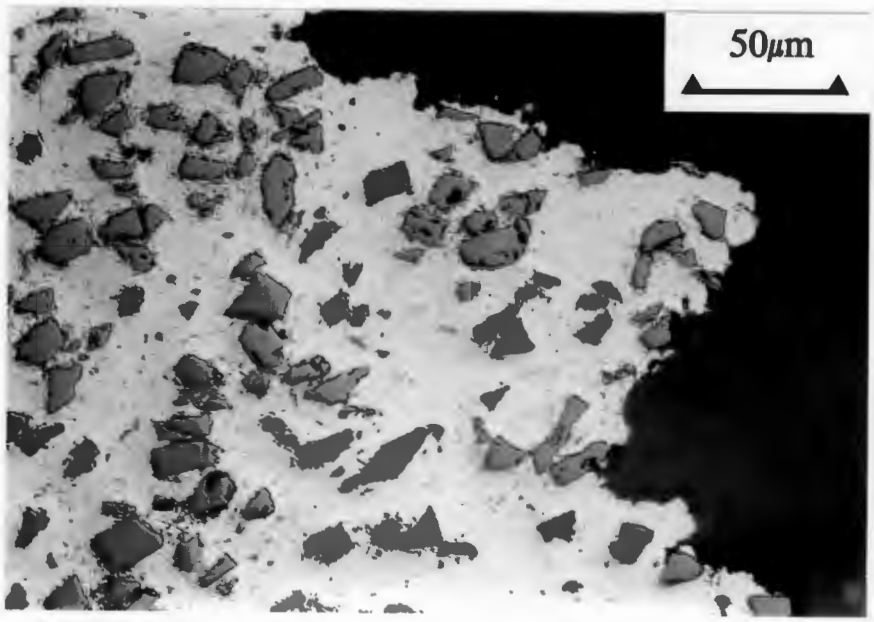

Fig.72a: Optical micrograph taper section (5°) of cavitation eroded surface of the 20 vol.% SiC reinforced 6061 alloy.

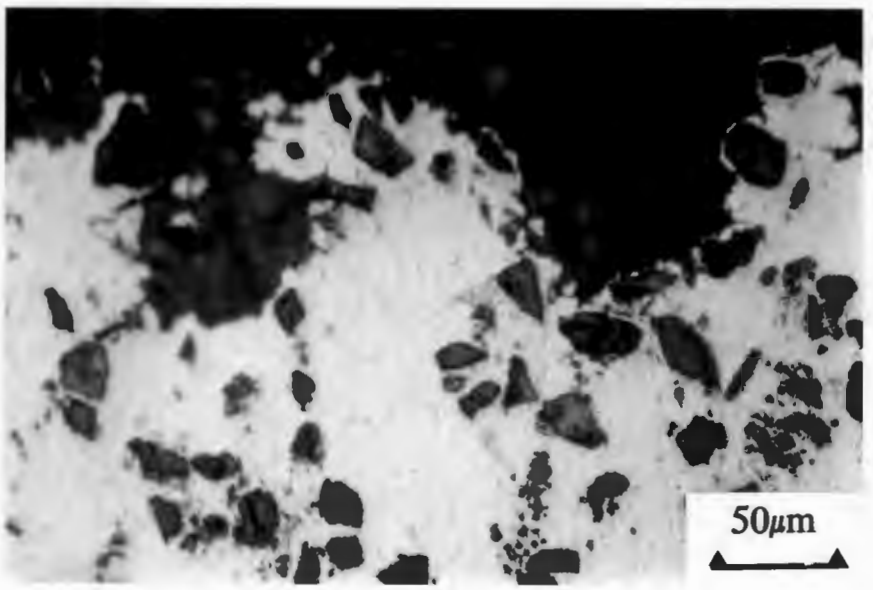

Fig.72b: Optical micrograph taper section (5°) of cavitation eroded surface of the 20 vol.% Al_2O_3 reinforced 2014 alloy. Note how the matrix alloy has sheared close to particulate interfaces.

5.0 Discussion

5.1 Tensile properties

The tensile behaviours of monolithic aluminium alloys are characterised by a period of moderate work hardening in the post-yield strain region followed by plastic instability and then rupture. Fracture surface morphology is typically "dimpled" resulting from a process of void initiation and growth from nucleation points such as intermetallics and other microdefects [117]. In each of the composites under consideration, the work hardening and fracture properties of the respective ductile matrices reinforced with ceramic particulates were altered significantly. The tensile curves of the reinforced alloys exhibited initial periods of very high work hardening, accompanied by observations of regions of intense shear deformation in the matrix alloy of post-fractured tensile specimen gauge lengths. The absence of macroscopic slip formations in the interparticulate matrix of "necking" regions of tensile specimens was particularly marked in composites containing higher volume fractions of reinforcement. The plastic accommodation of strain in these composites being highly localised and in the form of intense shear bands which were barely visible in the interparticulate matrix alloy. Intense shear bands of the type that lead to the development of ductile fracture surfaces can only develop under conditions of relatively low geometrical constraint, where the tangential component of a velocity discontinuity can greatly exceed the normal component [117]. Velocity discontinuities arise in the interparticulate matrix alloy as a result of the strong incompatibility in elastic and plastic properties between particulates and aluminium metal. Table VII summarises the disparities between the elastic and plastic properties for aluminium alloys and those of silicon carbide and alumina, together with other physical data such as thermal expansion coefficients and thermal conductivities.

Several recent experimental and numerical investigations into the deformation characteristics of discontinuously reinforced aluminium alloys [34-45] have indicated that triaxial stresses are developed within the interparticulate

	2014 Al	6061 Al	SiC	Al_2O_3
E (GPa)	74.7	69.7	400-500	300-380
Y.S. (MPa)	436	338	-	-
U.T.S. (MPa)	508	391	-	-
% Elong.	10.5	9.3	-	-
α (10^{-6}/°C)	23	23	4	8
C (J/kg/K)	900	900	628-1046	1088
σ (W/m/K)	239	239	63-270	27
MPt.(°C)	660	660	2688	2046

Table VII: Summary of the Young's moduli (E), 0.1% yield stress (Y.S.), ultimate tensile stress (U.T.S.), ductility (% Elong.), thermal expansion coefficients (α), specific heat capacities (C), thermal conductivities (σ) and melting points of silicon carbide, alumina and aluminium alloys.

matrix alloy during tensile straining. The composite matrix is constrained from plastic flow by the reinforcement interfaces and the hydrostatic nature of the stresses developed are sufficient to inhibit any yielding and void growth phenomena [35,41]. In composites containing higher volume fractions of reinforcement, the levels of triaxial stress are sufficient to initiate fracture in the ceramic reinforcement [36,44,45]. The matrix alloy is initially constrained from deformation by the reinforcing particulate interfaces in the early stages of strain accommodation. Large triaxial stresses are generated in the matrix arising from constraint effects; the yield stress of the matrix alloy is raised as a result of the elastic transfer of stress from the more compliant to the stiffer phase [31], thereby introducing a pseudo-elastic or 'brittle' type behaviour in the matrix. Eventually, the release of strain energy can occur via a combination of several relaxation mechanisms namely, microvoid nucleation, coalescence and growth, particulate fracture at high levels of matrix hydrostatic stress, microyielding in regions of lower matrix constraint and failure of matrix-particulate interfaces. These strain energy releasing mechanisms result in

lower levels of geometric constraint in matrix regions, which are conducive to the onset of shear type deformation phenomena. The intensity of the shear occurring in the interparticulate matrix alloy would be dependant on the magnitude of the hydrostatic stresses developed, or 'brittleness' of the matrix alloy before the occurrence of ductile deformation at velocity discontinuities. In this regard, the composites with the high yield strength 2014 matrix alloy as matrix and the 6061 alloys containing large volume fractions of reinforcement, each display intense shear phenomena in their post-fractured gauge lengths, examples of which are displayed in figs.14 and 15. High work hardening rates arise in these composites as a result of the rapid release of large amounts of strain energy, producing the high velocity motion of dislocations and initiating the nucleation, growth and coalescence of microvoids in localised regions of intense shear, followed by ductile fracture.

Particulate fracture is also found to occur in localised regions of high particulate density in the matrix alloy (clusters). The release of strain energy during tensile overload occurring when the ceramic particulates fracture, resulting in localised rapid strain hardening, intense shear and tearing of the matrix alloy adjacent to the cracked particulates. Eventual failure of the composite occurs through linkage of torn matrix "cavities" situated around broken particulates accompanied by intensive shear deformation near particulate interfaces. Further support for these failure modes are observed in the tensile overload fracture surface morphologies of the composites presented in figs.16-18. Each reinforced alloy exhibited particulate fracture in the plane normal to the tensile axis. The fracture surfaces of the alloys containing 15 vol.% and 20 vol.% reinforcement, showed widespread particulate cleavage associated with extensive matrix tearing to form "tear ridges" [39] and cavities surrounding each broken particulate. The composites containing 10 vol.% of reinforcement had fracture surfaces showing particulate failure and matrix tearing, together with widespread dimple formation associated with the release of strain energy by void nucleation and growth, in the less constrained regions of matrix containing low densities of reinforcing particles. The composites containing higher volume fractions of reinforcement showed similar evidence of dimple formation in isolated regions on their fracture surfaces; attributable to the release of strain energy in areas of low particulate density, accompanied by regions of intense

matrix shear close to particulate interfaces. The fracture surface of the 2014 alloy reinforced with 20 vol.% alumina in fig.17, displays widespread particulate fracture, interfacial decohesion and intense ductile shear of the matrix alloy near interfaces. The observed fracture phenomena occur as a result of the rapid relaxation of large levels of geometric constraint and triaxial stress within the high strength matrix. Both the greater volume fraction and size (27μm diameter) of the reinforcing particulates in this composite, are conducive to generating very large amounts of constraint and triaxiality.

The stress-strain response of each of the reinforced alloys is determined predominantly by the volume fraction of ceramic particulates present in the ductile matrices. With larger volume fractions of high modulus particulates, there is a buildup of constraint within the matrix resulting in a more efficient transfer of load to the reinforcement. Strain energy is thus accumulated, and liberated, in a more elastic fashion by the added ceramic reinforcement, resulting in lower plastic strains during tensile overload.

The strength of each base matrix alloy appears to have an influence on the stress-strain response of each reinforced system. The high strength and ductility of the 2014 alloy is compromised with the addition of alumina reinforcement, showing similar behaviour to the tensile tests conducted by McDanels [16], who also obtained drops in strength and ductility with the use of high strength matrices. Thus it can be inferred that the magnitude of the stresses developed in the early stages of strain hardening in the interparticulate matrix alloy of each composite, are of the same order of magnitude of those required to initiate fracture in the alumina reinforcement.

The weaker and less ductile 6061 matrix alloy undergoes moderate to significant strengthening effects with the addition of alumina particulates, showing proportionately higher plastic extensions in comparison to the 2014 alloys reinforced with the same volume fraction of particulates. It is evident that the 6061 matrix composites require additional straining and plastic work in order to generate matrix triaxial stresses sufficient to initiate fracture in the alumina reinforcement. The plausibility of this argument is improved when considering the behaviour of the 6061

alloy reinforced by the harder, tougher and stiffer silicon carbide particulates [81,118]. There is a larger elastic misfit between silicon carbide and the aluminium matrix, as compared to that obtained between alumina and aluminium, due to the fact that silicon carbide has a larger average elastic modulus (Table VII). During plastic deformation the matrix transfers stress to the elastically distorted inclusions. Elastic distortion strains in a high stiffness silicon carbide inclusion would be below those found in an alumina inclusion at equivalent external stress levels. Thus the matrix surrounding the silicon carbide particulates is subjected to a higher level of constraint and therefore has a higher yield stress, compared to the matrix alloy surrounding alumina particulate inclusions. The extra strain energy required to initiate fracture in the silicon carbide particulates in the 20 vol.% SiC reinforced 6061 alloy, is achieved by the additional work-hardening and consequent strength increment of the SiC composite as compared to the alumina reinforced matrices.

A measure of the strain energy required to initiate fracture in the composites and their respective matrix alloys, is reflected in their work to fracture values ($E_{fracture}$) displayed in fig.73 and Table IV. The $E_{fracture}$ values were determined by measuring the area beneath each material's stress-strain curve. The 2014 matrix alloy shows a higher work to fracture as it is harder than the 6061 alloy and thus cannot be strengthened very much by the addition of reinforcement, prior to the initiation of void growth and ductile fracture. The 6061 alloy is a softer, tougher matrix and undergoes a relatively greater degree of hardening with the addition of particulates before fracture processes occur. Thus all the 6061 matrix composites show proportionately higher $E_{fracture}$ measurements than their 2014 matrix alloy counterparts of equivalent reinforcement content. This occurs as a result of the additional plastic work required to initiate fracture in the 6061 composites, whereas the 2104 composites require relatively little plastic work for void initiation and reinforcement damage. The high matrix - inclusion elastic misfit and resultant increased matrix yield stress, are the most probable reasons explaining the slightly greater work to fracture in the silicon carbide reinforced 6061 alloy, compared to its 6061 matrix counterpart containing 20 vol.% alumina.

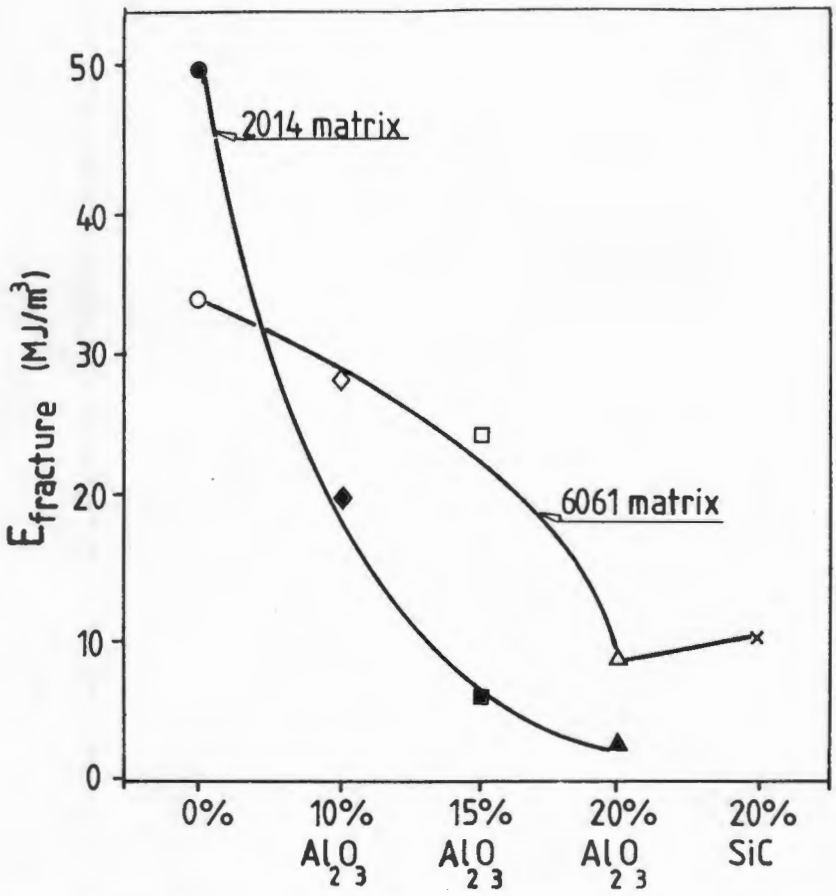

Fig.73: The work to fracture values ($E_{fracture}$) of each composite and monolithic alloy are plotted as a function of their respective reinforcement contents. The work to fracture terms were calculated from the total area beneath each material's tensile curve (figs.12 and 13).

The rationale behind characterising the mechanical properties of the reinforced and unreinforced aluminium alloys was to facilitate the interpretation of their behaviour in various tribological situations. While the stresses imparted to a material as it rubs, abrades or impacts against another are often more complex in nature than those developed in a simple uniaxial tensile test, it is hoped nevertheless, that the current assessment of mechanical response will contribute towards predicting and interpreting the tribological behaviour. In addition, fracture in tension can depend strongly on notches and surface defects. The strain to fracture values obtained in the current investigation, were similar to manufacturing specifications listed for 2014 and 6061 (T6) alloy composites by *Duralcan* [135]. Strain to fracture values for alumina reinforced 6061 (T6) matrix composites are listed by *Duralcan* as follows: 10% alumina - 7.6% el., 15% alumina - 5.4% el., 20% alumina - 2.1%. Strain to

fracture values for 2014 (T6) matrix composites are listed by Duralcan as: 10% alumina - 3.3% el., 15% alumina - 2.3% el., 20% alumina - 0.9% el.

The majority of tribological environments involve situations where a hard body indents, impinges or slides against another softer surface. In this regard, the hardness, work hardening ability and the magnitude of the strain to fracture of each material involved in the mechanical interaction, are important factors which determine the degree and depth to which strain accumulates below each surface prior to microfracture and wear loss. Furthermore, the magnitude of the stresses as well as the rate at which strain energy is imparted and dissipated between two bodies as they interact, also determines the respective levels of subsurface strain accumulation and fracture.

5.2 Abrasion

Each of the unreinforced aluminium matrix alloys display abrasive wear modes that are typical of those found for ductile metals; extensive plastic deformation and cutting of the aluminium is evident, together with lower wear rates for the harder 2014 aluminium alloy. All of the reinforced aluminium alloys display two body abrasion resistances that are greater than those of their respective matrix alloys, in both high and low contact stress abrading conditions. The interaction between reinforcing particulates on the surface of each composite and abrasive particles, results in the generation of stresses at asperity contact points which are sufficient to initiate damage in the ceramic reinforcement. The extent of particulate damage depends on the magnitude of these contact stresses as well as the toughness and hardness of both the reinforcing ceramics and abrasive particles. When each composite is abraded against the coarsest abrasive, the reinforcing particulates fracture as a result of the large stresses present at asperity contact points. Surface morphologies of each worn composite correlate well with observations made by other researchers using coarse abrasives against a variety of aluminium matrix composites [7,10,56]; the common characteristic features of high contact stress abrasion involve widespread particulate or fibre fracture, accompanied by extensive

plastic indentation, plastic deformation, and cutting of the matrix alloy.

The use of finer abrasives is associated with a larger number of asperity contact points per unit area and thus lower average contact stresses. Abrasive particles are unable to indent the composite surfaces and damage to the ceramic reinforcement is restricted to microfracture with very little evidence of catastrophic failure. Thus the indentation stresses during abrasion by fine abrasives are so low that little plastic deformation is caused on each pass. The onset of the transition from general reinforcement fracture and fragmentation, to low stress abrasion where the integrity of the ceramic inclusions is maintained, is associated with the use of the 600 grit abrasive grit particles (see figs.25 and 26) that are approximately 16μm in diameter. Similar values were obtained by Wang and Hutchings [7] for alumina fibre reinforced 6061 alloys, where abrasive particle sizes of between 20-28μm no longer fractured the reinforcing fibres.

The worn surfaces of each composite are covered with large abrasive wear tracks whose size generally exceeds that of the microstructural constituents of each reinforced alloy. This appears to be the case particularly when the materials are abraded against coarse grit abrasives (see figs. 25a and 26a), yet even when they are worn against the finest grit abrasive, the magnitude of the observed wear tracks is generally bigger than interparticulate distances (approximately 10-20μm). Thus the indenting abrasive particles 'see' the average or bulk composite microstructure during abrasion. The amounts of material displaced and removed as an abrasive particle indents the surface of a composite would therefore be dependant on the level to which its microstructure is able to resist plastic deformation by indentation. Resistance to plastic indentation and deformation in the reinforced alloys is governed primarily by the level of constraint introduced into interparticulate matrix regions by the high modulus inclusions. Large volume fractions of ceramic reinforcement introduce greater levels of matrix constraint, effecting an overall increase in matrix yield and therefore hardness and improved wear resistance.

Each material's resistance to indentation appears to be the dominant factor in determining abrasion resistance under both high and low contact stress conditions. This is further illustrated by fig.74 which shows a plot of abrasion rates of each

reinforced and unreinforced alloy as a function of their respective bulk hardness values. Wear rates for abrasion against both the coarsest and finest abrasives are shown; they exhibit a general decrease in abrasion rate with increase in each composite's bulk hardness. Apart from the improved wear resistance of each composite when worn against finer grit sized abrasives, some alloys which have similar hardnesses display different abrasion resistances when they are worn against the same abrasive grit size. eg. the 20 vol% SiC reinforced 6061 alloy (159 HV) and the 10 vol.% Al_2O_3 reinforced 2014 alloy (162 HV). Thus it becomes apparent that the bulk hardness of each composite is not the only determinant of abrasion resistance and that other properties of both matrix and particulates, such as toughness and strain to fracture, possibly play an important function.

The importance of the type of reinforcement used in each composite, in determining wear behaviour, is illustrated when the silicon carbide reinforced 6061 alloy is compared to the other alumina reinforced alloys. Despite the bulk hardness of the silicon carbide composite being lower than that of the 2014 alloy composites, this material shows a higher wear resistance under both high and low contact stress abrasive environments. It is evident that the greater toughness, hardness and compatibility of the higher modulus silicon carbide particulates to plastic strain, are primarily responsible for improved resistance to indentation deformation and fracture during abrasion. Typical Knoop Hardness values of sintered silicon carbides lie in the range 2500-2800 $kgmm^{-2}$, with fracture toughnesses between 3 and 5 $MNm^{-3/2}$ [118]. High density alumina (3.98 gcm^{-3}) on the other hand has a hardness in the region of 1800 HV and fracture toughness of 2.9 $MNm^{-3/2}$ [81]. The current tensile testing investigations have established that silicon carbide reinforcement was able to withstand greater stresses than alumina reinforcement, before eventual catastrophic failure. The greater compatibility of the higher modulus silicon carbide to strain transfer from the plastically deforming matrix alloy, makes removal of the 6061 alloy more energy intensive than that found in the alumina reinforced composites. Removal of the 6061 matrix alloy is thus prevented by the additional constraint afforded by the tougher, harder and elastically more compatible silicon carbide particulates which retain their integrity to a greater extent when compared to the alumina reinforcement in similar abrasive situations.

Another factor which plays an important role in the wear behaviour of each reinforced alloy, is that of the hardness of the abrasive particles against which the composite is loaded. The aluminium oxide abrasive particles are themselves abraded by the alumina and silicon carbide reinforcing particulates present in the aluminium alloys. A situation is reached where aluminium oxide abrasive particles and ceramic reinforcing particulates are involved in a process of mutual microfracture as they move across each other. The silicon carbide reinforcement present in the 20 vol.% 6061 alloy, is able to indent the softer abrading particles resulting in very low wear rates for this composite.

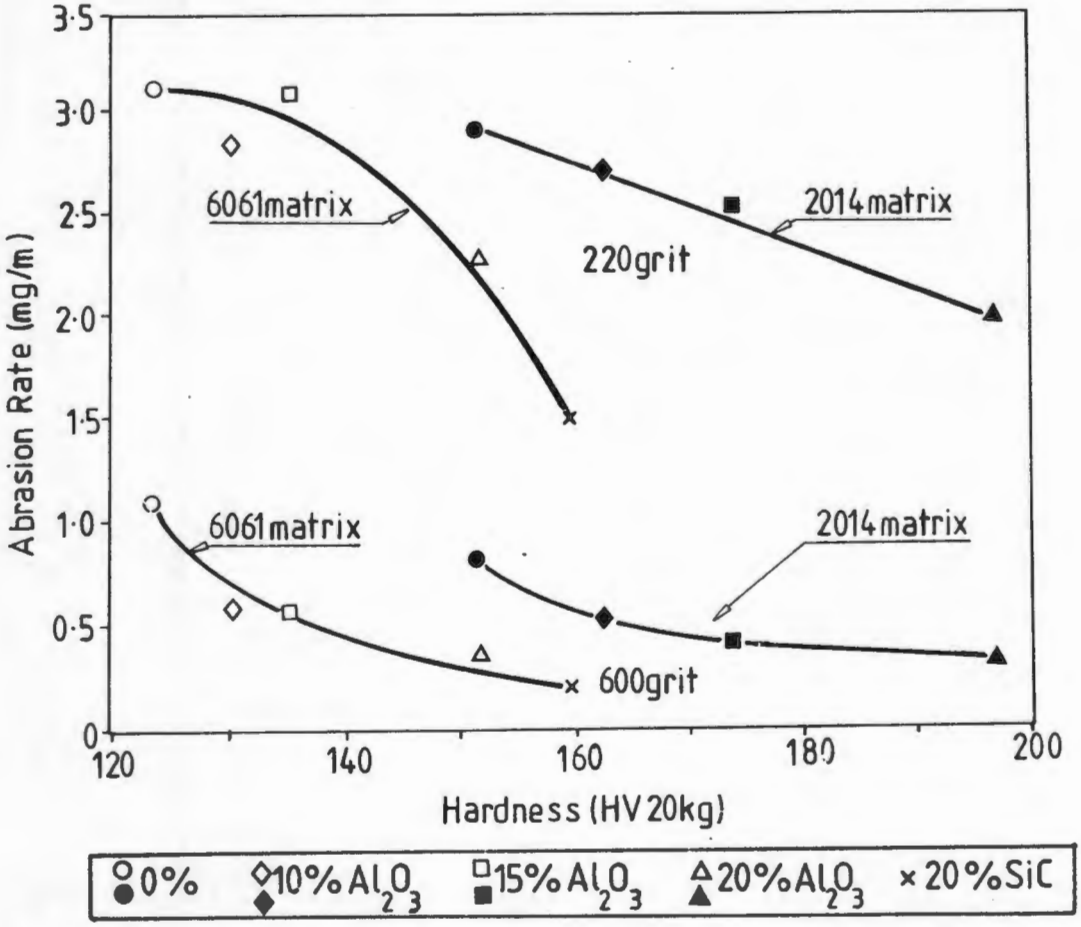

Fig.74: Abrasion rates of each reinforced and unreinforced alloy, plotted as a function of their respective macrohardness (HV_{20kg}) values. The wear rates are those for abrasion against the coarsest (220 grit) and finest (600 grit) alumina abrasives.

By taking into account the excellent abrasion resistance of the silicon carbide reinforced alloy, when it is abraded against an abrasive which is softer than silicon

carbide, it can be inferred that the use of softer abrasives (eg. silica), will result in even better wear resistances for all the composites.

The effect of using an abrasive that is harder than alumina, such as silicon carbide results in a distinct decrease in abrasion resistance of the composites, relative to their matrix alloys (see fig.27). The alumina reinforced alloys deteriorate in abrasion resistance to levels similar or below those of their matrix alloy, whereas the silicon carbide reinforced alloy shows a moderate reduction in relative wear resistance from 2.08 to 1.47. The low wear resistances obtained for the alloys containing alumina reinforcement, are an indication that increased microfracture of the softer alumina inclusions is occurring when they are indented by the silicon carbide abrasive particles. The 6061 alloy reinforced with silicon carbide is able to resist microfracture of its reinforcing inclusions due to their similarity in hardness with the silicon carbide abrasive. Silicon carbide also has an improved fracture toughness and elastic compatibility to its deforming matrix, as compared to alumina.

The influence that reinforcing particulate size has over abrasion resistance is best illustrated by focussing on the behaviour of the softer alumina reinforced 6061 alloys. The 20 vol.% Al_2O_3 reinforced alloy has a wear resistance which outperforms that of the harder 2014 alloy containing 15 vol.% alumina, in both high and low stress abrasion. A possible explanation for such behaviour may be associated with the large average diameter of this composite's reinforcing inclusions (32.2μm), which are approximately twice the size of the alumina particulates in the 10% and 15% reinforced 6061 and 2014 alloys. Thus, an abrading particle has to indent the surface of the 20 vol.% Al_2O_3 6061 alloy to a proportionately greater depth than that of the other composites in order to effect the same degree of damage to the larger particulates. Bigger reinforcing particulates would also require greater amounts of kinetic energy to be transferred during abrasion, in order to initiate their fracture and removal. The matrix alloy is also more constrained from plastic deformation and removal by the larger particulate size.

The 10 vol.% and 15 vol.% alumina reinforced 6061 alloys have similar particulate sizes (14.1μm and 15.1μm respectively) and are able to accommodate strain energy in a more plastic fashion compared to the harder 20 vol.% alumina reinforced 6061

alloy. Indentation depths in these two composites are more likely to exceed the diameters of their respective reinforcing particulates under high contact stress abrasion, increasing the likelihood of particulate fracture and greater material removal rates. The relatively small difference in bulk hardness between these two composites (130.4 and 135.3 HV respectively) indicates that the depth of subsurface deformation during high contact stress abrasion is similar. Material removal rates can then be rationalised in terms of the difference in ductility between the two composites. The matrix of the 15 vol.% alumina reinforced 6061 composite is under greater constraint and therefore has a lower ductility compared to the 10 vol.% alumina reinforced alloy. Microfracture processes would thus occur at lower plastic strains in the composite containing more reinforcement, resulting in the observed larger rates of material removal for the 15 vol.% reinforced alloy. The transition to low contact stress abrasion results in the 15 vol.% reinforced alloy having a marginally lower wear rate compared to the 10 vol.% composite. Indentation depths are reduced in this instance and there is less chance of bulk microfracture occuring in either of the composites. The effect of reinforcing particulate size is not evident in the abrasion behaviour of the 2014 matrix alloy composites, despite their having similar particulate sizes to their reinforced 6061 matrix alloy counterparts. This can be explained by taking into account the greater hardness of the 2014 matrix alloy, where indentation depths are reduced resulting in less catastrophic fracture and removal of particulates from the harder matrix.

5.3 Reciprocating Sliding Wear

A common feature of the interaction between aluminium and steel, as they come into sliding contact, is the rapid formation of a transfer layer of aluminium on the steel surface [68-70]. During steady state wear a situation develops where the aluminium alloy eventually ends up sliding against its own transfer layer, with friction coefficients approaching those measured for the aluminium alloy sliding against itself. Large shear stresses are developed at the sliding interface, with the rate of material removal from an aluminium alloy surface being largely dependant on its resistance to shear.

The steady state sliding wear behaviour of the two unreinforced aluminium alloys, is characterised by high wear rates and transfer of the aluminium to the stainless steel counterfaces. Of the two alloys, the harder and stronger 2014 monolith displays a steady state wear rate that is approximately ten times below that of the 6061 alloy. The stronger alloy is clearly more resistant to shear as is evident by the steep strain gradient in its subsurface wear zone (fig.42), accompanied by markedly less transfer to the counterface surface. The reciprocating nature of the sliding wear tests make it difficult for quantitative comparisons of subsurface strain gradients to be made. Thus, the depth to which there is plastic strain accommodation is perhaps a suitable alternative indication of each alloys ability to resist deformation by shear. In comparison to the 2014 alloy, the weaker 6061 alloy is less resistant to deformation, showing strain accumulation to depths of 100-150μm below its worn surface. The examination of the counterface which had been worn to steady state by the 6061 alloy, displayed a large amount of transferred aluminium and a preponderance of big flakes of the alloy adhering to its surface.

The permanent bending of grains in the subsurface region of the 2014 alloy slider, despite the reciprocating motion during wear tests, may be attributable to localised work-hardening in the initial pass of slider over the counterface; further reciprocating cycles producing incremental increases in plastic strain of the deformed grains, without shearing them in the opposite direction. Similar findings were made by Caldwell and Wert [119] in reciprocating slider tests on Cu-Al alloys where initial permanent bending of grain boundaries was a precursor to further strain accommodation by pronounced slip and lattice rotation. The absence of any significant permanent directionality in subsurface slip in the 6061 alloy (see fig.41) can probably be attributed to its lower work-hardening behaviour compared to the 2014 alloy. This is evidenced in the subsurface microhardness profiles displayed in fig.43 where no significant hardening occurs in the wear zone of the 6061 alloy, despite a preponderance of slip lines being observed. The weaker 6061 alloy does not work-harden and is therefore more susceptible to shear deformation in the subsurface regions. The low shear resistance of this alloy allows for greater amounts of transfer in the form of large flakes of aluminium wear debris (see fig.31) and high wear rates.

The sliding wear rates of each aluminium alloy reinforced with ceramic particulates are almost three orders of magnitude below those of their respective unreinforced alloys. The incorporation of particulate reinforcement into each alloy has resulted in a lowering of the adhesive transfer rate of aluminium to the stainless steel surfaces. Similar reductions in aluminium transfer to steel counterfaces, have been reported by several other investigators [57,61,63,64]. By increasing the volume fraction of ceramic particulates in each alloy, the surface area of matrix alloy that comes into contact with the counterface is reduced as the particulates themselves become load bearing, resulting in a reduction in the rate of aluminium to steel transfer. The tensile test investigations conducted on each composite, have recorded that plastic flow of the matrix alloy of each composite is inhibited by the constraints imposed by the particulates during tensile straining. Similar effects can be expected at the sliding wear interface, where plastic flow of the interparticulate matrix alloy, arising from frictional shear stresses generated at the composite sliding surface, would be prevented depending on the level of plastic constraint in the matrix. Thus, the probability of shear failure in the aluminium matrix is diminished by the reduced ability of the composite to accommodate strain by plastic slip and lowering the probability of transfer to the steel counterface. In this regard, the 6061 composites show moderate reductions in steady state wear as the volume fraction of reinforcement is increased. The 2014 composites display approximately equal wear rates, apart from the 20 vol.% Al_2O_3 alloy which exhibits both high and low wear losses. The 10 vol.% 6061 alloy shows the greatest wear rate of all the composites (besides the 20 vol.% Al_2O_3 2014 composite) which is in accordance with its proportionately higher surface area of matrix alloy in contact with the counterface, and increased susceptibility to localised shear failure afforded by the lack of significant matrix protection by the reinforcing particulates. This is further corroborated by the existence of patchy areas of transferred aluminium alloy on the counterface surface, against which the composite was worn. The sliding wear rates of the 2014 alloys reinforced with 10 vol.% and 15 vol.% alumina, and the steady state low wear regime of the alloy containing 20 vol.% alumina, are significantly below those of their 6061 counterparts due to the greater shear strength of the 2014 matrix.

When the sliding wear behaviour of each material is considered on a strength or hardness basis, it is clear that the modest variations in hardness and strength afforded by the presence of the reinforcing particulates, are unable to account for the observed dramatic improvements in wear resistance. In addition, there exists a disparity between the respective tensile work to fracture ($E_{fracture}$) terms of the monolithic alloys (fig.73) and those of the composites, when compared to their respective wear rates. Both monolithic alloys require large amounts of plastic work to initiate the formation of a new surface during tensile straining. The high wear rates and production of large debris flakes (50 - 200μm) during reciprocating sliding wear of the aluminium alloys are indicative of high wear energies. In recent work by Rosenfield [120] on the fracture mechanics of wear, it was found that wear energies are generally very high compared to tensile energies. The creation of a new surface by wear requires considerably more energy than does creation of a new surface by tensile loading of a large crack. In the current investigation the reinforced alloys display marked reductions in wear rate of several orders of magnitude, yet exhibit moderate reductions in tensile energy when compared to the monolithic alloys. A probable explanation for these observations could be attributed to the constraining effects of reinforcing particulates which prevent the onset of shear deformation arising in the interparticulate matrix alloy during sliding wear. There exists a dramatic improvement in sliding wear resistance due to an overall change in wear mode. This change in wear mode is accompanied by an increased resistance to shear, shear instabilities, and most probably adiabatic shear, arising in the interparticulate matrix aluminium at the sliding interface.

Each of the stainless steel counterfaces displayed steady state wear rates during sliding contact with the reinforced alloys. The wear mode for all the counterfaces is distinctively abrasive, indicating that the ceramic reinforcing particulates abrade and initiate the transfer of steel debris to the sliding surfaces of each composite. Evidence from the subsurface taper section in fig32a together with the worn surfaces of composites in figs.36 and 39 and their associated Fe-Xray maps, confirm that there is significant transfer and embedding of counterface debris into the worn surfaces of both the alumina and silicon carbide reinforced alloys.

The counterfaces worn by the 10 vol.% and 15 vol.% alumina reinforced 2014

matrix alloys, display lower wear rates compared to those worn by the alumina reinforced 6061 alloys (see figs.28 and 29). This is most probably attributable to the greater shear strength of the 2014 matrix, which would reduce chances of decohesion and transfer of mechanically mixed aluminium matrix and steel debris between the two sliding surfaces, thus preventing further exposure of reinforcing particulates to the counterface. Each of the 6061 and 2014 composites, including the low-wear regime of the 20 vol.% Al_2O_3 2014 composite, display counterface wear rates which show a slight decrease with increase in volume fraction of reinforcement. The decrease in wear rate, although minor, can be attributed to the higher number of reinforcing particulates per unit area, in contact with the counterface and resultant lower contact stresses. However, once a significant steady-state transfer layer has been formed, the contact stresses would be markedly reduced. Of greater influence perhaps, is the ease with which interparticulate matrix alloy and transfer layer material is able to be back-transferred to the counterface, thereby exposing the ceramic particulates to the counterface and initiating further abrasion.

The lowest counterface wear rate is displayed during wear against the silicon carbide reinforced 6061 alloy as is shown in fig.28. Silicon carbide, being both harder and tougher than alumina, is better able to resist fracture when exposed to the counterface during sliding. Previous research involving sliding contact between ceramic matrix composites and steels [121,122], and aluminium matrix composites and steels [11], has reported the preferential transfer of steel to alumina surfaces as opposed to carbide or nitride reinforcements. The preferred adhesion of steel to alumina has been attributed to the strong adhesive bond formed between the oxide ceramics and ferrous metals. There is little chemical affinity between carbide type ceramics and ferrous metals at very low sliding speeds and in vacuum [123]. However, at higher sliding speeds and temperatures there would be an expected high affinity and good adhesion between ferrous and carbide materials, producing an Fe_3C interfacial compound. Despite these considerations, it could equally be argued that the increased susceptibility of alumina to fracture would expose the counterface to additional abrasion by particulate fragments acting as third bodies in the sliding process. The silicon carbide particulates are harder and more tough compared to alumina inclusions, and therefore don't fragment as easily; thus

retaining their integrity and providing improved load bearing capacity as protective 'studs' in the matrix alloy.

The microfracture of reinforcement, particularly the alumina, results in fragments becoming incorporated into the transfer layer, causing yet further abrasion during the transfer and back-transfer dynamic situation that ensues during steady-state sliding. The dynamic transfer process can be likened to a third body abrasive wear situation, where the transfer layer of ceramic, steel and aluminium debris acts as a type of abrasive 'slurry' at the sliding interface. This situation is illustrated schematically in fig.75, showing an alumina reinforced alloy sliding against a steel counterface.

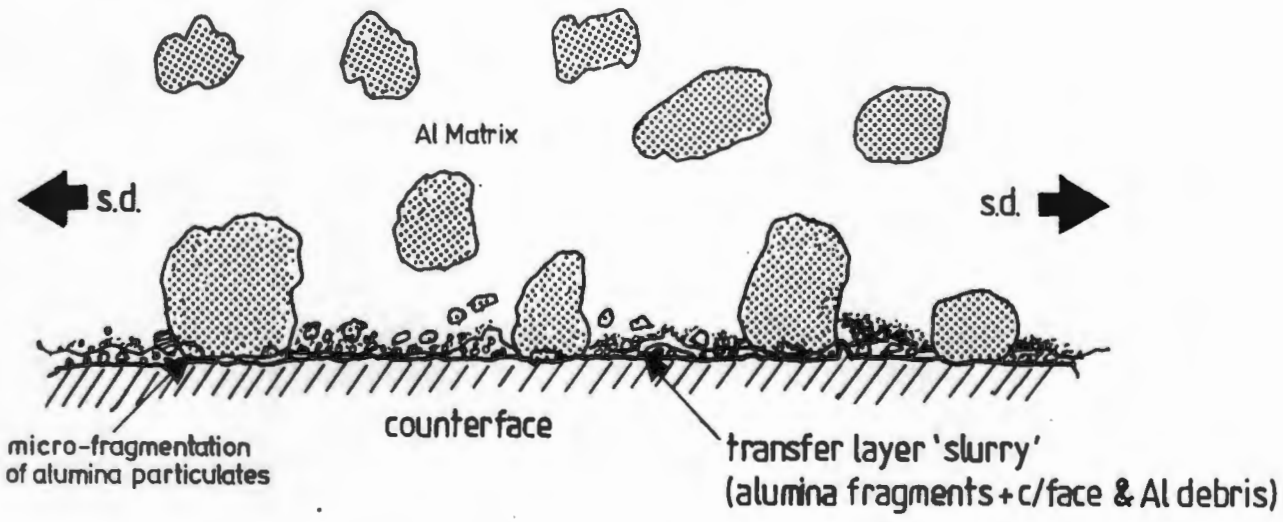

Fig.75: Schematic diagram of the wear processes at the sliding interface between an alumina particulate reinforced alloy and a steel counterface. The dynamic transfer process during steady state wear can be likened to a third body abrasive wear situation, where the transfer layer of alumina fragments, steel and aluminium debris acts as a 'slurry' at the sliding interface.

Breakage and microfracture of alumina reinforcing particulates would also render their surfaces more susceptible to mechanical interlocking with steel asperities, thereby increasing counterface wear. This argument is corroborated by the observation that less counterface and particulate debris entrainment is visible in the worn surface of the composite reinforced by the more fracture resistant silicon carbide (fig.38), when compared to those of the alumina reinforced alloys shown in figs.35,36 and 39.

The large counterface wear of the 2014 alloy reinforced with 20 vol.% alumina (see fig.29) represents an anomaly, in that reduced loads per reinforcing particulate are expected, resulting in less fragmentation and wear. A probable explanation for this behaviour may be attributed to the inability of the interparticulate matrix alloy to withstand the high triaxial stresses developed at the wear interface, resulting in fracture at low strains. This argument is developed more fully, later in this section of the chapter.

Further evidence for alumina fragmentation and incorporation into the transfer layer is found in the transmission electron microscope investigations of the wear transfer layer of the 20 vol.% Al_2O_3 6061 composite. Selected area Debye-Scherrer ring patterns of this composite in fig.53 and Table VI, show several characteristic alumina reflections particularly at a measured d-spacing of 3.45Å (3.479Å Al_2O_3, (012) reflection) which is noticeably absent in typical diffraction patterns of the silicon carbide composite's transfer layer (fig.54).

The aqueous environment in which sliding tests were conducted is also conducive to the degradation of alumina reinforcement. Alumina is known to be susceptible to water accelerated crack growth [124] and undergoes a tribochemical reaction leading to the formation of an aluminium hydroxide film. The hydroxide can lead to a reduction in friction and wear due to its lubricating properties, but these effects can be reversed when alumina is worn against rough surfaces; the higher stresses leading to water accelerated crack growth [125]. Characteristic hydroxide reflections could not be resolved in the current transfer layer investigation, with many of the common d-spacings being close to those of alumina. Nevertheless, the

oxidised appearance of worn alumina reinforced composite surfaces and the extremely fine grained transfer layer material observed in transmission micrographs (fig.51), closely resemble those found on polycrystalline alumina surfaces which have undergone wear in moist or aqueous environments [126,127]. The absence of any significant oxide reflections in the diffraction pattern of the silicon carbide composite's transfer layer, is also an indication that the primary source of oxides on the alumina reinforced alloys worn surfaces, are the alumina particulates themselves. The low incidence of silicon carbide reflections in the wear transfer layer of the 20 vol.% SiC reinforced 6061 alloy (fig.54) is a good indication of the greater hardness and toughness of the silicon carbide reinforcement, where minimal fragmentation and reincorporation of particulates into the transfer layer 'slurry', are conducive to low counterface and composite wear rates.

Notably absent from both the silicon carbide and alumina composites transfer layer diffraction patterns, are any characteristic iron oxide reflections, which were a major constituent of the transfer layer analyses conducted by Alpas and Zhang [13]. A possible explanation for this is the fact that the current investigation involved sliding tests against a stainless steel (as opposed to alloy steel) counterface, thereby reducing the formation and generation of iron oxide and hydroxide products. The transfer layer characterisation by Wang and Rack [14] also found an absence of iron oxide products in their sliding tests of aluminium matrix composites against stainless steel counterfaces.

The shear stresses developed in the immediate wear zone beneath composite surfaces in sliding contact with their respective counterfaces, results in the formation of shear strains which are then accommodated either elastically or plastically. The magnitude of strain accommodation depends on each composite's ability to plastically deform. Factors which influence this ability are the strength of the matrix alloy as well as the degree to which it has been constrained by the interfaces of the reinforcing particulates. The compaction of steel, aluminium and particulate fragments into the interparticulate matrix regions of each composite, would also generate added straining effects in the near surface composite microstructure. By referring to these considerations, the low wear resistance regime of the 2014 alloy reinforced with 20 vol.% alumina can be explained. This composite displays a strain

to failure of 0.9% and is weaker than the unreinforced matrix alloy. Moreover, very little strain energy is required to initiate fracture in this material as it also has the lowest work to fracture value ($E_{fracture}$ = 2.5MJm^{-3}) of all the reinforced alloys. The extent to which the composite accumulates strain in a plastic manner is shown in the subsurface section in fig.46a. Deformation is concentrated primarily in the immediate wear zone, accompanied by particulate fracture to depths of up to 40μm below the worn surface. The composite has a very steep strain gradient with the particulate interfaces constraining the matrix from undergoing shear. This is in contrast to the greater amount of subsurface plastic strain observed in the scanning electron micrographs of the 15 vol.% Al_2O_3 6061 (fig.45) and 10 vol.% Al_2O_3 2014 (fig.46) composites. These composites show evidence of plastic strain accommodation to greater depths below their worn surfaces as a result of their lower reinforcement contents and accompanying reductions in matrix protection.

The subsurface microhardness profile comparison made between the worn monolithic 2014 alloy and the 20 vol.% and 10 vol.% alumina reinforced 2014 alloys in fig.47, is additional evidence of how particulate additions reduce plastic strain accommodation in subsurface wear regions. This effect is apparent in the sharp drop in matrix microhardness as a function of depth below the worn surfaces of the 10 vol.% and 20 vol.% alumina reinforced alloys, while the monolithic 2014 alloy has a gentler subsurface work-hardening gradient. What is perhaps even more interesting about these results is the fact that the monolithic 2014 alloy undergoes a greater degree of work-hardening at its worn surface, compared to that found in each of the two composites. This observation is verified by the lower matrix alloy microhardnesses obtained close to the wear surfaces of the two composites, with the 20 vol.% alumina reinforced alloy having the lowest degree of work-hardening. These observations suggest that the matrix alloy in each composite undergoes a relatively lower amount of work-hardening and strain accommodation in order to initiate fracture and wear at the sliding surface, compared to that required in the unreinforced alloy. The higher yield stresses arising in the matrix alloy, as a consequence of increased matrix protection and constraint effects by the reinforcing particulates, introduce a 'pseudo-brittle' effect in the matrix. Thus failure of the constrained matrix alloy in the composites, occurs at lower levels of plastic strain and work-hardening than those found in the monolithic alloy. In addition, the

abrasive nature of the reinforcing particulates and the wear transfer layer, would also contribute to the rapid removal of any heavily sheared or 'unprotected' matrix at sliding interfaces. The schematic diagram in fig.76 illustrates the aforementioned plastic strain accommodation effects, arising in both reinforced and unreinforced alloys during steady state sliding wear.

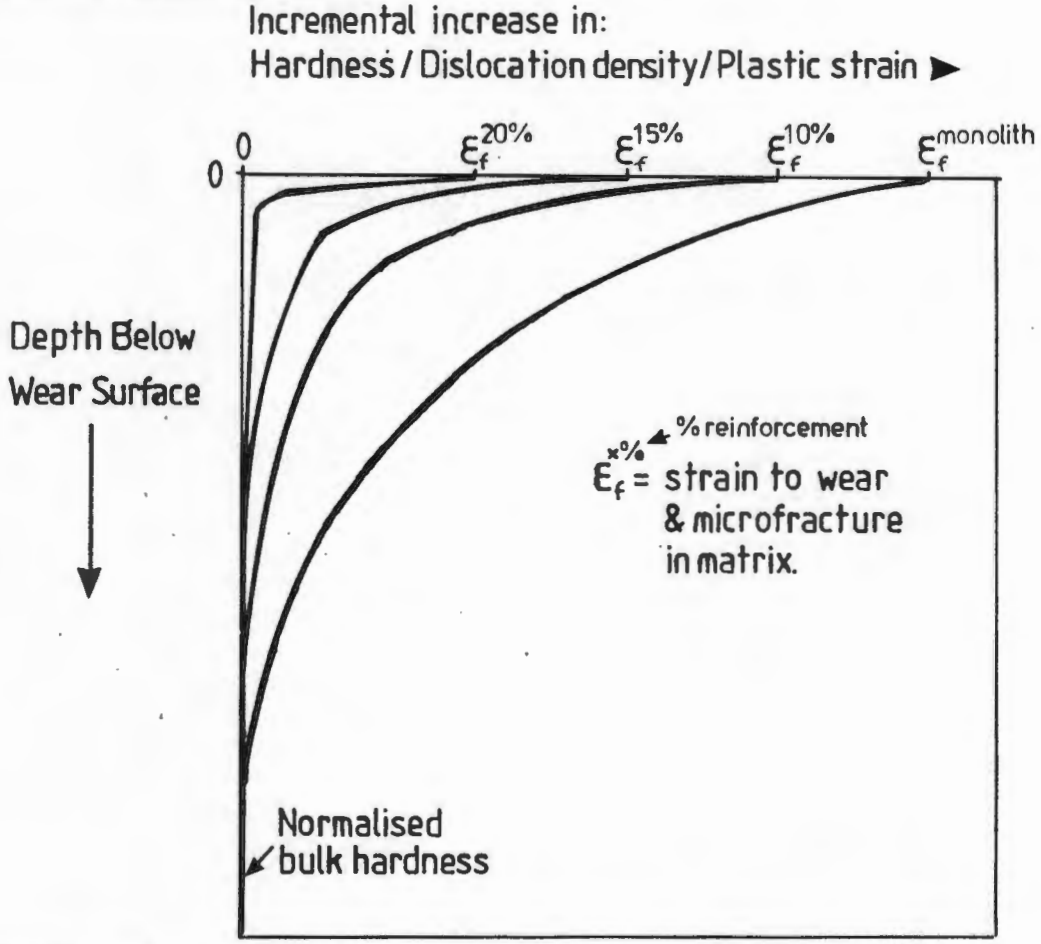

Fig.76: Schematic illustrating the effect of particulate additions on plastic strain accommodation in an aluminium alloy, below the sliding wear surface.

The low strength and inability of the 20 vol.% alumina reinforced 2014 composite to accommodate strain results in particulate failure in the subsurface region. The triaxial stresses generated in this region are sufficient to initiate premature fracture of the particulates, resulting in a lowering of matrix constraint and degradation in stiffness, accompanied by increased wear losses. Material removal during the high-wear regime probably occurs as a result of crack propagation and tearing of matrix

between fractured particulates, resulting in delamination and exposure of unworn composite to the counterface. Steady-state wear ensues as a continuous process of composite and counterface surface degradation by delamination and abrasion, with there being little chance of a stable transfer layer forming. This is confirmed by comparing the worn surfaces of the 15 vol.% (fig.39) and 20 vol.% (fig.40) alumina reinforced 2014 alloys, where the 15 vol.% alloy is smoother in appearance than the 20 vol. % material in its high-wear regime; the 15 vol.% composite having developed a stable wear transfer layer. In addition, the greater loss of material from the 20 vol.% composite can be correlated with the significant adhesion of transfer layer material on the surface of the counterface, against which it is worn (fig.34). These observations agree with those reported by Alpas and Embury [58], who obtained a similar high wear rate for an 2014 alloy reinforced with 20% silicon carbide. This composite also displayed a very low strain to failure and a wear mode involving extensive delamination and cracking of the surface transfer layer, resulting in exposure of reinforcing particulates and significant damage to the counterface.

Subsurface cracking and delamination of the wear transfer layer *per se*, was also observed in the subsurface worn microstructure of the worn 20 vol.% alumina reinforced 2104 alloy, in its high-wear regime (fig.46). The instability of the transfer layer is probably enhanced by being restricted to a very narrow surface region where shear forces are very high and the plastic accommodation of transfer layer material induced strains into the matrix are prevented by the large degree of matrix constraint.

The 20 vol.% alumina reinforced 2014 alloy also exhibited an initial low wear regime (fig.30) which could be termed an "incubation period", whereby strain is accumulated in the subsurface regions prior to particulate fracture and rapid material loss. However, the erratic behaviour of this composite during sliding tests, where in some instances the "low-wear regime" extended in excess of 10^6 cycles, make such assertions difficult to justify. Further work involving TEM examination of subsurface structures in the two wear regimes, would need to be conducted so as to gain further understanding of the strain accumulation mechanisms in operation.

5.3.1 *Dislocation substructures*

The dislocation substructures observed in the worn 6061 monolithic alloy and its 10 vol.% and 20 vol.% alumina reinforced counterparts, arise as a result of the cyclic stresses generated by the reciprocating motion of the surfaces in contact with each other. Constraints imposed on the matrix aluminium alloy by reinforcing particulate interfaces, together with the overall increase in stiffness of the system, allow for an increase in the elastic accumulation of the energy transmitted at the sliding interface. There is a reduction in plastic strain for surface failure and increase in strain gradient in the subsurface wear zone as the reinforcement content of the composites is increased (see the schematic diagram in fig.76). In reciprocating sliding situations, these effects result in a lowering of the plastic strain amplitude (γ_{pl}) in the interparticulate matrix region at equivalent depths beneath their worn surfaces. The resulting persistent slip band (PSB) "ladder" structures obtained in the 10 vol.% and 20 vol.% alumina reinforced 6061 alloys are typical features found in face centred cubic metals deformed under low amplitude cyclic loading conditions [108,109]. The cell-like features obtained in the monolithic alloy, at approximately the same subsurface depth as those of the 10 vol.% reinforced alloy, are indicative of high γ_{pl} fatigue structures; most of the strain energy being accumulated plastically within a greater subsurface volume, due to the alloy having a lower overall stiffness and being less constrained by reinforcement interfaces. The large dislocation densities associated with the monolithic alloy subsurface cell structures is yet additional evidence that the strains for wear and microfailure in the unreinforced alloys are considerably larger than those obtained in the reinforced alloys.

Despite the existence of characteristic fatigue type strain accumulation microstructures in the subsurface regions of the 6061 matrix alloy and composites, further work is still necessary in order to ascertain whether strain localisation and subsurface crack nucleation and debris formation arise from either persistent slip bands or other shear type structures. The presence of secondary dislocations together with PSB's in the worn subsurface region of the 20 vol.% alumina reinforced 6061 alloy (fig.50) as well as the existence of heavily sheared cell microstructures in the near surface region of this composite (fig.52), are indications

that the stresses arising in these heavily strained regions are more complex than simple cyclic strain accumulation at constant γ_{pl}. Moreover the greater strain gradients and localisation of deformation in the near surface regions of the reinforced and unreinforced 2014 matrix alloys would make these materials more prone to extraneous shear type plastic strains. Hirth and Rigney [128] postulated that the loading spectra obtained at asperity contacts during sliding contact, closely resemble those obtained in cyclic stressing and fatigue loading experiments. However, the loading differs from uniaxial type deformation, in that it produces multiaxial stressing with compression weighted more than tension. In addition, the multiple asperity interactions produce a spectrum type loading situation where γ_{pl} is not constant. Typical subsurface dislocation structures found in unidirectional sliding wear experiments resemble the cell features observed in fig.48, showing large misorientations between the individual cells. At greater depths below the worn surfaces and lower strains, the substructures generally consist of equiaxed subgrains with less misorientation between them [114,128,129,130]. Similar substructures have also been observed in low carbon steel under reciprocating motion [131]. Additional work is thus necessary to further characterise the dislocation substructures in both the 6061 and 2014 alloys and their composites. Of particular interest would be an investigation of the transition from constant γ_{pl} fatigue structures, to misoriented cell and shear band features in the near surface regions, and how these are affected by reinforcement constraints.

A common feature of sliding wear situations is the generation of thermal energy at asperity contacts on the sliding surface; commonly referred to as flash heating. The magnitude of temperatures generated depend on a variety of factors, the most important being the sliding speed, load and thermal conductivity of the materials in contact [113]. Large flash temperatures are generated at asperity contacts where there is an increased resistance to heat flow. Oxide materials in particular, are prime candidates for reducing heat flow and generating high flash temperatures when present at sliding asperities. The presence of alumina reinforcing particulates in each of the aluminium alloys would therefore be conducive to the generation of large asperity temperatures at sliding interfaces. While the use of water as a debris remover and coolant during sliding tests may have limited heating effects, there is evidence for some recovery having occurred in the matrix alloy, close to the worn

surface of the alumina reinforced composite shown in fig.52. The fine crystallite structure displayed in fig.52 is indicative of continuous plastic deformation and recovery having occurred without any significant recrystallisation effects ie. large grain sizes. The low thermal conductivity of alumina (27 $Wm^{-1}K^{-1}$ - Table VII) compared to that of aluminium (239 $Wm^{-1}K^{-1}$) reduces the rate of heat flow away from the deforming matrix, encouraging recovery effects and adiabatic shear phenomena at the wear surface. The removal of any cooling liquid or lubricant from a sliding couple of alumina reinforced aluminium and steel, would most probably result in the rapid generation of large flash temperatures and increased wear losses arising from thermal softening and adiabatic shear at the sliding interface.

Silicon carbide on the other hand, has a much higher thermal conductivity when compared to that of alumina (Table VII). Thermal conductivity values range between 63 $Wm^{-1}K^{-1}$ and 270 $Wm^{-1}K^{-1}$ depending on the level of purity and internal crystal defects. Pure single crystal silicon carbide has a very high thermal conductivity of around 270 $Wm^{-1}K^{-1}$ which exceeds that of aluminium (239 $Wm^{-1}K^{-1}$) [134]. The small size of the silicon carbide particulates used as reinforcement in the 6061 alloy, is conducive to low levels of porosity and internal defects being present in them and therefore high values of thermal conductivity. Thus, flash temperatures at silicon carbide asperities would be expected to be very low, if not lower than those generated in the aluminium matrix as a result of shear. From these observations it can be inferred that silicon carbide reinforced aluminium alloys are ideal for sliding wear applications where there is a danger of lubricant starvation and overheating.

5.4 Solid Particle Erosion

The two unreinforced matrix alloys display erosive wear modes that are characteristic of those found for ductile metals [77,78]. Steady-state eroded surfaces of each alloy after erosion at 90° to the target surface, show extensive plastic deformation and indentation (see fig.59a). The energy transmitted to each aluminium surface during normal impact by the silicon carbide erodent is

accommodated primarily through strain hardening and lateral displacement of the surface metal. In contrast, during erosion at a lower impact angle of 30° (fig.59b), the energy transferred to the metal surface by each erodent particle, is largely consumed through continuous removal of the aluminium metal by shear and micromachining. This results in a markedly higher material removal rate accompanied by less subsurface deformation.

The onset of steady state erosion in each matrix alloy is preceded by an initial incubation period of mass gain, where erodent particles become embedded in the softer aluminium matrix. The incubation period is most probably a consequence of both erodent particles embedding in the target surface and the build-up of plastic strain. This effect is most marked at 90° erosion where a large proportion of impact energy is converted into plastic deformation and shear of the aluminium. The harder 2014 alloy shows a smaller incubation region at 90° impact accompanied by a slightly greater erosion rate, when compared to the softer 6061 alloy. The micrographs in figs.61 depicting subsurface steady state deformation in the two monolithic alloys, show greater depths of erosion damage in the softer 6061 alloy at 90° impact. Both alloys exhibit entrainment of erodent fragments in their subsurface regions although this is noticeably less in the 2014 alloy where particles are less likely to embed into the harder surface. Silicon carbide erodent fragments, which have embedded into the 6061 alloy and increased its hardness, will also be responsible for added erosion resistance over that of the 2014 alloy. When impact energies are largely consumed by shearing and micromachining of each alloy's surface at a 30° erosion angle, the softer and less shear resistant 6061 aluminium displays a greater wear rate than the 2014 alloy; erodent particles being able to displace and remove greater volumes of the softer 6061 alloy. Thus the level to which particulates become embedded in the surface of a target material, has a direct influence on the steady state erosion rates. This effect is most pronounced at 90° impact and is more likely to influence erosion rates during erosion of softer and more accommodating target materials.

Solid particle erosion of the reinforced aluminium alloys is characterised by a general increase in erosion rate over that of their respective matrix alloys. Similar findings have been reported by Goretta et al [84,87] and Hutchings and Wang [85].

The eroded surfaces of each composite show similar features (figs.56c and 59d) to those found in each of the matrix alloys at the two impact angles. However, there is also evidence of extensive reinforcing particulate fracture and the deformed metal is less ductile in appearance indicating constrained plastic flow and intense shear; this is particularly evident in alloys with higher reinforcement contents. The subsurface damage in the eroded 20 vol.% SiC reinforced 6061 alloy (figs.62a and 62b) reveal a larger amount of reinforcing particulate fracture and plastic deformation, although the subsurface depth to which these features are found is considerably less compared to that observed at 90° and 30° erosion in the 6061 monolithic alloy (fig.61a and 61b). Plastic strain accommodation extends to some 100μm in the 90° eroded taper section of the composite in fig.62a, whereas the monolithic 6061 alloy displays plastic deformation to depths of around 300μm (fig.62a). By comparison, the taper sections of the 30° eroded surfaces show plastic strain accommodation to around 100μm in the monolithic 6061 and approximately 20-30μm in the composite (fig.62b). The erosion rates of the 6061 monolithic alloy are found to be almost half of those obtained for the SiC reinforced 6061 composite at 90° impact, yet the depth of subsurface deformation in the monolithic alloy is approximately three times that obtained in the composite. Thus strains for wear and microfracture in the reinforced alloys are well below those required for material removal in the monolithic alloys.

Further evidence for microfracture and wear loss occurring at lower levels of plastic strain in the composite materials, is found in figs.55 and 56. When the incubation periods of the monolithic alloys are compared with those of the composites, each alloy displays a smaller incubation period and increase in steady state wear (steeper slope of cumulative mass loss curve) as reinforcement contents are increased. The incubation period is indicative of the amount of plastic strain that a material can absorb prior to wear loss and microfracture; this being smallest in composites with the highest reinforcement contents. Particulate embedding also directly influences the magnitude of incubation periods and erosion rates, but these effects would most likely be negligible in the composites having greater hardnesses.

The scanning electron micrographs depicting single impact sites in the 6061 monolithic alloy (figs.60a and 60b) and 20 vol.% alumina reinforced 2014 alloy

(figs.60c and 60d) provide additional evidence for the claim that composite wear losses occur at low plastic strains. Micrographs showing impact at 90° and 30° in the monolithic 6061 (figs.60a and 60b) exhibit extensive ductility of the deformed metal in each impact site with little evidence of any microfracture. Thus additional strain accommodation by particle impact would be needed to effect further strain hardening, microfracture and removal of the plastically deformed alloy in each impact site. The impact sites on the surface of the alumina reinforced 2014 alloy (figs.60c and 60d) display markedly less ductility and considerable damage to both reinforcing particulates by microfracture, and the matrix alloy by intense shear deformation and constrained flow. There is also little difference in ductility between the impact sites at 90° and 30° on the composite surface.

Both constrained plastic flow and intense shear of matrix alloy are common features associated with the tensile deformation of reinforced alloys. These deformation phenomena also exist on the eroded surfaces of the composites (figs.59c and 59d) and single impact sites (figs.60c and 60d) where there is evidence of intense shear, microextrusion and constrained plastic flow of matrix alloy. During solid particle impact, the depth of plastic deformation and indentation initiated by impacting particles on composite surfaces, is controlled by the degree to which reinforcing inclusions constrain the plastic flow of interparticulate matrix alloy. As matrix constraint is increased by higher volume fractions of reinforcing particulates, there is an associated increase in yield strength and lowering of ductility of the matrix, with an accompanying transfer of load to the high modulus inclusions. The plastic strains required to initiate matrix failure during erosion are therefore reduced as a consequence of the increased yield and 'embrittlement' of the interparticulate matrix alloy.

The fracture of reinforcing particulates was a common feature associated with solid particle erosion of all the composites. Fracture and fragmentation is initiated by the hard erodent particles indenting the reinforcing inclusion surfaces as well as by the transfer of strain from the plastically deforming matrix alloy. It therefore seems highly probable that the toughness of reinforcing particulates and their elastic compatibility with the plastically deforming matrix, are important determinants of the rate of fracture and wear loss occurring during the erosion of composites. In this

regard, silicon carbide particulates are better able to resist fracture compared to alumina reinforcement, due to their enhanced fracture toughness and ability to withstand greater degrees of stress transfer in an environment of plastically deforming matrix. The greater erosion resistance of the 20 vol.% SiC reinforced 6061 alloy as compared to that of the same alloy reinforced with 20 vol.% alumina (fig.57), can therefore be explained in terms of the enhanced elastic compatibility and fracture toughness of the silicon carbide reinforcing inclusions.

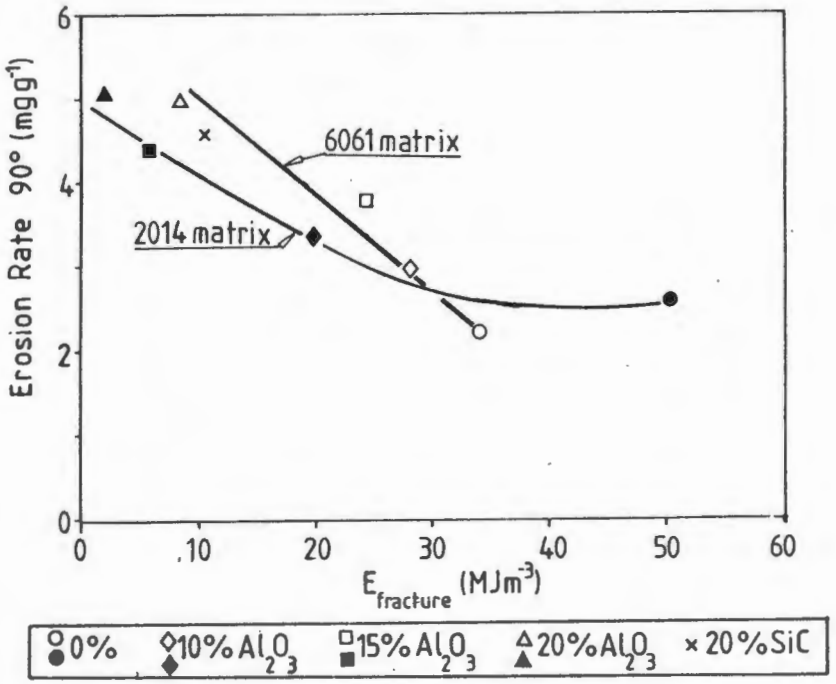

Fig.77: Solid particle erosion resistance of each of the composites and their respective matrix alloys, plotted as a function of their tensile work to fracture values ($E_{fracture}$), for erosive impact at 90° incidence.

Erosion rates of each composite are influenced by their respective ductilities, with the least ductile materials exhibiting the greatest mass losses and smallest incubation periods. While ductility remains an important consideration in analysing erosion behaviour, other researchers have invoked energy parameters based on the mechanical work required to initiate failure in various materials [86,132]. These energy terms are based on the product of the material's tensile stress and strain to failure, which gives a parameter equivalent to the plastic work per unit volume. A particle striking the surface of a material transmits a certain amount of kinetic

energy into its microstructure. If the impact energy exceeds that required to initiate failure in the material, then subsurface rupture will occur. Alloys or composites which have low fracture energies will then become more susceptible to erosive wear loss. In this investigation, the work to fracture parameters ($E_{fracture}$) of each alloy and composite have been plotted against their respective erosive wear rates at a 90° erosion impact angle in fig.77; $E_{fracture}$ values were measured from the area beneath each material's stress-strain curve obtained from the tensile tests (figs.12 and 13).

The reinforced 6061 and 2014 alloys show reasonable correlation between their erosion rates and $E_{fracture}$ values, where a general trend of decreasing erosion resistance with lower $E_{fracture}$ energy is evident.

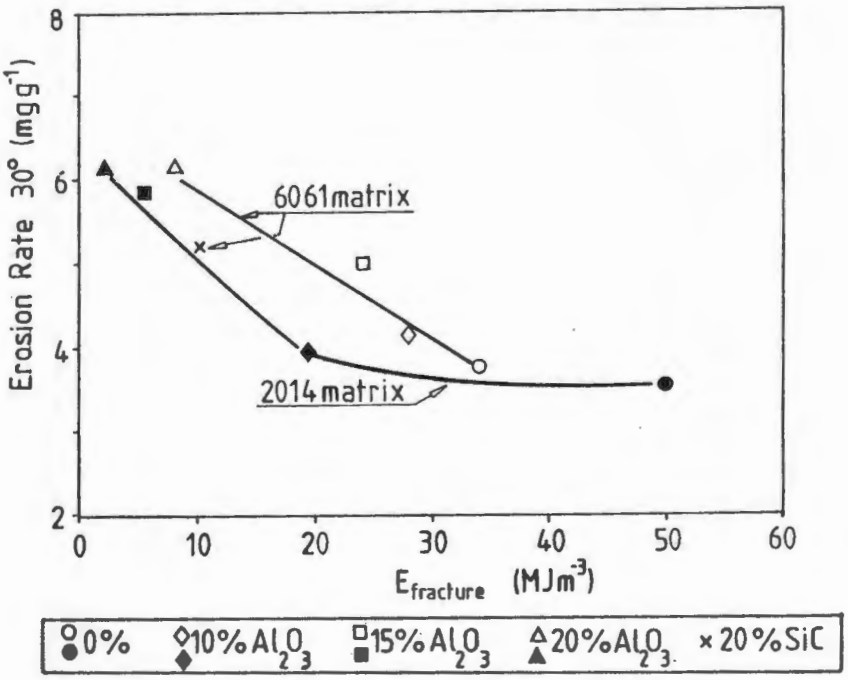

Fig.78: Solid particle erosion resistance of each of the composites and their respective matrix alloys, plotted as a function of their tensile work to fracture values ($E_{fracture}$), for erosive impact at 30° incidence.

The stronger unreinforced 2014 alloy has a higher erosion rate compared to its 6061 counterpart despite having a greater $E_{fracture}$ value. This can be accounted for when the effect of erodent particle embedding in the softer 6061 matrix is taken into account; thereby increasing its erosion resistance. This is illustrated by the much

longer incubation effects shown by the softer 6061 alloy (figs.55 and 56). When the erosion rates of each material are plotted against their $E_{fracture}$ values, for erosion at 30° impacting conditions (fig.78), the 6061 monolithic alloy is less resistant compared to the 2014 alloy; there being very little embedding of particulates into the softer and less shear resistant matrix alloy at this eroding angle.

Both the 6061 matrix materials and the reinforced 2104 alloys show reasonable correlation with their $E_{fracture}$ values. The monolithic 2014 alloy has a relatively higher erosion rate at both impact angles in spite of its high $E_{fracture}$ value. This deviation can be attributed to the difference in modes of deformation and fracture obtained during erosion, as opposed to a tensile test. Energy absorption by deformation and fracture during erosion occurs under stress state conditions which are constrained and multiaxial in nature, similar to those found in a hardness test. In contrast, the energy required for a tensile test, arises from a largely unconstrained, almost uniaxial stress state [133]. Also apparent, are the large differences in strain rate under the two deformation modes and the highly localised nature of shear displacements during erosion, which affect the onset of shear instabilities.

It is interesting to note that the erosion rates of the two alloy systems approach a linear correlation with their respective $E_{fracture}$ parameters, when ceramic particulates are added to their microstructures. A possible explanation for this behaviour may be attributed to the constrained nature of matrix flow in the composite during tensile straining; the mode of deformation being more similar to the multiaxially stressed and constrained flow obtained during erosion of these materials. Under these conditions, the difference in energy absorption between erosive wear and tensile fracture is reduced, as the plastic strains during erosion approach those found at a crack tip when it propagates through a tensile specimen.

Examination of the dislocation substructures obtained during erosion of the reinforced 6061 alloy in fig.57, reveal a subgrain type arrangement which is indicative of large scale strain accumulation in the matrix alloy and possibly adiabatic shear. While these dislocation arrangements are similar to those found in cold worked aluminium [116], further TEM work is necessary to establish the extent

to which shear deformation and accommodation of strain by shear bands is affected by the constraining effects of the reinforcing particulates.

5.5 Cavitation Erosion

The two unreinforced aluminium alloys each display similar cavitation erosion characteristics to those of other age-hardening alloys previously investigated by Vaidya and Preece [93]. They established that aluminium alloys generally show greater erosion resistances when their strengths are increased, either by age hardening or solute content additions. However, the data that they presented relied solely on microhardness as a measure of alloy strength and did not include tensile properties such as yield strength, ultimate tensile strength and ductility. While cavitation erosion data presented in this investigation (fig.66) also shows an increase in erosion resistance for the harder 2014 alloy, it would be necessary to consider properties such as ductility and work to fracture values, before assuming that improved strength and hardness were the only criteria required for improved erosion resistance. Indeed, some alloys may be strengthened considerably by solute additions and ageing treatments, yet experience significant reductions in ductility and work to fracture. In this investigation, the 2104 alloy has both a high strength and ductility, and therefore a high work to fracture compared to the weaker and less ductile 6061 alloy (see Table IV and fig.73).

The erosion data in fig.66 depicts greater erosion losses for the weaker 6061 alloy compared to the 2104 monolithic alloy. Both alloys experience an initial period of incubation prior to the onset of steady state cumulative mass losses (figs.64 and 65) with the incubation for the 2104 alloy being almost twice that of the 6061 alloy. The presence of an incubation period is an indication that erosion losses arise as a result of a process of strain accumulation in the aluminium by work hardening, followed by rupture. The low strength 6061 alloy is less resistant to shear deformation and thus experiences a smaller incubation period, accompanied by increased erosion losses.

With the addition of ceramic reinforcement to each matrix alloy, the incubation periods of the composites show no major deviations from those of their respective matrix alloys. This indicates that the dominant mode of material removal in all the matrix alloys and composites, occurs through strain accumulation and rupture in the matrix alloy of each material. However, the slopes of the cumulative mass loss plots in figs.64 and 65, and erosion data in fig.66, show significant deviations in steady state erosion losses with the addition of reinforcement; the inclusions most probably affecting the rate at which strain accumulation and fracture occurs in the matrix.

Evidence for the reinforcing inclusions having an effect on the plastic deformation of the aluminium matrices, is found in the micrographs exhibiting incubation damage in an unreinforced alloy and composites in figs.67-69. Incubation damage in the 2014 monolithic alloy (figs.67) is similar to that obtained in the 2014 alloy reinforced with 20 vol% alumina (fig.68), in that most deformation occurs through a process of intense ductile shear of the matrix aluminium. However the eroded surface topography in the monolithic alloy is characterised by a uniform ductile appearance, particularly the steady state eroded surface (fig.67c), while that of the composite is distinctly irregular, showing evidence of intense shear and rupture of the matrix at the exposed particulate interfaces. A few of the exposed particulates in fig.68b also show evidence of matrix-inclusion interfacial degradation. Damage initiation in the silicon carbide reinforced 6061 alloy (figs.69) is similar to that obtained in the 2014 composite except that the integrity of the reinforcing particulate is maintained with there being no apparent evidence of interfacial degradation.

The erosion rates of each reinforced alloy bear no correlation with their respective bulk hardness values. This lack of correlation is demonstrated in fig.79 which displays each material's cavitation erosion rate plotted as a function of bulk hardness. Solid particle erosion data have also been included on this plot for comparison, where there is also no correlation with hardness. Both erosion modes are thus associated with strain accumulation and failure phenomena, as opposed to indentation type wear mechanisms where high bulk hardnesses would lead to improved wear resistances.

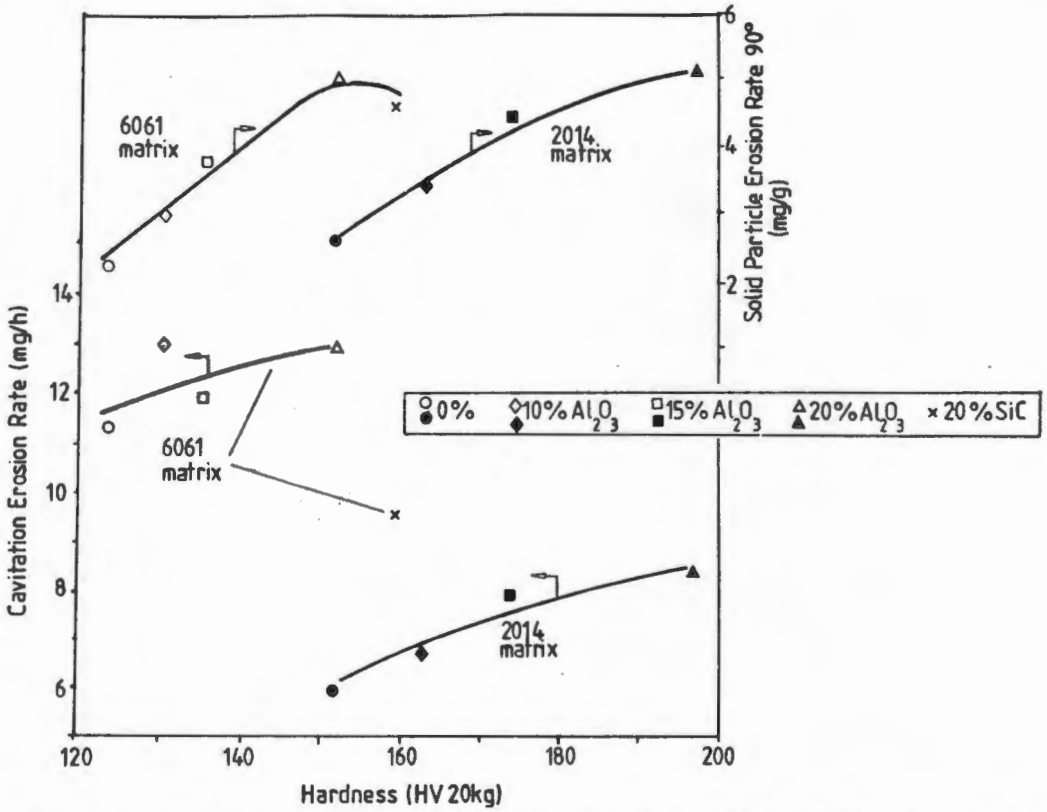

Fig.79: Cavitation and solid particle erosion data of the composites and monoliths, plotted as a function of their respective bulk hardness values. There is no correlation between hardness and erosion resistance; there being a significant lowering of erosion resistance with increased hardness, in both erosion modes.

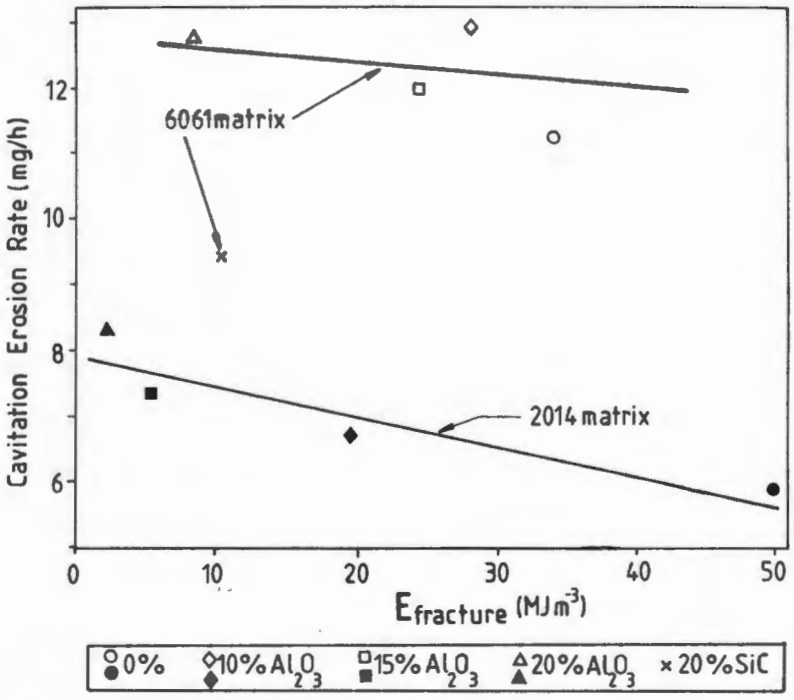

Fig.80: Cavitation erosion rates of each of the reinforced and unreinforced alloys, plotted as a function of their respective tensile work to fracture ($E_{fracture}$) values.

Steady state cavitation erosion rates of each material are plotted as a function of their respective work to fracture ($E_{fracture}$) values in fig.80. The alloy with the greatest work to fracture, namely 2014 aluminium, together with its alumina reinforced composites, each show improved erosion resistances when compared to those of the reinforced and unreinforced 6061 matrix alloys. The addition of alumina reinforcement to each of the matrix alloys results in a general decrease in erosion resistance, whereas the addition of 20 vol.% SiC to the 6061 alloy results in a dramatic increase in erosion resistance. The mode of failure in each material is clearly dominated by strain accommodation and rupture in the matrix aluminium. This being verified by the greater erosion resistances obtained for the reinforced and unreinforced alloys whose matrix has the highest work to fracture, namely the 2014 alloy.

There is no direct correlation between the $E_{fracture}$ values of the composites and their respective erosion rates. If this were the case, then both the 6061 and 2014 matrix composites would show a combined correlation with their respective $E_{fracture}$ values. Such a correlation was obtained for solid particle erosion (figs.77 and 78) where the 20 vol.% alumina reinforced 2014 composite with the lowest $E_{fracture}$ value ($2.2MJm^{-3}$) experienced the highest erosion rate of all the reinforced and unreinforced alloys.

The lack of correlation between composite $E_{fracture}$ values and their erosion rates also suggests that the nature of plastic strain accumulation during cavitation does not occur through large scale deformation and bulk fracture of subsurface material, as is the case during solid particle erosion. Instead, plastic deformation and material loss most probably arises as a result of highly localised intense shear of matrix aluminium. This is confirmed by the subsurface taper sections of the eroded 2014 monolithic alloy (fig.71a), the 20 vol.% SiC reinforced 6061 alloy (fig.72a) and the 20 vol.% Al_2O_3 2014 alloy (fig.72b), where the deformation is restricted to the immediate subsurface regions, there being no evidence of large scale deformation and fracture. Furthermore, the absence of any significant work-hardening below the

surface of the eroded 2014 monolithic alloy (fig.71b) is an indication that the plastic deformation is highly localised at the erosion surface.

Both the optical micrographs in figs.72 depict matrix fracture paths passing close to particulates and exposing them at the eroded surface. The matrix alloy appears to have ruptured away from the particulates leaving a thin coating of aluminium on the exposed particulate surfaces. This effect is more noticeable in the 2014 matrix composite (fig.72b), probably to the fact that its matrix alloy has a high work to fracture and is more resistant to shear deformation, compared to that of the 6061 matrix composite in fig.72a. The existence of intensely sheared matrix alloy at particulate interfaces is consistent with the eroded composite surface morphologies shown in figs.67-69, where intense shear and rupture of matrix alloy appear adjacent to particulate interfaces.

Heathcock et al [92], established that materials with a greater elastic resilience displayed better resistances to cavitation erosion. The addition of high modulus ceramics to aluminium alloys results in an overall increase in their ability to absorb and dissipate impact energy in an elastic manner. Thus, an increase in erosion resistance with greater volume fractions of high modulus alumina reinforcement would be expected. However, the erosion data for each of the alumina reinforced alloys contradicts these considerations, with composites having higher elastic moduli showing greater wear losses. One of the factors which may be controlling the intensity of the shear deformation occurring adjacent to particulates, and therefore erosion rates, is the effect of modulus mismatch between particulate and matrix interfaces. There is a large difference in elastic strain and plastic strain mismatch between aluminium and alumina particulates during cavitation deformation. As a result of this there could be an expected increase in probability of matrix rupture and work-hardening at matrix-particulate interfaces, depending on whether there is efficient transfer of strain energy from the plastically deforming matrix to the higher modulus inclusions.

Both the alumina and silicon carbide particulates constrain the interfacial matrix alloy from deforming, with elastic and plastic strain mismatch arising between regions of constrained interfacial aluminium and relatively unconstrained

interparticulate alloy. This results in intense shear and work hardening effects occurring away from the interface, leaving a thin layer of alloy surrounding the particulates (figs.72). The reasons why increased erosion rates are found in the alumina reinforced alloys, over that of their respective matrix alloys, and the silicon carbide reinforced alloy in the 6061 based materials, are most probably due to the degradation of the interface in these composites. Evidence for some interfacial degradation is observed in fig.68 on a limited scale, but is clearly present in the electropolished eroded surfaces of the 20 vol.% alumina reinforced alloy, shown in figs.70a and 70b. The interface appears to have cracked at the junction between the spinel layer products on particulate surfaces, and the alumina. The cracking most probably arising as a result of the elastic modulus mismatch between the spinel layer and the alumina particulate during high frequency shock loading encountered in cavitation. As a result of the degradation of the interface, there is a reduction in the transfer of strain energy from the plastically deforming matrix to the stiffer alumina inclusions. An overall reduction in plastic constraint and yield stress of the matrix is experienced, rendering it more susceptible to erosion damage. The alumina particulates are also more angular in morphology when compared to the silicon carbide particulates. The increased angularity would result in there being a greater probability of added stress concentrations effects and concentration of deformation at alumina-aluminium interfaces, giving rise to increased matrix and particulate failure and higher erosion rates.

The 20 vol.% silicon carbide reinforced 6061 alloy on the other hand, experiences a significant decrease in erosion rate over its matrix alloy and all the alumina reinforced 6061 alloys. This occurs in spite of the fact that it has a greater elastic modulus than alumina, and therefore a larger elastic and plastic strain mismatch with the surrounding matrix alloy. Evidence from the micrographs in figs.69a-69b suggest that matrix alloy remains bonded to the silicon carbide reinforcement during erosion, indicating that matrix-particulate bonds are probably very high. Thus, due to this enhanced compatibility, the matrix alloy will tend to shear and rupture preferentially in the matrix regions close to the silicon carbide interfaces, or within the particulates themselves if they have internal flaws. In this regard the

electropolished surface of the eroded 20 vol.% SiC 6061 composite in fig.70c does show some minor evidence of internal particulate cracking, which is probably nucleated at internal flaws. Unlike the alumina reinforcement, there is no evidence for interfacial degradation between the 6061 alloy and silicon carbide reinforcement. With no deterioration in the interface occurring, there is a more efficient transfer of strain from the plastically deforming matrix which is immediately adjacent to the particulate surfaces. The resulting increase in plastic constraint and yield strength of the matrix alloy adjacent to the silicon carbide, renders it less susceptible to erosion damage. The strain energy introduced by cavitation erosion shock waves is thus attenuated in an elastic fashion, resulting in reduced erosion losses in the matrix alloy of this composite.

6.0 Conclusions

An attempt has been made to characterise the wear behaviour of two age hardening commercial aluminium alloys, each reinforced with different volume fractions of hard ceramic particles, in a variety of tribological situations. The tensile characteristics of each composite were investigated in order to facilitate interpretation of their various tribological responses. The results of this investigation are summarised as follows:

The strength of each reinforced aluminium alloy is dependent on the degree to which plastic slip processes are inhibited by the constraining effects of the ceramic particulates, the strength of the matrix alloy itself, and the ability of the reinforcing ceramic particulates to resist fracture. Composites having the weaker 6061 alloy as matrix, require additional straining and work hardening in order to generate levels of triaxial stress sufficient to initiate fracture in the ceramic inclusions. In contrast, the stress levels generated in the stronger 2014 matrix alloy were sufficient to initiate fracture in the alumina reinforcing particulates after very little plastic strain accumulation. As a consequence of this the reinforced 2014 alloys displayed a deterioration in strength and strain to failure with increase in reinforcement content.

Abrasive wear rates of each composite range between two and six times lower than those of their respective matrix alloys, with greatest improvements occurring during low contact stress conditions. Each of the reinforced and unreinforced alloy's abrasion resistance is related to their respective macrohardness values. The macrohardness of each composite is dependent on the strength of the matrix alloy, the level to which the matrix alloy is plastically constrained by the reinforcing particulates and the hardness and toughness of the ceramic particulates themselves. The microfracture of reinforcing particulates is found to influence each composite's abrasion resistance; the effect being most noticeable during high stress abrasion and abrasion by a very hard abrasive such as silicon carbide, where the softer and low toughness alumina reinforcements show a poor resistance to indentation fracture. Under these conditions, a degradation in wear resistance of the alumina reinforced alloys to levels close to or below those of their respective matrix alloys is found. A silicon carbide reinforced 6061 alloy has the greatest wear resistance of all the composites. This was attributed to the silicon carbide reinforcement's high hardness, toughness and compatablity to strain transfer from the plastically deforming matrix.

Adhesive transfer and wear loss of aluminium to steel surfaces during reciprocating sliding wear conditions, is found to be reduced by almost three orders of magnitude by the addition of ceramic reinforcement to each of the aluminium alloys. Steel

counterfaces are also found to undergo wear losses due to the abrasive action of the ceramic particles; the silicon carbide reinforced 6061 imparts the least counterface damage and removal. The sliding wear behaviour of each composite is characterised by the formation of a transfer layer on the surface in contact with the steel counterface. The stability of this transfer layer is dependent on the strength and ductility of each composite. By plastically constraining the matrix alloy, ceramic reinforcing particulates prevent shear flow and plastic instabilities arising in the aluminium matrix at the sliding interface. The particulates also become load bearing while in contact with the steel counterface, thereby protecting the matrix alloy from shear forces created by contact. In this regard, the 2014 alloy reinforced with 20 vol.% alumina displays erratic wear losses that were generally greater than any of the other composites. These effects are attributable to its poor strength and low strain to failure. The composite is unable to accommodate shear strains developed at the sliding interface, encouraging subsequent rapid deterioration of the transfer layer and increased abrasion of the counterface.

The solid particle erosion resistances of the composites are below those of their respective matrix alloys. Erosion rates of up to twice those of the matrix alloys are obtained with the addition of 20 vol.% alumina particulates. A reasonable correlation is found between the solid particle erosion resistances of each of the composite materials and their respective work to fracture ($E_{fracture}$) values calculated from tensile test data. The addition of ceramic reinforcement to each alloy results in a deterioration in their erosion resistances, indicating that mass losses were not dependent on resistance to indentation hardness, but rather on each material's ability to accumulate strain followed by shear failure of the matrix. Eroded surfaces display increasing amounts of plastic constraint and microfracture of the matrix alloy, with the addition of higher volume fractions of reinforcement.

The cavitation erosion resistances of each of the alumina reinforced composites are similar but slightly inferior to those of their respective matrix aluminium alloys. The erosion resistance of a silicon carbide reinforced alloy is found to significantly enhance erosion resistance to a level below that of its matrix alloy. Incubation periods show little deviation with the addition of ceramic reinforcement, indicating that the major material removal mode is through strain accumulation and rupture in the matrix alloy. The alumina reinforced alloys display a slight trend in increasing erosion rate with higher volume fractions of particulates and lower work to fracture ($E_{fracture}$) values. The possibility that the alumina reinforcement may be responsible for higher erosion rates by undergoing interfacial degradation when exposed to the cavitating liquid, is proposed. In contrast, the greater erosion resistance of the silicon carbide reinforced alloy is attributable to the greater integrity of its matrix-inclusion interfaces, there being more efficient accomodation of strain transfer from the aluminium undergoing intense

shear at the interfaces.

This investigation has demonstrated that aluminium matrix composites exhibit distinctly different performances relative to those of unreinforced alloys, depending on the type of tribological situation. This has important consequences for components and machinery manufactured from these materials which are, or have the potential to be, subjected to more than one type of wear during normal or adverse operating conditions. These materials have widespread potential for use in tribological conditions involving low indentation and impact stresses. Possible applications could include components which experience low load abrasion, ideally against fine abrasive media that are softer than the reinforcing particulates. Typical items that are often subjected to low stress abrasion, and which could be manufactured from aluminium matrix composites, include pulleys, conveyor belt rollers, handles, transport containers, storage racks and chutes.

Aluminium matrix composites are also ideally suited for components which experience sliding or rubbing contact with other metal surfaces. Their extremely high seizure resistance over that of aluminium alloys makes them ideal for use in the automobile and general transport sectors. Typical examples which have already found application include pistons, connecting rods, cams and gear selector forks. The use of silicon carbide particulates as reinforcement in aluminium alloys, holds distinct advantages in terms of resistance to sliding wear, abrasion and cavitation erosion, making them ideal for use in engine components. Silicon carbide reinforced alloys offer increased rates of transport of thermal energy away from sliding interfaces, reduced thermal expansion and low counterface abrasion characteristics. In this regard, silicon carbide reinforced engine components offer added protection against seizure when abnormal operating conditions arise eg. lubricant starvation. These qualities can have exceptional cost benefits in tightly controlled production environments such as underground mining situations, where tribological failures involving compressor or engine seizure can lead to debilitating down-time costs.

7.0 References

[1]: A.K. Vasudevan, R.D. Doherty (eds.), Aluminium Alloys - Contemporary Research and Applications, Treatise on Materials Science and Technology, vol.31, Academic Press, San Diego, (1989).

[2]: T.Donomoto, K.Funatani, N.Miura, N. Miyake, Proc. Conf. Soc. of Automobile Engineers, (1983), paper no.830252, March 1983.

[3]: M. Hunt, Materials Engineering, Jan., p.37-40, (1989).

[4]: T.A. Hahn in R.K. Everett, R.J.Arsenault (eds.), Metal Matrix Composites - Mechanisms and Properties, Treatise on Materials Science and Technology, Academic Press, San Diego, Ch.11, p329-354, (1991).

[5]: P.K. Rohatgi, S. Ray, Y. Liu, International Materials Reviews, ASM Int., vol.37, No.3, p.129-149, (1992).

[6]: A. Watanabe, Y.Sugai, T.Tsujimura, K. Takao, E. Nishii, T.Khikawa, Proc. Conf. RASELM 1991, Tokyo, Oct. 1991, Japan Inst. Light Metals, p.525-530, (1991).

[7]: A.G. Wang, I.M. Hutchings, Mater. Sci. Tech., 5, 71-76, (1989).

[8]: S.V. Prasad, P.K. Rohatgi, T.H. Kosel, Mater. Sci. Eng., 80, 213-220, (1986).

[9]: M. Zongyi, B. Jing, L. Yuxiong, S. Hongwei, G. Yinxuan, Wear, 148, 287-293, (1991).

[10]: A. Wang, H.J. Rack, Wear, 146, 337-348, (1991).

[11]: Y. Pan, M.E. Fine, H.S. Cheng, in P.K. Rohatgi, C.S. Yust, P.J. Blau (eds.), Proc. Conf. Tribology of Composite Materials, Oak Ridge TN, May 1-3, (1990), ASM Int., 93-101, (1990).

[12]: A.T. Alpas, J.D. Embury, Scripta Metall. Mater., 24, 931-935, (1990).

[13]: A.T. Alpas, R.J. Zhang, Wear, 155, 83-104, (1992).

[14]: A. Wang, H.J. Rack, Mater. Sci. Eng., A147, 211-224, (1991).

[15]: A. Brown, Materials World, J. Inst. Materials, 1, 20-21, (1993).

[16]: D.L. McDanels, Metall. Trans. A., 16A, 1105-1115, (1985).

[17]: R.J. Arsenault, R.M. Fisher, Scripta Metall., 17, 67-71, (1983).

[18]: R.J. Arsenault, Mater. Sci. Eng., 64, 171-181, (1984).

[19]: Y. Flom, R.J. Arsenault, Mater. Sci. Eng., 77, 191-197, (1986).

[20]: R.J. Arsenault, S.B Wu, Mater. Sci. Eng., 96, 77-88, (1987).

[21]: R.J Arsenault, M.Taya, Acta Metall., 35, 651-659, (1987).

[22]: Y. Flom, R.J. Arsenault, Acta Metall., 37, 2413-2423, (1989).

[23]: R.J. Arsenault, N. Shi, C.R. Feng, L. Wang, Mater. Sci. Eng., A131, 55-68, (1991).

[24]: R.J. Arsenault, L. Wang, C.R. Feng, Acta Metall. Mater., 39, 47-57, (1991).

[25]: R.J. Arsenault, Scripta Metall. Mater., 25, 2617-2621, (1991)

[26]: A.G. Evans, J.W. Hutchinson, R.M. McMeeking, Scripta Metall. Mater., 25, 3-8, (1991).

[27]: Y.L. Klipfel, M.Y. He, R.M. McMeeking, A.G. Evans, R. Mehrabian, Acta Metall. Mater., 38, 1063-1074, (1990).

[28]: J.J. Lewandowski, D.S.Liu, C.Liu, Scripta Metall. Mater., 25, 21-26, (1991).

[29]: S.V. Kamat, J.P.Hirth, R.Mehrabian, Acta Metall. Mater., 37, 2395-2402, (1989).

[30]: J. Yang, S.M. Pickard, C.Cady, A.G. Evans, R. Mehrabian, Acta Metall. Mater., 39, 1863-1869, (1991).

[31]: P.J. Withers, W.M. Stobbs, O.B. Pedersen, Acta Metall., 37, 3061-3084, (1989).

[32]: T. Christman, S. Suresh, Acta Metall, 36, 1691-1704, (1988).

[33]: S. Suresh, T.Christman, Y.Sugimura, Scripta Metall., 23, 1599-1602, (1989)

[34]: T. Christman, A. Needleman, S. Suresh, Acta Metall., 37, 3029-3050, (1989).

[35]: J. Llorca, A. Needleman, S. Suresh, Acta Metall. Mater., 39, 2317-2335, (1991).

[36]: D.J. Lloyd, Acta Metall. Mater., 39, 59-71, (1991).

[37]: Y. Brechet, J.D. Embury, S. Tao, L. Luo, Acta Metall. Mater., 39, 1781-1786, (1991).

[38]: D.L. Davidson, Metall. Trans. A, 18A, 2115-2128, (1987).

[39]: D.L. Davidson, Metall. Trans. A, 22A, 113-123, (1991).

[40]: S.M. Pickard, B. Derby, Acta Metall. Mater., 38, 2537-2552, (1990).

[41]: V. Tvergaard, Acta Metall. Mater., 38, 185-194, (1990).

[42]: C.P. You, A.W. Thompson, I.M. Bernstein, Scripta Metall., 21, 181-185, (1987).

[43]: T. Kobayashi, H. Iwanari, H.J. Kim, E.P. Yoon, Proc. Conf. RASELM 1991, Tokyo, Oct. 1991, Japan Inst. Light Metals, 477-482, (1991).

[44]: Z. Wang, R.J. Zhang, Metall. Trans. A, 22A, 1585-1593, (1991).

[45]: P. Mummery, B. Derby, Mater. Sci. Eng., A135, 221-224, (1991).

[46]: G. Meyer-Rodenbeck, T. Hurd, A. Ball, Wear, 154, 305-317, (1992)

[47]: J. Larsen-Basse, Scripta Metall. Mater., 24, 821-826, (1990).

[48]: M.M. Khruschov, Wear, 28, 69-88, (1974).

[49]: K.H. Zum Gahr, G.T. Eldis, Wear, 64, 175-194, (1980).

[50]: K.H. Zum Gahr (ed.), Microstructure and Wear of Materials, Tribology Series 10, Elsevier, Amsterdam, p.329, (1987).

[51]: B.R. Lawn, A.G. Evans, J. Mater. Sci., 12, 2195-2199, (1977).

[52]: E.A. Almond, L.A. Lay, M.G. Gee, Inst. Phys. Conf. Series, No.75, Ch.9, 2nd Int. Conf. Sci. Hard Mater., Rhodes, 23-28 Sept (1984), 919-948, (1984).

[53]: K. Kendall, Proc. Roy. Soc. London A, 361, 245-263, (1978).

[54]: W. Simm, S. Freti, Wear, 129, 105-121, (1989).

[55]: K.H. Zum Gahr, Proc. Int. Conf. on Wear of Materials, Vancouver, Apr. 14-18, 1985, ASME N.Y., p.45-58, (1985).

[56]: A. Banerji, S.V. Prasad, M.K. Surappa, P.K. Rohatgi, Wear, 82, 141-151, (1982).

[57]: M.K. Surappa, S.V. Prasad, P.K. Rohatgi, Wear, 77, 295-302, (1982).

[58]: W. Horn, W. Ziegler, Proc. Conf. Metallurgical Aspects of Wear, Bad Pyrmont, FRG, 24-25 Oct., 1979, Deutche Gesellschaft fur Metallkunde, 223-235, (1979).

[59]: T.S. Eyre, F. Abdul-Mahdi, Proc. Conf. Aluminium Technology, March 1986, London, Inst. Metals, 485-492, (1986).

[60]: K.H. Zum Gahr (ed.), Microstructure and Wear of Materials, Tribology Series 10, Elsevier, Amsterdam, p.352, (1987).

[61]: F.M. Hosking, F.F. Portillo, R. Wunderlin, R. Mehrabian, J. Mater. Sci. 17, 472-498, (1982).

[62]: F. Rana, D.M. Stefanescu, Metall. Trans. A, 20A, 1564-1566, (1989).

[63]: J. Yang, D.D. Chung, Wear, 135, 53-75, (1989).

[64]: K. Anand, Kishore, Wear, 85, 163-169, (1983).

[65]: N.P. Suh, Wear, 25, 111-124, (1973).

[66]: N. Saka, D. Karalekas, Proc. Int. Conf. on Wear of Materials, Vancouver, Apr. 14-18, 1985, ASME N.Y., 784-793, (1985).

[67]: O.P. Modi, B.K.Prasad, A.H. Yegneswaran, M.L. Vaidya, Mater. Sci. Eng., A151, 235-245, (1992).

[68]: A.D. Sarkar, J.D. Clarke, Wear, 61, 157-167, (1980).

[69]: S. Lingard, K.H. Fu, K.H. Cheung, Wear, 96, 75-84, (1984).

[70]: J.A. Schey, P.C. Nautiyal, Wear, 146, 37-51, (1991).

[71]: L.H. Chen, D.A. Rigney, Wear, 105, 47-61, (1985).

[72]: D.A. Rigney, L.H. Chen, M.G.S. Naylor, A.R. Rosenfield, Wear, 100, 195-219, (1984).

[73]: P. Heilmann, J. Don, T.C. Sun, D.A. Rigney, W.A. Glaeser, Wear, 91, 171-190, (1983).

[74]: C.P. You, W.T. Donlon, J.M. Boileau, in P.K. Rohatgi, C.S. Yust, P.J. Blau (eds.), Proc. Conf. Tribology of Composite Materials, Oak Ridge TN, May 1-3, (1990), ASM Int., 157-167, (1990).

[75]: C.A. Caracostas, W.A. Chiou, M.E. Fine, H.S. Cheng, Scripta Metall. Mater., 27, 167-172, (1992).

[76]: S.Wilson, A. Ball, in P.K. Rohatgi, C.S. Yust, P.J. Blau (eds.), Proc. Conf. Tribology of Composite Materials, Oak Ridge TN, May 1-3, (1990), ASM Int., 103-112, (1990).

[77]: A.W.Ruff, S.M.Wiederhorn, Treatise on Materials Science and Technology, 16, 69-126, (1979).

[78]: A.V.Levy, Wear, 108, 1-21, (1986).

[79]: A.G.Evans, T.R.Wilshire, J. Mater. Sci., 12, 97-116, (1977)

[80]: A.G.Evans, M.E.Gulden, M.Rosenblatt, Proc. Roy. Soc. Lond. A, 361, 343-365, (1978).

[81]: R.A.Vaughan, A.Ball, Proc. Int. Conf. Wear of Materials, Orlando, Florida, April 7-11, 1991, ASME, 71-75, (1991).

[82]: S.K.Hovis, J.E.Talia, R.O.Scattergood, Wear, 108, 139-155, (1986).

[83]: A.Ninham, Wear, 121, 307-324, (1988).

[84]: K.C.Goretta, W.Wu, J.L.Routbort, P.K.Rohatgi, in P.K. Rohatgi, C.S. Yust, P.J. Blau (eds.), Proc. Conf. Tribology of Composite Materials, Oak Ridge TN, May 1-3, (1990), ASM Int., 147-155, (1990).

[85]: I.M.Hutchings, A.Wang, Proc. Conf. New Materials and Their Applications, Inst. Phys. Conf. Series, Warwick, April 1990, 111-120 (1991).

[86]: S.Srinivasan, R.O.Scattergood, R.Warren, Metall. Trans. A, 19A, 1785-1793, (1988).

[87]: W.Wu, K.C.Goretta, J.L.Routbourt, Mater. Sci. Eng., A151, 85-95, (1992).

[88]: Lord Rayleigh, Phil. Mag., 34, 94-98, (1917).

[89]: B.Vyas, C.M.Preece, J. Appl. Phys., 47, 5133-5138, (1976).

[90]: T.B.Benjamin, A.T.Ellis, Philos. Trans. Roy. Soc. Lond. A., 260, 221, (1966).

[91]: Y.L.Chen, T.Kuhl, J. Israelachvili, Wear, 153, 31-51, (1992).

[92]: C.J.Heathcock, B.E.Protheroe, A.Ball, Proc. 5th Int. Conf. on Erosion by Solid and Liquid Impact, Cambridge, England, (1979), 219-224, (1979).

[93]: S.Vaidya, C.M. Preece, Metall. Trans. A., 9A, 299-307, (1978).

[94]: F.B.Pickering (ed.), The Basis of Quantitative Metallography, Inst. Metall. Tech., London, (1976).

[95]: R.Holland, J. Acoust. Soc. Amer., 40, 1051-1057, (1966).

[96]: J.F.W.Bell, J.C.K.Sharp, Rèv. Int. Htes Temp. et Réfract., 12,40-43, (1975).

[97]: ASTM B557M-84, Annual book of ASTM standards (1987), ASTM, p.80 (1987)

[98]: C.Allen, A.Ball, B.E.Protheroe, Wear, 74. 287-299, (1981-82).

[99]: U.F.B.Kienle, MSc. Thesis, University of Cape Town, (1988).

[100]: R.C.Pennefather, MSc. Thesis, University of Cape Town, (1986).

[101]: A.W.Ruff, L.K. Ives, Wear, 35, 195-199, (1975).

[102]: C.J.Heathcock, PhD Thesis, University of Cape Town, (1980).

[103]: J.M.Papazian, P.N.Adler, Metall. Trans. A, 21A, 401-410, (1990).

[104]: G.J.Mahon, J.M.Howe, A.K.Vasudevan, Acta Metall. Mater., 38, 1503-1512, (1990).

[105]: C.P.You, M.Dollar, A.W.Thompson, I.M.Bernstein, Metall. Trans. A, 22A, 2445-2450, (1991).

[106]: M.Taya, K.E. Lulay, K.Wakashima, D.J.Lloyd, Mater. Sci. Eng., A124, 103-111, (1990).

[107]: S.J.Basinski, Z.S.Basinski, A.Howie, Phil. Mag., 19, 899-924, (1969).

[108]: F.Ackermann, L.P.Kubin, J.Lepinoux, H.Mughrabi, Acta Metall., 32, 715-725, (1984).

[109]: J.G.Antonopoulos, A.T.Winter, Phil. Mag., 33, 87-95, (1976).

[110]: J.M.Finney, C.Laird, Phil. Mag., 31, 339-366, (1971).

[111]: D.Kuhlman-Wilsdorf, C.Laird, Mater. Sci. Eng., 27, 137-156, (1977).

[112]: Z.S.Basinski, S.J.Basinski, Prog. in Mater. Sci., 36, 89-148, (1992).

[113]: S.C. Lim, M.F. Ashby, J.H. Brunton, Acta metall., 37, 767-772, (1989).

[114]: D.A.Rigney, M.G.S.Naylor, R.Divakar, L.K.Ives, Mater. Sci. Eng., 81, 409-425, (1986).

[115]: H.Chandra, J.D.Embury, U.F.Kocks, Scripta Metall., 16, 493-497, (1982).

[116]: C.Y.J.Barlow, B.Bay, N.Hansen, Phil. Mag., 51, 253-275, (1985).

[117]: P.F.Thomason (ed.), Ductile Fracture of Metals, Pergamon Press, Oxford, (1990).

[118]: M.Srinivasan in J.B.Wachtman Jr. (ed.), Structural Ceramics, Treatise on Materials Science and Technology, 29, Academic Press, San Diego, 1989, Ch.3, 99-148, (1989).

[119]: S.G.Caldwell, J.J.Wert, J. of Tribology, (ASME Trans.), 107, 379-388, (1985).

[120]: A.R.Rosenfield, Scripta Metall. et Mater., 24, 811-814, (1990).

[121]: H.Liu, M.E.Fine, H.S.Cheng, in P.K. Rohatgi, C.S. Yust, P.J. Blau (eds.), Proc. Conf. Tribology of Composite Materials, Oak Ridge TN, May 1-3, (1990), ASM Int., 329-336, (1990).

[122]: K.Fikuda, Y.Sato, T.Sato, M.Veki, in P.K. Rohatgi, C.S. Yust, P.J. Blau (eds.), Proc. Conf. Tribology of Composite Materials, Oak Ridge TN, May 1-3, (1990), ASM Int., 323-328, (1990).

[123]: D.H.Buckley (ed.), Surface Effects in Adhesion, Friction, Wear and Lubrication, Tribology Series 5, Elsevier, Amsterdam, (1981).

[124]: R.S.Gates, S.M.Liu, E.E.Klaus, Tribology Trans., 32, 357-363, (1989).

[125]: J.K.Lancaster, Tribology International, 23, 371-389, (1990).

[126]: M.G.Gee, Wear, 153, 201-227, (1992).

[127]: A.J.Perez-Unzueta, J.H.Beynon, M.G.Gee, Wear, 146, 179-196 (1991).

[128]: J.P.Hirth, D.A.Rigney, in F.R.N.Nabarro (ed.), Dislocations in Solids, North-Holland, (1983), Vol.6, Ch.25, 1-54, (1983).

[129]: P.Heilmann, W.A.T.Clarke, D.A.Rigney, Acta Metall., 31, 1293-1305, (1983).

[130]: K.Kato, T.Kayaba, Y.Ono, Proc. Int. Conf. Wear of Materials, New York, (1985), ASME, 463-470, (1985).

[131]: I.I.Garbar, J.V.Skorinin, Wear, 51, 327-336, (1978).

[132]: D.G.Rickerby, Wear, 84, 393-395, (1983).

[133]: D.R.K.Rao, B.Venkataraman, M.K.Asundi, G.Sundararajan, Scripta Metall. et Mater., 27, 937-942, (1992).

[134]: M. Ura in S. Saito (ed.), Fine Ceramics, Elsevier NY & Ohmsha Ltd. Tokyo, (1988), Ch.4, 243-251, (1988).

[135]: Mechanical and physical property data, Wrought Composites, Duralcan Composites - San Diego CA, USA, (Alcan Aluminium Ltd.), February 26, 1990.

Appendix 1

A.1: *Modulus of elasticity measurements for aluminium matrix composites:*

Table A1 lists the 1,2 and 1R distortion mode frequencies that were measured from the in-plane resonance spectra for 14mm diameter disks of each composite and monolithic alloy. Poisson's ratio was then obtained from the comparison of the 2D and 1R resonance frequencies [96]. Table A2 lists the calculated Poisson's ratio values, Young's Moduli and K1,2 eigen parameters for each material. Young's modulus values were calculated using the following relationship:

$$E = \rho C_l^2$$

using: $C_l = C_p (1-\sigma^2)^{0.5}$

$$C_p = (2 \pi F_{1,2} r)/ K_{1,2}$$

Where:

E = Young's Modulus
ρ = material density
C_l = angular frequency
C_p = plate frequency
σ = Poisson's Ratio
r = disk sample radius
$F_{1,2}$ = 1,2 distortion mode frequency
$K_{1,2}$ = normalised dilational eigen values, which have been tabulated in ref. [95].

Alloy	Vol.%	$F_{1,2}$ (kHz)	$F_{1,R}$ (kHz)	ρ g/cm^3
6061	0	167.1	251.1	2.68
"	10% Al_2O_3	174.9	264.4	2.76
"	15% Al_2O_3	179.4	267.8	2.84
"	20% Al_2O_3	185.3	276.6	2.89
"	20% SiC	195.6	291.6	2.77
2014	0	168.3	254.9	2.82
"	10% Al_2O_3	175.5	264.8	2.85
"	15% Al_2O_3	184.1	277.6	2.96
"	20% Al_2O_3	186.0	280.4	2.97

Table A1: Measured 1,2 and 1,R resonance frequencies and specific densities, of each reinforced and unreinforced alloy.

Alloy	Vol.%	σ	$K_{1,2}$	E GPa
6061	0	0.326	1.362	69.6
"	10% Al_2O_3	0.319	1.368	78.5
"	15% Al_2O_3	0.314	1.373	85.1
"	20% Al_2O_3	0.309	1.378	91.1
"	20% SiC	0.308	1.379	95.7
2014	0	0.323	1.365	74.7
"	10% Al_2O_3	0.322	1.365	80.4
"	15% Al_2O_3	0.326	1.362	93.6
"	20% Al_2O_3	0.324	1.364	96.9

Table A2: Calculated Poisson's ratio, K1,2 eigen parameters and Young's Moduli for the reinforced and unreinforced alloys.